ADVANCED MATERIALS
www.advmat.de

Laser Irradiation of Metal Oxide Films and Nanostructures: Applications and Advances

Haribabu Palneedi, Jung Hwan Park, Deepam Maurya, Mahesh Peddigari, Geon-Tae Hwang, Venkateswarlu Annapureddy, Jong-Woo Kim, Jong-Jin Choi, Byung-Dong Hahn, Shashank Priya, Keon Jae Lee,* and Jungho Ryu**

Recent technological advances in developing a diverse range of lasers have opened new avenues in material processing. Laser processing of materials involves their exposure to rapid and localized energy, which creates conditions of electronic and thermodynamic nonequilibrium. The laser-induced heat can be localized in space and time, enabling excellent control over the manipulation of materials. Metal oxides are of significant interest for applications ranging from microelectronics to medicine. Numerous studies have investigated the synthesis, manipulation, and patterning of metal oxide films and nanostructures. Besides providing a brief overview on the principles governing the laser–material interactions, here, the ongoing efforts in laser irradiation of metal oxide films and nanostructures for a variety of applications are reviewed. Latest advances in laser-assisted processing of metal oxides are summarized.

1. Introduction

Metal oxides (MOs) are known to exhibit a variety of unique physical and chemical properties that are of significant interest for scientific and technological developments. MOs consisting of at least one metal cation and an oxygen anion can be synthesized with different crystal structures, offering electronic properties ranging from insulator to semiconductor to conductor.[1,2] MOs can be tailored to exhibit desired physical and chemical characteristics under a given operating condition (e.g., temperature, frequency, and pressure) by doping, biasing, or by modifying the stoichiometry. Both simple (single cation) and complex (multiple cations) MOs have been utilized in diverse range of applications, including dielectric capacitors, ferroelectric memories, piezoelectric sensors and actuators, multiferroic magnetoelectric (ME) devices, photocatalysis, gas sensors, transparent screens, photonics, spintronics, field-effect transistors, infrared detectors, thermistors, fuel cells, batteries, and solar cells.[1–4]

Thin films and nanostructures of MOs have become essential layers in the design of functional devices. These oxide films and nanostructures are traditionally synthesized by deposition methods utilizing liquid, gaseous, ionized vapor, or plasma precursors.[1,2] Among these options, liquid-precursor-based synthesis methods are attractive due to such attributes as speed, low temperature, being vacuum-free, cost effectiveness, and scaling.[5] Wet-chemical processes, such as the sol–gel technique and metal–organic deposition (MOD), are commonly used for growth of MO thin films. Coprecipitation and hydrothermal methods are more popular for the synthesis of nanostructured MOs. In all of these methods, thermal treatment or annealing of the solution-derived precursor layers or nanostructures is usually necessary to achieve the intended behavior.[6,7] Thermal treatment processes enable: (i) removal of the hydrous skeleton by decomposing the residual solvents and organic binders; (ii) improvement in phase purity and chemical homogeneity; (iii) control of stoichiometry, composition (doping), and concentration/type of defects; (iv) modification of phase structure (amorphous/crystalline) and microstructure (grain size, morphology, orientation, crystal/lattice imperfections, surface roughness, and porosity); (v)

Dr. H. Palneedi, Dr. M. Peddigari, Dr. G.-T. Hwang, Dr. J.-W. Kim, Dr. J.-J. Choi, Dr. B.-D. Hahn, Dr. J. Ryu[+]
Functional Ceramics Group
Korea Institute of Materials Science (KIMS)
Changwon 51508, Republic of Korea
E-mail: jhryu@kims.re.kr, puggy96@hanmail.net
Dr. J. H. Park, Prof. K. J. Lee
Department of Materials Science and Engineering
Korea Advanced Institute of Science and Technology (KAIST)
Daejeon 34141, Republic of Korea
E-mail: keonlee@kaist.ac.kr

[+]Present address: School of Materials Science and Engineering, Yeungnam University, Gyeongbuk 38541, Republic of Korea

Dr. D. Maurya, Prof. S. Priya
Bio-inspired Materials and Devices Laboratory (BMDL)
Center for Energy Harvesting Materials and Systems (CEHMS)
Virginia Tech
Blacksburg, VA 24061, USA
E-mail: spriya@vt.edu
Dr. V. Annapureddy
CSIR-National Physical Laboratory
Dr. K. S. Krishnan Road, New Delhi 110012, India

DOI: 10.1002/adma.201705148

improvement in interfacial bonding of the film/substrate, (vi) reduction of interfacial strain and residual stresses; (vii) enhancement of interparticle bonding or sintering and densification; and (viii) dimensional control of the nanostructures. Oxide films deposited by other synthesis methods using gaseous and ionized vapor or plasma precursors also require thermal treatment for the above-stated purpose.

Conventionally, the thermal treatment of MO films and nanostructures is conducted in an oven or a furnace in the temperature range of 300–1000 °C, depending on the material system, thermodynamics, and the intended effect.[8–10] This process is associated with such issues as high thermal budget (thermal power), long processing times, and high degree of energy loss because sample dimensions are considerably smaller than the heated volume, and almost all of the energy is used to raise and lower the temperature of the substrate and the furnace itself. In addition, this process is incompatible with thermally sensitive substrates (e.g., Si, glass, amorphous alloys, and polymers), where the high temperatures can cause microstructural changes and thermal-expansion mismatch, leading to mechanical failures. Furthermore, thermal treatment processes based on traditional heating methods cannot induce spatially resolved thermal effects, requiring the films or nanostructures to be physically separated from the electronic circuitry. These issues limit the direct integration of MO films or nanostructures into the complementary metal-oxide–semiconductor (CMOS) fabrication process.

As an alternative to the conventional thermal treatment, laser irradiation offers potential solutions to the above issues and enables a highly compatible on-chip integration of MO films and nanostructures. This technique is primarily based on the photothermal effect induced by a focused laser that remotely generates a confined temperature field at a desired position with high controllability.[11] Several laser process parameters, such as laser intensity, pulse width, and scanning rate, can be varied to achieve the desired thermal effect. This process is characterized by significantly fast and localized thermal effects, allowing precise control over the material properties. The heating and cooling rates ($>10^6$ °C s^{-1}) for laser irradiation are orders of magnitude higher than the rates of the conventional annealing and rapid thermal annealing (RTA), enabling rapid fabrication of materials with minimal energy losses. As laser-induced heat can be confined to a specific area in both in-plane and thickness directions, it is possible to selectively anneal the films and nanostructures without any thermal interference with the underlying substrates and adjacent structures. Furthermore, utilization of lasers with sufficient efficiency (defined as the ratio of the optical output power and input electrical power) can result in significant reduction in energy required for thermal processing.[6,12]

Laser-based processing has been utilized in applications ranging from communications to materials processing.[13,14] Traditionally, lasers have played important role in the manufacturing industry for operations such as cutting, welding, patterning, drilling, etc. In recent times, laser processing has found a new avenue in implementation of additive manufacturing and micro/nanofabrication technologies. These new sectors for laser processing have just started to take-off. Currently, excimer laser systems are widely utilized for commercial, large-area device applications, including the fabrication of low-temperature

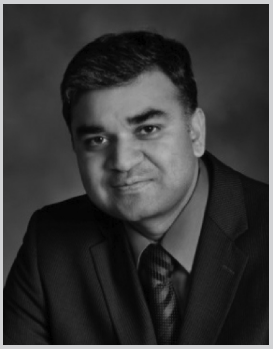

Shashank Priya is currently Robert E. Hord Jr. Professor in the Department of Mechanical Engineering and also serving as Associate Director, Research and Scholarship, in the Institute for Critical Technology and Applied Science. He has made a strong impact in the field of energy harvesting, multifunctional materials, and bioinspired robotics. He is the founder and chair of the Annual Energy Harvesting Workshop series (www.ehworkshop.com) and founding president of the energy-harvesting society (www.energyharvestingsociety.org). He is also serving as member of the Honorary Chair Committee, for the International Workshop on Piezoelectric Materials and Applications (IWPMA).

Keon Jae Lee received his Ph.D. in materials science and engineering (MSE) at the University of Illinois, Urbana-Champaign (UIUC). During his Ph.D. at UIUC, he was involved in the first coinvention of "flexible single-crystalline inorganic electronics", using top-down semiconductors and soft-lithographic transfer. Since 2009, he has been a professor in MSE at KAIST. His current research topics are self-powered flexible electronic systems including energy-harvesting/storage devices, LEDs, large-scale integration (LSI), high-density memory. and laser–material interaction for in vivo biomedical and flexible applications.

Jungho Ryu received his Ph.D. in materials science and engineering at the Seoul National University, Korea in 2001. During his Ph.D and later in his postdoctoral tenure (2000–2003), he studied magnetoelectric composites and piezoelectric materials at the Pennsylvania State University, USA. Prior to joining Yeungnam Univerity in 2018, he was a senior engineer and project leader at Samsung Electro-Mechanics Co. Ltd, (2003–2006) and a principal Researcher at KIMS (2006–2018). His current research interests include the development of piezoelectric and ferroelectric devices, energy harvesting, and functional thin/thick ceramic films.

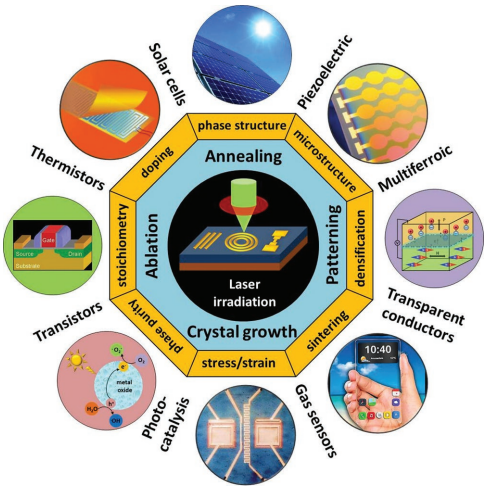

Figure 1. Laser-induced phenomena in metal oxide films and nanostrucutres and their applications in various functional devices. Lasers are used for multiple purposes in the processing of metal oxides, including annnealing, crystal growth, patterning, ablation, and structuring/writing.

poly-Si for high-end thin-film transistor displays and annealing of liquid-crystal display and active-matrix organic light-emitting diode (OLED) backplanes for smartphones and OLED televisions and the manufacture of polymer-based flexible-displays.[15]

Laser systems operating in continuous-wave (CW) or pulsed modes at wavelengths in the ultraviolet (UV), visible (vis), and infrared (IR) ranges have been employed to tailor the properties/functionality of metal oxides. Laser irradiation of a wide variety of MO films and nanostructures has been conducted for their applications in dielectric,[16,17] ferroelectric,[18] piezoelectric,[19] and multiferroic magnetoelectric[20] devices, photocatalysis,[21] gas sensors,[22] transparent conductors,[23] field-effect transistors,[24] solar cells,[25] and thermistors[26] (**Figure 1**). Besides the overarching goal of tailoring of the physical and chemical properties, several interesting phenomena induced by laser irradiation have been reported, e.g., structural distortion and transformation,[27,28] diamagnetic to ferromagnetic switching,[29,30] modification of exchange bias,[31] wettability switching,[32] p-type to n-type conductivity transformation,[33] resistive switching,[34,35] metal-to-insulator transition (MIT),[36] and electrochromic switching.[37]

Over the past decade, laser irradiation has also been employed to replace the conventional thermal treatment for the nucleation and growth of functional MO thin films at low temperatures and on short time scales.[5] Absorption of laser radiation results in rapid photothermal and/or photochemical effects, which influences the crystallization and growth kinetics of thin films. Prior studies have demonstrated the evolution of polycrystalline, textured, and epitaxial microstructures of diverse MO films (e.g., tin-doped indium oxide (ITO), Ga_2O_3, ZnO, TiO_2, VO_2, WO_3, $BaSrTiO_3$ (BST), $Pb(Zr,Ti)O_3$ (PZT), $La_{1-x}Sr_xMnO_3$ (LSMO)) deposited by methods such as chemical solution deposition (CSD),[5,10] pulsed-laser deposition (PLD),[38] and sputtering.[39,40] The large temperature gradients and high diffusion rates during laser processing lead to epitaxial growth rates that are orders of magnitude larger and effective heating times much shorter than that for conventional thermal treatment.[10,19] Furthermore, the laser irradiation technique has been utilized for processing of complex nanostructures, such as site-specific growth of nanowires (NWs) (e.g., ZnO,[41–43] TiO_2[44]) and nanorods (NRs) (e.g., Fe_2O_3,[45] Ag/ZnO[46]), spatial patterning of nanocrystals (e.g., ZnO)[47] and NWs (e.g., Al_2O_3),[48] fabrication of nanosheets (e.g., Fe_2O_3)[49] and clustered nanostructures (e.g., Ag–ZnS@ZnO,[50] Ag/WO_{3-x}[51]), production of oxide nanoparticles (NPs) by laser ablation in liquid (e.g., CuO,[52] MnO_x,[53] $Y_3Fe_5O_{12}$,[54] Ag/TiO_2,[55] $Y_2O_3:Eu^{3+}$, $Gd_2O_3:Eu^{3+}$, $Y_3Al_5O_{12}:Ce^{3+}$ (YAG:Ce),[56] $Fe@Fe_2O_3$, or Fe_3O_4[57]),[58–61] in situ formation of nanocomposites (e.g., Co_3O_4, MoO_2, and Fe_3O_4 particles embedded in graphene, ZnO particles embedded in poly(methyl methacrylate)),[62,63] selective patterning of hybrid electrodes (e.g., Ni/NiO),[64] direct scribing of fine structures (e.g., ITO),[65] and direct writing of microdevices (e.g., TiO_2,[66] Cu/Cu_2O[67]).

Here, we focus on understanding the effects of laser irradiation of MO films and nanostructures for their applications in functional systems and devices. We initially discuss the laser–material interactions, including basic laser principles, photothermal events and their effects, and factors (material characteristics and laser parameters) affecting laser-induced modifications in materials. Subsequently, we provide a comprehensive overview of the laser irradiation of oxide films and nanostructures and its impact on their functionality, performance, and applications. Furthermore, several interesting phenomena, such as ferromagnetic switching, wettability switching, and the metal-to-insulator transition induced by laser irradiation of MO films, are presented. Finally, recent progress and advances in the laser processing of metal oxides pertaining to laser-assisted crystal growth of films, selective growth and patterning of nanostructures, and direct structuring and writing of patterned layouts and microdevices of MOs are discussed.

2. Laser–Material Interactions

2.1. Laser-Induced Events and their Effects

Lasers cover wavelengths ranging from the deep UV to the far IR region (**Figure 2**a). Laser radiation is characterized by monochromaticity, coherence, and collimation, which differentiates it from other light sources.[68] The laser can be operated to deliver very low (≈mW) to extremely high (≈1–100 kW) power with a precise control over its spot size and spatial/temporal distribution.[69] Based on the lasing medium, there are different categories of lasers, including solid-state lasers, liquid-dye lasers, gas lasers, semiconductor lasers, fiber lasers, and free-electron lasers. The wavelength and power of a laser beam are determined by the characteristics of the laser medium and the optical resonator. Lasers have been used in a wide variety of applications, including information processing, medical diagnostics and surgery/therapy, metrology, holography, spectroscopy, and materials processing.[70] Laser-based material processing is a very attractive fabrication approach due to its compatibility with a multitude of materials and its adaptability for roll-to-roll manufacturing. It is possible to digitize the laser process parameters, which facilitates the integration of the process with computer-aided design and a manufacturing system that can be changed on demand.[23]

Laser processing of materials is based mainly on the absorption of laser radiation in the material, which results in various

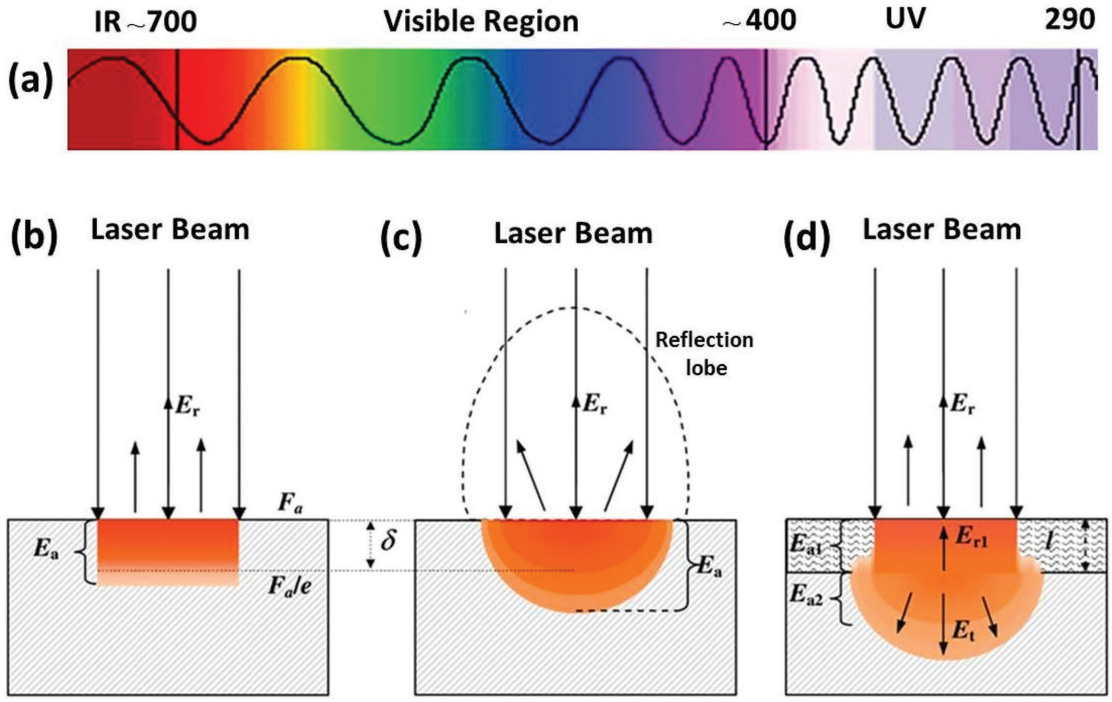

Figure 2. a) Wavelengths used for lasers in the electromagnetic spectrum of light. b–d) Representation of energy redistribution during laser–material interaction: b) absorbing material, c) diffusing material, and d) material with adjacent absorbing and diffusing layers. E_r: reflected energy, E_t: transmitted energy, E_a: absorbed energy. b–d) Reproduced with permission.[71] Copyright 2008, European Cooperation in Science and Technology (COST).

effects, such as heating, melting, vaporization, plasma formation, and ablation. The extent of these effects depends primarily on the characteristics of the laser radiation (laser wavelength, intensity, and interaction time), as well as the optical and thermophysical properties of the material (**Table 1**). The absorption phenomenon is usually associated with the scattering of laser radiation, leading to attenuation and spatial redistribution (diffusion) of the beam energy. The redistribution of laser energy during laser–material interaction is depicted in Figure 2b–d for different absorption scenarios.[71]

The mechanism of photon-energy ($h\nu$) absorption depends on the electronic structure of a material.[72–75] In this instance, h is the Planck constant, and ν is the photon frequency. In insulators and semiconductors with bandgap (E_g), the absorption occurs through resonant excitation involving mainly interband electronic transitions. If $h\nu < E_g$, only weak phonon excitation and absorption are possible. However, interband transitions may occur at higher laser intensities due to sequential multiphoton excitation via defect states or coherent multiphoton excitation. In addition, defect or impurity states often allow sub-bandgap excitation. If $h\nu \geq E_g$, strong interband excitation of electrons will occur, creating electron–hole pairs. The energy from the excited electronic states is transferred to the phonons, which intensifies the lattice vibrations. Intraband transitions in semiconductors or insulators may occur at elevated temperatures due to the availability of more free electrons. The laser-induced interband or intraband electronic transition induces a nonequilibrium electronic distribution that thermalizes the material via electron–electron and

Table 1. Factors affecting the laser–material interactions.

Parameters	Variables
Laser parameters	Working mode (continuous-wave, pulse), wavelength (UV, visible, IR), laser intensity (power/power density, fluence/energy density), interaction/dwell time, angle of incidence, polarization state, beam profile (Gaussian, multimode, flat-top/top-hat), focusing condition (positive, negative), spatial and temporal coherence, spot size, bite size between laser spots, scan speed, pitch distance or line scan spacing, spot overlap rate, scan overlap rate, pulse variables (pulse width/duration, no. of pulses, pulse shaping, frequency, repetition rate)
Material properties	Optical: bandgap, absorbance, transmittance, reflectivity
	Thermal: conductivity, diffusivity, heat capacity, shock resistance, transition temperature, melting point
	Chemical: composition and stoichiometry (defects, impurities)
	Physical: phase structure (amorphous, crystalline), microstructure (morphology, grain size, grain boundaries, crystal/lattice imperfections, surface roughness, porosity), density, ductility/brittleness, thickness, multilayered structures
Others	Substrate properties, sample stage temperature, adhesion/bonding strength of film, processing environment (air/gas/vacuum, liquid, magnetic field, ultrasonic vibration), in situ laser treatment

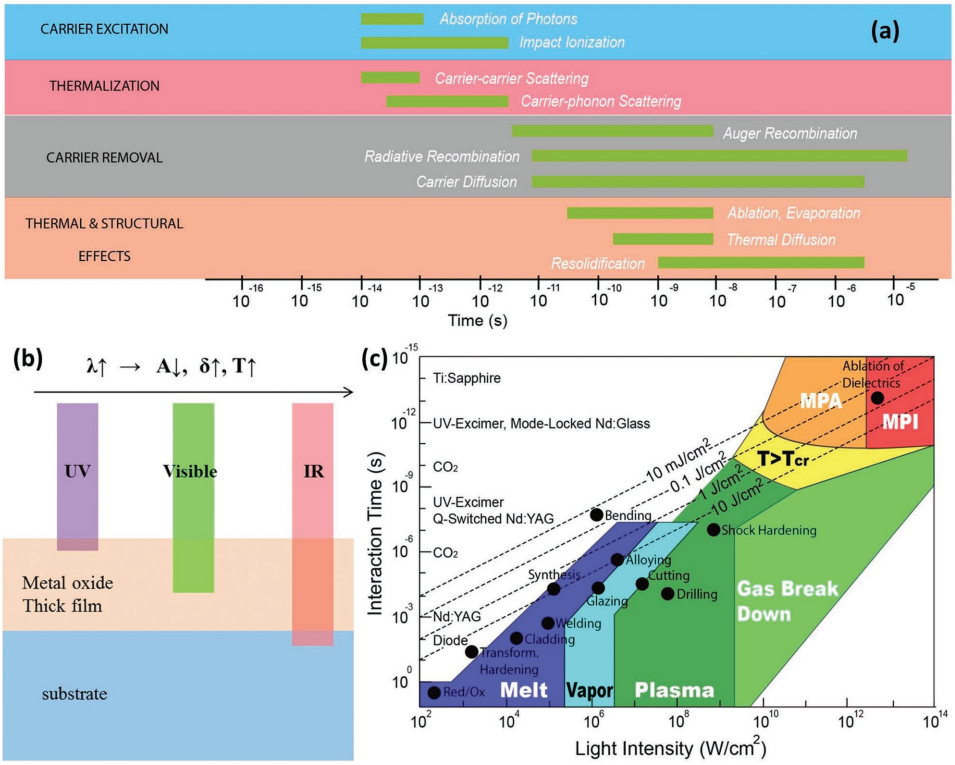

Figure 3. a) Timescales of various energy transitions during laser-induced excitation of a semiconductor material. Reproduced with permission.[77] Copyright 2002, Nature Publishing Group. b) Comparison of optical penetration depths of laser radiation of different wavelengths in a metal oxide film (≈1–10 µm thick). The UV-laser radiation exhibits stronger absorption but lower optical penetration depth in metal oxide films compared to visible and IR lasers, which transmit more deeply into the oxides. Reproduced with permission.[20] Copyright 2017, Wiley-VCH. c) Illustration of the various laser-induced thermal effects and material-processing applications. The light intensities and interaction times shown in the figure refer to different types of lasers. Reproduced with permission.[78] Copyright 2011, Springer-Verlag. *A*: absorbance, *δ*: laser penetration depth, *T*: transmittance, MPA/MPI: multiphoton absorption/ionization, and T_{cr}: critical temperature.

electron–phonon interactions. The electron–hole recombination process reestablishes the equilibrium condition on a time scale that depends on the material characteristics.[76] The overall effect is the conversion of electronic energy derived from the beam of the incident laser into heat.

The electron and lattice excitation and relaxation processes in a semiconductor material can be distinguished based on the timescales of the corresponding phenomena. Such categorization includes four regimes: (i) carrier excitation, (ii) thermalization, (iii) carrier removal, and (iv) thermal and structural effects (**Figure 3**a). These processes do not occur sequentially but overlap in time, forming a continuous chain of events spanning the entire range from femtoseconds (fs) to microseconds (µs). Various mechanisms of the electron and lattice dynamics represented in the four regimes have been described in the literature.[77] The dominant mechanism depends on the wavelength, intensity, and interaction time of the laser, as well as the electronic structure and the optical properties of the material.

2.2. Factors Affecting Laser–Material Interactions

Lasers can be operated in either the continuous or the periodic mode, depending upon whether their power output is continuous over time or takes the form of pulses on one or another time scale.[68,74] CW laser beams can be shuttered mechanically at some rate to produce pulses of light with short emission times, which are classified as quasi-CW lasers. Laser processing of materials typically involves selection of an appropriate laser system and processing parameters, arrangement of the optics for controlling the laser beam, and an experimental setup for focusing the laser beam over the target area of the material followed by irradiation under the desired conditions. The optical and thermal properties of materials should be considered carefully for the selection of appropriate laser parameters. Some of the factors (Table 1) influencing the laser–material interactions with respect to semiconductors and insulators are discussed in this section.

2.2.1. Laser Wavelength

The basic wavelength of a laser beam is determined by the atomic energy level of the lasing medium. However, it is possible to change the laser wavelength by employing nonlinear optics in the resonator cavity. The intensity of the laser radiation is attenuated inside the material in accordance with the Beer–Lambert law: $I(z) = I_0\ e^{-\alpha z}$, where I_0 is the laser intensity just below the surface after considering the reflection loss, $I(z)$ is the intensity at depth z, and α is the absorption

coefficient of the material.[71,78,79] The penetration depth (δ) of a particular wavelength of light radiation is related to the absorption coefficient of the material according to expression: $\delta = \frac{1}{\alpha} = \frac{\lambda}{4\pi k_e}$, where k_e is the extinction coefficient.[80] Furthermore, α is dependent on the thickness (t) and optical properties of the materials as per the relationship, $\alpha = -\frac{1}{t}\ln\left(\frac{T}{1-R}\right)$, where T and R are the transmittance and reflectance of the material.[81] In metals, which are nontransparent to almost all laser wavelengths and exhibit high α values, the extent of laser penetration is quite limited. On the other hand, laser energy may be absorbed over a considerable depth during its transmission in semiconductors and insulators.[82]

As discussed above, the incident photon should have energy equal to or higher than the bandgap of the semiconductor or insulator material for effective absorption. Most studies on MO thin-film fabrication have employed high-energy, short-wavelength UV lasers, as these oxides typically exhibit much higher absorbance in the UV range than in the vis and IR regions. However, the absorption of UV laser radiation, owing to its shallow penetration depth, is limited to film thicknesses in the range of 200–300 nm (Figure 3b).[20,68] The full transparency of low-energy, long-wavelength IR laser radiation, in MO films, is likely to cause thermal damage to the substrate and interfacial reactions. In case of MO thick films (>1 μm) that are semitransparent to visible light, the laser radiation is absorbed mainly by the intermediate layers of the film, and its lower and surface layers are heated up indirectly by thermal diffusion.[83,84] Therefore, visible laser radiation is expected to be adequate for selective irradiation of MO thick films without disturbing the substrate. Although thicker MO films can absorb additional visible laser radiation, their limited transmittance may not allow the dissipation of laser-induced heat to their whole depth, above an optimum thickness level.[20] Since the optical transmittance of the film changes with its thickness, IR laser radiation may be a suitable choice for thermal treatment of much thicker (>10 μm) MO films. The efficiency of the laser irradiation of MO films and nanostructures depends greatly on their optical absorbance in the chosen laser wavelength range.

2.2.2. Laser Intensity

Laser-assisted heating with intensity (or fluence) lower than the threshold of melting can trigger a variety of temperature-dependent processes. The high temperatures generated can induce phase and microstructural modifications and enhance sintering and densification of materials.[7,85] The localized laser heating causes large temperature gradients that can induce self-quenching of the material, thermal stresses, and thermoelastic excitation of acoustic waves, resulting in non-equilibrium structures, surface hardening, bending, and cracking.[73] A laser fluence above the threshold for melting can create transient pools of molten matter on the surface. Above the ablation threshold, material evaporation/exfoliation and sublimation will occur. Figure 3c provides an overview of the various laser processing regimes and their applications based on the laser intensities employed and the interaction times for several kinds of lasers.[78]

2.2.3. Laser Interaction Time

The thermal diffusion length indicates how far the energy spreads during the laser irradiation time, which can be the laser-beam dwell time (spot size/scan speed for CW lasers) or pulse width in a practical case. The heat generated by CW laser irradiation can penetrate deeply into a material due to its long irradiation times (typically >1 μs).[86] This practical characteristic of thermal impact enables fast annealing, welding, and cutting of diverse materials. However, it is not ideal for devices that require thermal interactions nearer to the surrounding electronics (or other heat-sensitive materials) and minimal reoxidation during photothermal reduction.[87]

The motivation behind using a pulsed laser is the reduction of gradual and deep thermal reactions in the material. A pulsed laser is preferred in all types of laser processing that demand high heating/cooling rates and well-defined localized energy input to the solid. A pulsed laser facilitates high self-quenching rates (solidification-front velocities up to several m s^{-1}) by drastic heat dissipation to the cooler surrounding material, enabling freezing of defects and supersaturated solutes, as well as the formation of metastable material phases. Pulsed lasers are especially effective for reducing the ablation threshold intensity or precise processing. At a constant average power, a high-peak pulse energy with a short pulse width can be used for rapid material ejection. In this case, the excited material has less time to transfer energy to the surrounding environment before being ejected, which reduces the heat-affected zone.

2.2.4. Repetition Rate

The repetition rate implies the number of pulses per second, which determines the mean laser power through the equation: $P_M = E_P \times f_{pulse}$, where P_M is the mean laser power, E_P is the pulse energy, and f_{pulse} is the pulse repetition rate. The repetition rate can thus control the overall heat input into the material (assuming laser energy per pulse, E_p, is constant) with a possible heat-accumulation effect, enabling effective crystallization, and fast laser processing such as welding, cutting, and drilling without severe thermal damage.[79,88] If the repetition rate is overly low, the energy loss by heat conduction dominates, and most of the energy will not be used for laser processing.[69] Additionally, an overly high repetition rate can cause a particle shielding effect when ablated particles or the flume is located in the region of the next laser radiation.[78] This effect can lead to plasma ignition above the workpiece, which creates an additional heat source close to the surface of material. However, particle shielding can be reduced to a certain extent by fume extractors.

2.2.5. Overlap Rate

During raster scanning of lasers over a target area, two types of overlapping, namely spot overlap and scan line overlap, are

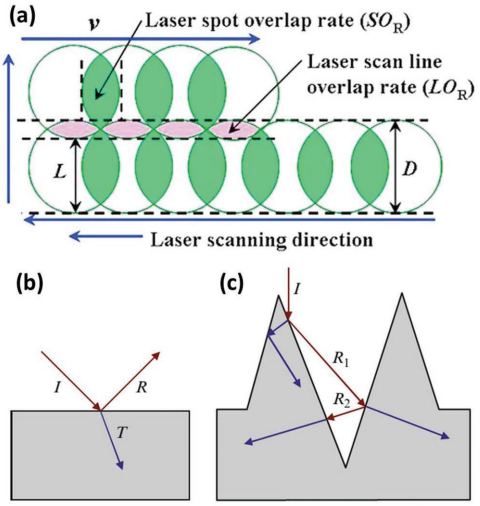

Figure 4. a) Schematic description of laser spot overlap rate (SO_R) and laser-scan-line overlap rate (LO_R). Controlling the pitch distance (separation between laser scan lines) and scan overlap rate is necessary for effective laser annealing and inducing desired effects. Reproduced with permission.[92] Copyright 2016, Elsevier Ltd. b) Light reflecting specularly from a flat surface. c) Light trapping due to multiple reflections from protruding structures on a rough surface, which enhances its coupling into the material. Furthermore, refraction causes the light to propagate at oblique angles, increasing the effective optical path length. b,c) Reproduced with permission.[72] Copyright 2010, Springer-Verlag.

usually observed (**Figure 4**a).[89–92] The corresponding overlap rates include the laser-spot overlap rate (SO_R) and the laser-scan-line overlap rate (LO_R). These overlaps depend on the beam spot size, the bite size between laser spots, the pulse repetition rate, the scanning speed, and the pitch distance or line-scan spacing. With higher SO_R or LO_R, the material surface undergoes more laser irradiation doses per unit area. However, the SO_R or LO_R that is too high can lead to excessive laser-beam energy per unit area, that will cause damage to the material. However, an SO_R or LO_R that is too low will result in a relatively gentle heating and thus cause unapparent changes in the properties of the material.

2.2.6. Thermal Conductivity of the Material

Thermal conductivity plays a crucial role in transporting heat through a given material. In dielectric solids, the conduction of heat is primarily due to the movement of phonons that persists until the phonons are scattered either through phonon–phonon interactions or at lattice imperfections.[93] The thermal conductivity (k) of a solid is expressed as $k = \left(\frac{1}{3}\right) C_p v l$, where C_p is specific heat, v is phonon velocity in the solid, and l is the phonon mean free path. Typically, materials with low thermal conductivity have low thermal diffusivity. Therefore, ceramics with low thermal conductivity may confine laser-induced heat, establishing a narrow temperature distribution within the material. Thus, if the melting temperatures of the solids are similar, laser processing can create small heat-affected zones and melt zones in materials with low thermal conductivity. Since heat is not well transferred to surrounding areas for ceramics with low thermal conductivity, a low cooling rate will be achieved and can induce slow recrystallization of the molten zone, which ultimately will define the composition and structure of the laser irradiated material.

2.2.7. Phase Structure and Microstructure of the Material

Both the phase structure and the microstructure of materials significantly influence laser-induced thermal effects. In the case of partially crystalline nanomaterials, the high density of grain boundaries increases the phonon scattering and decreases the phonon mean free path, which consequently decreases the thermal conductivity. The thermal conductivity of the material will decrease in the amorphous phase due to the structural disorder that destroys the coherence of lattice vibrations and limits the phonon mean free path.[94] Hence, the transfer of laser-induced heat in amorphous and partially crystalline materials will be constrained to smaller distances. Pores in the microstructure of metal oxide films will affect the absorption of UV laser radiation.[95] For dense precursor films, the incident UV laser and thermal transport cannot reach the bottom of the film (≈2 µm thick) sufficiently because of the shallow penetration of UV wavelengths. However, in the porous films, the voids present between the particles will allow the laser irradiation to reach deep into the film. Laser-induced defects such as vacancies, broken bonds, and molecular fragments can also affect the optical absorption behavior.

2.2.8. Surface Roughness of the Material

Multiscale surface texturing can cause considerable deviations in how light is scattered and reflected, leading to high absorption of the laser compared to the absorption of a flat smooth surface (Figure 4b,c).[72] This enhancement can be explained by noticing that protruding structures can reflect and scatter the laser beam back into the surface. The laser beam can be guided to interact with holes and crevices through multiple internal reflections, guiding the laser beam into the bulk material and enhancing the coupling. Refraction at the surface of these features also induces transmission at oblique angles, which effectively increases the optical path length and light absorption. The degree of enhancement relies on the specific dimension and geometry of the surface.[96] Creating features near the surface with dimensions on the order of a wavelength (e.g., surface roughness, cracks, and voids) also affects the surface reflectivity, which can increase the optical path length and laser absorption.[97] This is particularly important for improving light absorption of MO thin-film devices where the MO film thickness is on the order of the laser wavelength.[98]

2.2.9. Process Environment

In laser processing, a vacuum or an inert gas environment is often employed to avoid film contamination at the laser-interaction zone by eliminating adversely affecting contaminants, such as moisture and oil/grease.[80] The shielding gas has

additional functions such as acceleration of a reducing reaction, suppression of plasma, and morphology control by varying gas species (e.g., Ar, He, N_2, CO_2, and H_2) and pressure.[79,99–101] In the case of laser cutting of semiconductor solar-cell wafers, liquid-assisted laser ablation was found to be better compared to air-assisted laser ablation as it can eliminate the recasting effect, minimize the debris redeposition, and generate a clean surface without any need of post-treatment. Furthermore, laser cutting in ethanol–water mixtures results in a better cut quality than laser cuts performed in pure water, but leads to a lower cutting efficiency.[102] A magnetic field with specific orientations (e.g., vertical and parallel) applied during laser irradiation can change the surface morphology, microstructure, and grain size of MOs due to the magnetic force induced on the ferromagnetic elements.[103,104] A preheating process can be used to reduce thermal stress induced during laser heating and the light intensity requirement for appropriate interactions.[105] Incorporating a light-absorbing layer can efficiently convert the laser radiation into heat energy.[44,106] Finally, the agglomeration of the MO film during laser interaction can be prevented by introducing ultrasonic vibration to the oxide materials.[107]

2.2.10. Substrate Properties

Appropriate material selection and pretreatment of the substrate are important in many types of laser–material interactions.[78,108] In the case of MO thin films on an insulating transparent substrate, the critical intensities for laser interactions, such as melting and ablation, are considerably lower than the critical intensity for the film on a thermally conductive substrate. A substrate with a high thermal diffusivity can induce a large temperature gradient at the interface, which can generate thermal stress and crack formation on the film.[109,110] A large difference in the thermal-expansion coefficient between the film and substrate can cause microcracks during rapid laser heating and cooling. A high chemical stability of the substrate prevents interface reactions that change the film stoichiometry. A low lattice-constant mismatch between the substrate and the film can induce an oriented and large-grain film during the laser crystallization process. In addition, the surface quality of the substrate (i.e., roughness, surface oxides, and crystallographic orientation) influences the laser-induced surface temperature and the film reliability due to photothermal stresses. Finally, the temperature of the substrate can affect the optical properties of MOs through changes in the permittivity, band structure, plasma oscillations, or material phase.[111]

3. Laser Irradiation of Metal Oxides and their Applications

3.1. Dielectric, Ferroelectric, and Piezoelectric Systems

Dielectric, ferroelectric, and piezoelectric ceramic films have been used widely in a variety of microelectronic devices for applications in capacitors, sensors, actuators, transducers, memories, and energy harvesters. In recent years, considerable research has investigated the low-thermal-budget processing of electroceramic perovskite films for their direct integration into CMOS circuitry and flexible electronics. Conventional high-temperature thermal treatment conducted for functional activation of perovskite films generally requires them to be separated physically from the circuitry. In this context, laser irradiation appears as a potential alternative because laser irradiation exhibits a significantly fast and localized thermal effect without any interference with the underlying substrates or surrounding circuitry. Many studies have been conducted on the laser irradiation of dielectric, ferroelectric, and piezoelectric ceramic films for different purposes.[16–19,112–119] Representative findings of some of these studies on laser irradiated electroceramic films are discussed below.

During fabrication of conventional multilayer ceramic capacitors based on $BaTiO_3$ (BTO) with Ni-electrodes, sintering of BTO layers is normally conducted at elevated temperatures (≈1300 °C) under strongly reducing conditions ($pO_2 < 10^{-10}$ atm) to avoid oxidation of the base metal electrodes.[16] Next, the dielectric layers are reoxidized in a $pO_2 \approx 10^{-8}$ atm at lower temperatures (≈800–900 °C) to reduce the dielectric loss and increase the breakdown strength. A similar procedure is followed in the case of BTO films deposited on the base metal foils. The reoxidation process is kinetically controlled and should be well-optimized. Otherwise, incomplete oxidation of BTO or partial oxidation of the substrate will degrade the properties of the capacitor. Bharadwaja et al.[16] considered laser-assisted reoxidation as an alternative approach to modulate the oxidation kinetics of dielectric films. The UV excimer laser-assisted oxidation of BTO thin films on Ni foils can be achieved at modest temperatures (<350 °C) and high oxygen partial pressures (10^{-3} mTorr range). The BTO films (200 nm thick) on preannealed (10^{-19} atm) Ni foils were processed by repeated sol–gel coating and RTA in N_2 at 700 °C. Finally, these films were crystallized under $pO_2 \approx 10^{-14}$ atm (in 95% N_2/5% H_2) at 900 °C for 1 h. The as-crystallized films, prior to oxidation, exhibited the perovskite phase without any NiO formation (from X-ray diffraction (XRD) analysis). Reoxidation of the samples was conducted in a chamber filled with an O_2/O_3 (90/10) mixture, using a KrF excimer laser (248 nm, 50 mJ cm^{-2}, 24 ns). As-reduced and non-oxidized thin-film samples exhibited dielectric losses exceeding 200%, while the samples progressively became better insulators as the reoxidation proceeded. Under optimized conditions, the laser-reoxidized BTO film on Ni showed a dielectric permittivity of ≥1000 and a loss tangent of <2%, which were even better than those obtained through the conventional reoxidation approach (**Figure 5**a).[16] Oxygen stoichiometry of the laser reoxidized BTO film (Figure 5c) was determined from electron energy-loss spectroscopy data collected across its thickness direction using transmission electron microscopy (TEM) (Figure 5b).[16] It was observed that the laser-assisted reoxidation of the BTO film resulted in good oxygen stoichiometry (≈2.95–3.00), whereas the as-reduced BTO film was strongly oxygen-deficient (≈2.8) over the depth of the film. The reoxidation kinetics were hypothesized to be governed by the complex interplay between: (i) local temperature and elastic pressure gradients inside the film, (ii) laser-induced photolysis of oxygen/ozone gas molecules, and (iii) structure and property changes in the film as reoxidation continues.

Laser-induced transformation of amorphous to crystalline phase has been demonstrated in many studies to stimulate the functional activity of electroceramic perovskite

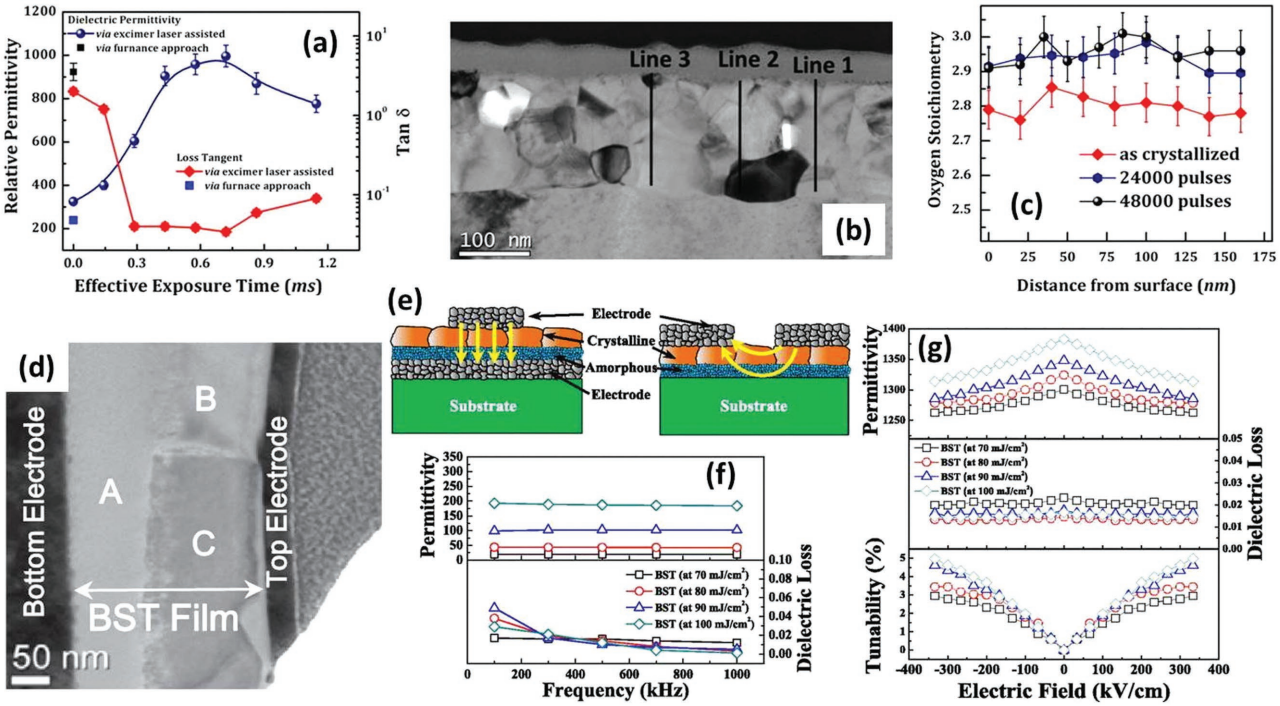

Figure 5. a) Variation of dielectric permittivity and loss tangent in laser-assisted reoxidized $BaTiO_3$ films on Ni foil as a function of effective laser exposure time (product of number of pulses and pulse width). b) Cross-sectional view of the sample with three indicator lines for the chemical analyses across the film thickness. c) Oxygen stoichiometry of the samples across the film thickness. The estimated oxygen stoichiometry was 2.95–3.00 in the laser-assisted reoxidized films and 2.8 for the films as-crystallized in reduced oxygen pressures. a–c) Reproduced with permission.[16] Copyright 2016, AIP Publishing LLC. d) TEM image of a $Ba_{0.6}Sr_{0.4}TiO_3$ thin film crystallized using a laser energy of 100 mJ cm^{-2}. e) Schematics of MIM and planar-type capacitors made using laser annealed BST films. f) Dielectric properties of MIM capacitors. g) Dielectric properties and tunabilities of planar type capacitors. d–g) Reproduced with permission.[17] Copyright 2012, American Institute of Physics.

films.[17,114,115,117,119] The degree of crystallization of the amorphous film and the fraction of functionally active material resulting from laser irradiation was found to significantly influence the properties of the film. The limited laser-absorption depth and the temperature inhomogeneity across the thickness, coupled with extremely short heating times during laser irradiation have been considered the main sources for the partially crystallized layers.[114,119] In the case of laser-annealed $Ba_{0.6}Sr_{0.4}TiO_3$ films, Kang et al.[17] observed a strong dependence of out-of-plane dielectric properties of the film on the residual amorphous phase. The BST films (300 nm thick) were deposited on $Pt/Ti/SiO_2/Si$ substrate by sol–gel coating and crystallized using a KrF excimer laser (70–100 mJ cm^{-2}, 200 pulse). Crystallinity and grain size of the films increased with increasing laser energy. However, an amorphous layer was observed near the film/substrate interface (Figure 5d, A: amorphous, B and C: crystalline). As shown in Figure 5e, a metal–insulator–metal (MIM) and a single-gap planar capacitor were fabricated using the laser annealed BST films to measure their out-of-plane and in-plane permittivities, respectively. The effective capacitance was estimated by considering the capacitance of the amorphous region, acting in series and parallel with the crystalline layer capacitance of the MIM and planar structures, respectively. In both structures, the relative permittivity and dielectric tunability were found to increase with increasing laser energy due to the improved crystallinity and grain growth (Figure 5f,g).[17] The permittivity values measured along the in-plane (ε_r = 1383) and out-of-plane (ε_r = 184) directions were found to be significantly different. These results indicate that the residual amorphous layer shows a greater influence on the dielectric properties along the out-of-plane direction.

Despite the promising benefits of using laser radiation for crystallization and densification of amorphous precursor films, careful control over different laser processing parameters is required to avoid damage to the constitutive materials.[114,119] Therefore, specific thermophysical and photothermal parameters should be considered in the design of the laser-irradiation process. In an attempt to optimize the laser processing conditions for annealing of $PbZr_{0.4}Ti_{0.6}O_3$, Xianyu et al.[18] investigated the effects of environment, substrate temperature, laser energy, and number of laser pulses on the ferroelectric behavior of PZT films deposited on $Pt/Ti/SiO_2/Si$ substrates. The sol–gel films synthesized and heat-treated at 550 °C, 10 min, in O_2 (160 nm thick) were irradiated with a XeCl excimer laser (308 nm). XRD analysis of the PZT films suggested that the formation of the pyrochlore phase occurs at all laser energy levels (150–750 mJ cm^{-2}, 1 pulse, substrate at room temperature (RT)) in air, which was not the case with the N_2 atmosphere (150–190 mJ cm^{-2}, 100 pulse, substrate at 400 °C). This behavior was also resembled in the scanning electron microscopy (SEM) images of the corresponding PZT film surface (**Figure 6**a,b). The polarization hysteresis behavior of the PZT film was also greatly dependent on the laser energy

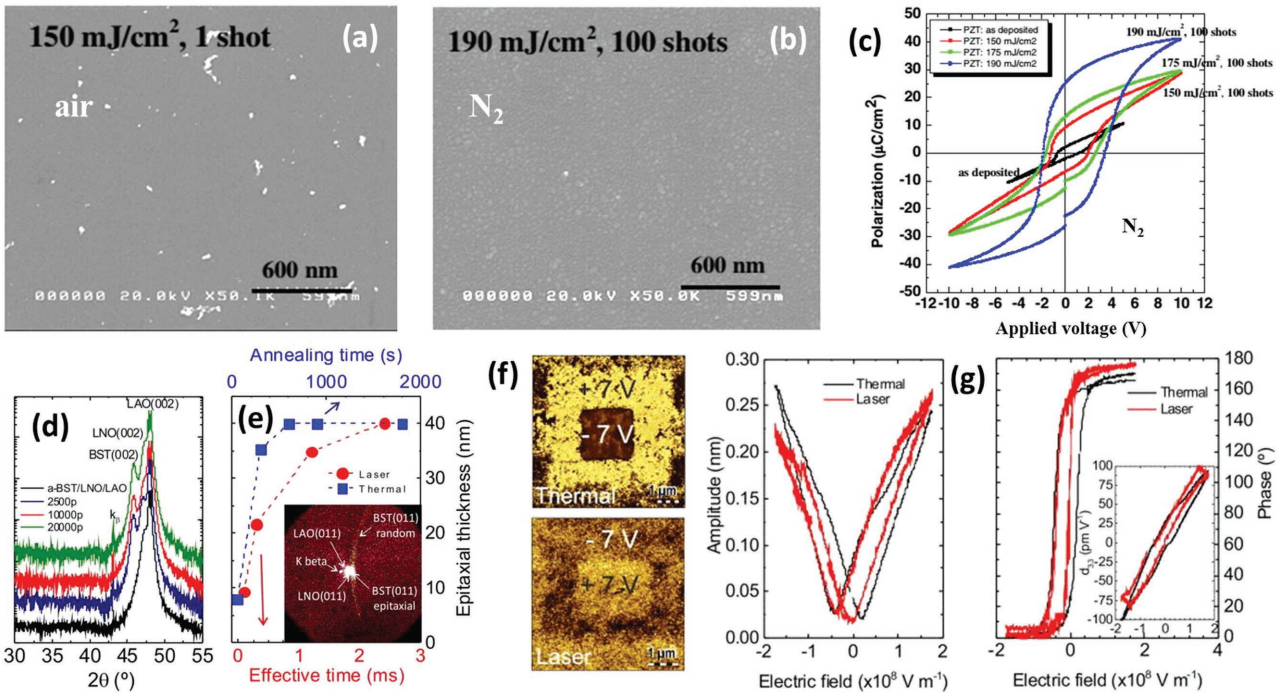

Figure 6. a,b) SEM images of PZT film surfaces after laser irradiation in air and N_2, respectively. c) Polarization–electric-field (*P*–*E*) loops of PZT films before and after laser annealing in N_2. a–c) Reproduced with permission.[18] Copyright 2005, Materials Research Society. d) X-ray diffractograms of a rapid thermally annealed $BaSrTiO_3$ (BST) film, as well as the samples laser irradiated with different number of accumulated pulses. e) Calculated epitaxial thickness of BST samples obtained by laser treatment and thermal annealing. Inset: 2D XRD data used for the quantification of the epitaxial fraction of the BST film (40 mJ cm^{-2}, 2500 pulses). f,g) PFM characterization of thermally annealed (900 °C, 14 400 s) and laser irradiated (40 mJ cm^{-2}, 10 000 pulses) BST films: f) phase-switching images obtained by applying ± 7 V and g) amplitude–electric-field butterfly and phase–electric-field hysteresis loops. Inset: d_{33} constant as a function of the electric field. d–g) Reproduced with permission.[19] Copyright 2015, AIP Publishing LLC.

density (Figure 6c).[18] A low-energy, multishot laser irradiation in a N_2 atmosphere was found to be more effective in producing high-quality perovskite PZT films.

From studies on crystal growth of CSD-derived amorphous oxide films, Tsuchiya and co-workers identified that during conventional thermal annealing, while epitaxial nucleation emerges at the substrate interface, polycrystalline nucleation can also occur at random locations in the precursor film.[5] At sufficiently high temperatures, the epitaxial domain, stabilized by the single-crystal substrate, eventually consumes the polycrystalline sections, and a single, uniform epitaxial thin film is obtained. By contrast, studies have demonstrated that laser-assisted epitaxial crystal growth proceeds via highly selective nucleation, as discussed later in Section 5.1. Recently, a comparative study was conducted by Queraltó et al.[19] on the structural, ferroelectric, and piezoelectric properties of $Ba_{0.8}Sr_{0.2}TiO_3$ epitaxial films crystallized by laser irradiation and rapid thermal annealing. The CSD-derived amorphous BST film (40 nm thick) on $LaNiO_3$ (LNO)-buffered $LaAlO_3$ (LAO) substrate was laser irradiated (Nd:YAG, 266 nm, 40 mJ cm^{-2}, 3 ns, 10 Hz) in air with a substrate temperature of 400 °C, and RTA of the film was done at 900 °C for 60–1800 s in oxygen flow. Conventional XRD measurements indicated the crystalline evolution of BST after laser irradiation and an increase in intensity of the epitaxial BST peak due to the accumulation of laser pulses (Figure 6d). 2D XRD analysis revealed heterogeneous nucleation of BST at the interface with LNO, in addition to homogeneous nucleation in other regions of the film (incomplete ring in the inset of Figure 6e). From the quantification of the fraction and the thickness of epitaxial BST using 2D XRD data, the epitaxial growth of BST in laser irradiated films was found to be significantly faster in comparison to films thermally annealed by conventional means (Figure 6e). This finding was attributed to the development of large temperature gradients and fast diffusion rates during laser processing. In addition, the rapid heating rates of laser irradiation are likely to prevent excessive coarsening of random orientations, contributing to a fast epitaxial growth.[10] Microstructural analysis of the BST/LNO/LAO sample indicated that the BST film was completely epitaxial. The ferroelectric switching and piezoelectric response of the laser irradiated BST film were relatively like the ferroelectric switching and piezoelectric response obtained for thermally annealed film (Figure 6f,g).[19] Faster growth of crystalline epitaxial films through laser irradiation made it more attractive than conventional thermal annealing.

3.2. Multiferroic Magnetoelectric Systems

The magnetoelectric response quantified in terms of the ME voltage coefficient (α_{ME}) represents the efficiency of coupling between magnetic and electric domains in a multiferroic ME material. In composites, ME coupling occurs predominantly through the interfacial strain transfer between piezoelectric

and magnetostrictive components. Film-based ME composites are highly desired for on-chip integration of devices. Recently, Palneedi et al. investigated the ME properties of laser annealed PZT thick films deposited on a magnetostrictive amorphous Metglas (FeBSi alloy) foil by the granule spray in a vacuum (GSV) technique.[20,83,84] The PZT/Metglas composite system was chosen for its promising ME performance due to the large piezoelectric constant (d_{ij}) of PZT and the high piezomagnetic coefficient (q_{ij}) of Metglas (since $\alpha_{ME} \propto d_{ij} \cdot q_{ij}$).

Conventional furnace annealing (usually over 600 °C) of the PZT film[120,121] on a thermally sensitive amorphous Metglas ($T_{crystal} \approx 510$ °C) substrate leads to crystallization and oxidation of Metglas along with interfacial chemical reactions between PZT and Metglas. To overcome these problems, Palneedi et al.[83] adopted a unique fabrication approach involving the room-temperature deposition of the PZT film (4 µm thick) by the GSV technique followed by its localized annealing with laser radiation (CW, Yb laser, 560 nm, 220 mW, 0.05 mm s^{-1}). Since GSV-deposited PZT is semitransparent to visible light, the laser radiation will be absorbed mainly by the intermediate layers of the PZT film, and its lower and upper layers will be heated up indirectly by thermal diffusion. The coexistent amorphous and nanocrystalline phases in the PZT film were hypothesized to limit the phonon mean path and confine the laser radiation within the film. The laser radiation could be absorbed selectively within the thickness of the PZT film without causing any thermal damage to the Metglas substrate. The enhanced dielectric constant, ferroelectric polarization, and ME coupling (**Figure 7**a) of the laser annealed PZT/Metglas system were attributed to the improved crystallinity and grain growth in the PZT film (Figure 7b). The improved crystallinity reduces the dielectric loss factor and stabilizes the ferroelectric polarization while grain growth promotes the domain mobility.

In another study, Palneedi et al.[84] investigated the annealing behavior of a 2 µm thick PZT film deposited on Metglas using a CW, Nd:YAG laser (532 nm) with varying laser energy (210–390 J mm^{-2}, 0.1 mm s^{-1}). The ME response of the composite increased with increasing laser energy up to 345 J mm^{-2} and decreased thereafter (Figure 7c), contrary to the changes in dielectric and ferroelectric properties with the laser energy. Microstructural observation using TEM indicated that the crystallinity of the PZT film increased with increasing laser energy. However, the laser radiation started penetrating beyond the PZT layer at 345 J mm^{-2} and crystallized the whole of the Metglas substrate at 390 J mm^{-2} (Figure 7d), causing a decrease in the ME output of the composite. Since the laser–material interactions occur instantaneously, the simultaneous structural (amorphous to crystalline) and size (grain growth) evolutions in the PZT film during laser irradiation should be conducive to concurrent improvement in its thermal conductivity and thus augment the heat transport. Therefore, above a certain level of laser fluence, the greater amount of heat generated may spread beyond the PZT layer due to the enhanced thermal diffusion.

Recent laser annealing studies on the PZT/Metglas composite system have demonstrated excellent ME properties.[20] The strong dependence of the ME output of the composite on the thickness (2–11 µm) of the PZT film (Figure 7e) has been attributed to the differences in the degree of crystallinity and the extent of annealing of the PZT films by laser radiation (CW, Yb laser, 560 nm, 220 mW, 0.03 mm s^{-1}). Optical characterization of the PZT films revealed that while the penetration depth of the laser radiation increased, its extent of penetration decreased with increasing PZT film thickness (Figure 7f). Since GSV-deposited films possess both amorphous and nanocrystalline phases, the thicker PZT films with a higher volume fraction of the amorphous phase exhibited lower thermal conductivity, resulting in a constrained dissipation of laser-induced heat in thicker films, which is not sufficient to anneal the layers closer to the Metglas substrate. Microstructural analysis of PZT/Metglas indicated that the PZT films were fully annealed up to a thickness of 6 µm, above which they were only partially annealed. It may be possible to fully anneal PZT films thicker than 6 µm using a higher laser energy. The increase in crystallinity and grain growth at higher temperature/heat induced by higher laser energy will improve the thermal conductivity, which augments the heat transport and spreads it to deeper layers of the film. By exploiting the material and process parameters, near-theoretical magnetoelectric output (7 V cm^{-1} Oe^{-1}) has been shown to be obtained in laser annealed PZT/Metglas film composites.

3.3. Transparent Conductors

Transparent and conductive oxide (TCO) films find applications in optoelectronic devices, such as displays, touch screens, light-emitting diodes, photovoltaics, and smart windows.[122] The TCOs deliver or collect electrons to or from the active layer of the optoelectronic device, while at the same time allowing visible light to pass through relatively unimpeded.[23] High optical transmittance and low sheet resistance are the main requirements for transparent electrodes in these devices. While ITO is the most popular TCO, other contenders include In/Al/Ga-doped ZnO, In-doped CdO, and F/Sb-doped SnO_2. Laser irradiation has been utilized in many studies to modify and fine-tune the optical and electrical properties of TCO films.[23,91,123–125]

Tsuchiya et al.[126] demonstrated a significantly low resistivity in ITO films through microstructure control assisted by photoirradiation. ITO films prepared by spin-coating of ITO NPs on a SiO_2 substrate were photoirradiated by a two-step treatment, first using a Xe excimer lamp (in air) and then with a KrF excimer laser (in N_2). Initial irradiation with the lamp was conducted to improve the adherence between ITO NPs and substrate as well as to prevent ablation of the film observed in the case of direct laser exposure. **Figure 8**a,b shows the atomic force microscopy (AFM) images of the film surface obtained after conventional annealing (500 °C, N_2) and two-step photoirradiation, respectively. Small grains with pores were observed in the former case while big grains with some cracks were observed in the latter case. Compared to conventional annealing and direct laser irradiation, the two-step photoirradiation resulted in lower electrical resistivity (3.33×10^{-3} Ω cm) of the ITO film. It was also found that the resistivity of the film depends on its thickness. Based on the idea that the absorption of laser energy is strongly influenced by ITO layer thickness, an optimized condition

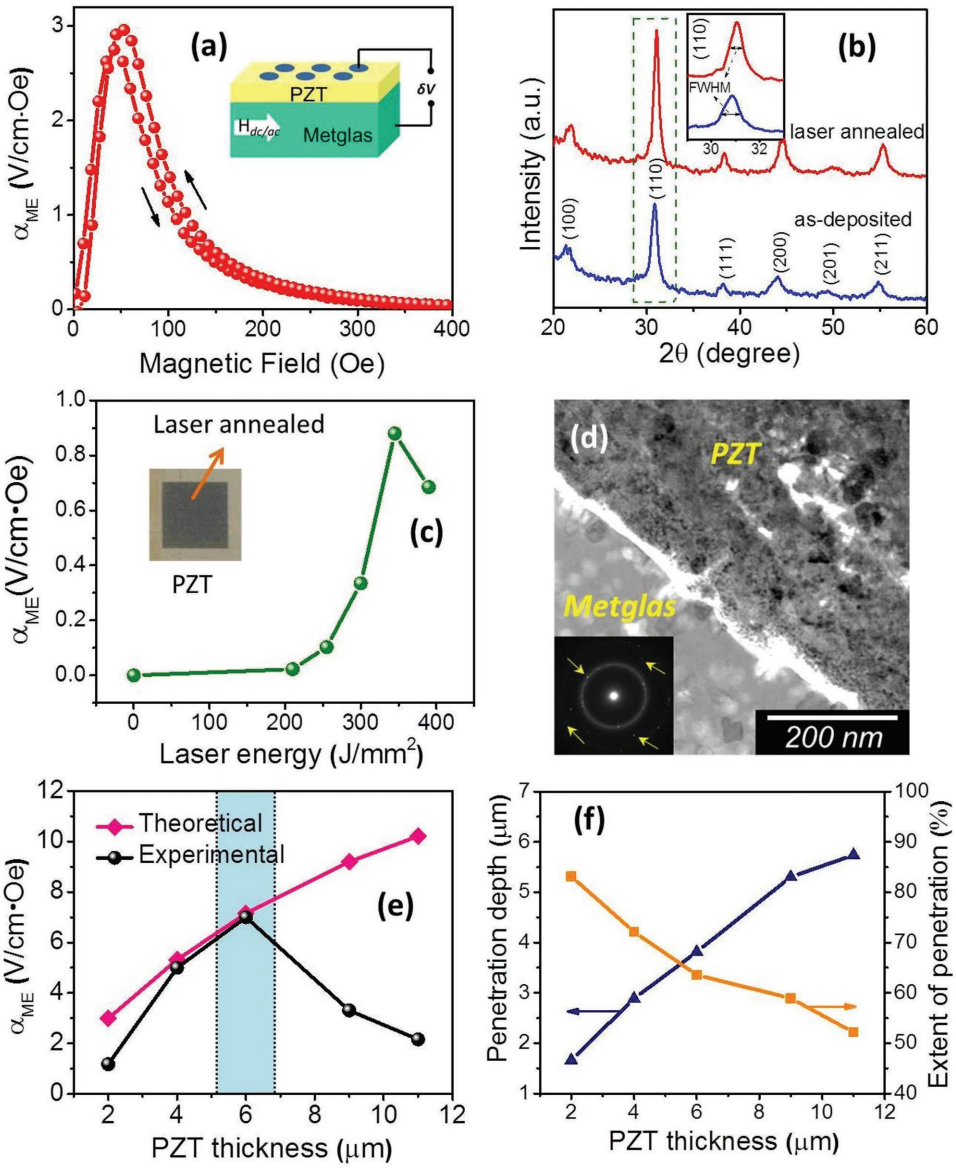

Figure 7. a) ME voltage coefficient (α_{ME}) dependence of applied magnetic bias (H_{dc}) for laser annealed PZT film (4 μm thick) on amorphous Metglas substrate (inset shows a schematic illustration of the α_{ME} measurement). b) XRD patterns of the as-deposited and laser annealed PZT film on Metglas. a,b) Reproduced with permission.[83] Copyright 2015, AIP Publishing LLC. c) Variation in values of α_{ME} as a function of laser fluence for PZT film (2 μm thick) on Metglas. Result for the as-deposited film is represented by the laser fluence of 0 J mm^{-2}. d) TEM image and selected area electron diffraction (SAED) pattern (inset) of the PZT/Metglas annealed at 390 J mm^{-2}, showing crystallization of Metglas due to laser induced heat. c,d) Reproduced with permission.[84] Copyright 2016, The American Ceramic Society. e) Comparison between theoretical and experimental α_{ME} values for different thicknesses of laser annealed PZT film on Metglas. f) Variation of the laser penetration depth and extent of penetration as a function of the PZT film thickness. Reproduced with permission.[20] Copyright 2017, Wiley-VCH.

of spin-coating + two-step photoirradiation followed by spin coating + direct laser irradiation was adopted to grow a 150 nm thick film layer-by-layer. In this case, no cracks were observed in the film, as seen in Figure 8c. The corresponding TEM image of the ITO film (Figure 8d) indicates that the grain size in the upper part of the film is larger compared with that near the interface of the film. It was found that the ITO layer grown by two-step photoirradiation acts as a buffer layer for preventing ablation of the film, and that direct laser irradiation induces photoreaction of the NPs leading to improved grain size. The resulting ITO film showed a very low resistivity of 5.94×10^{-4} Ω cm and a transmittance of 81% at 550 nm (Figure 8e).[126] The enhanced electrical and optical properties of the ITO film prepared using the combined two-step and direct irradiation processes were attributed to the improvements in sintering of the NPs and microstructure of the film.

Lee et al.[23] investigated the effect of laser irradiation on the conductivity and transparency of undoped ZnO thin films. The films spin-coated on a quartz substrate, using a ZnO NP precursor

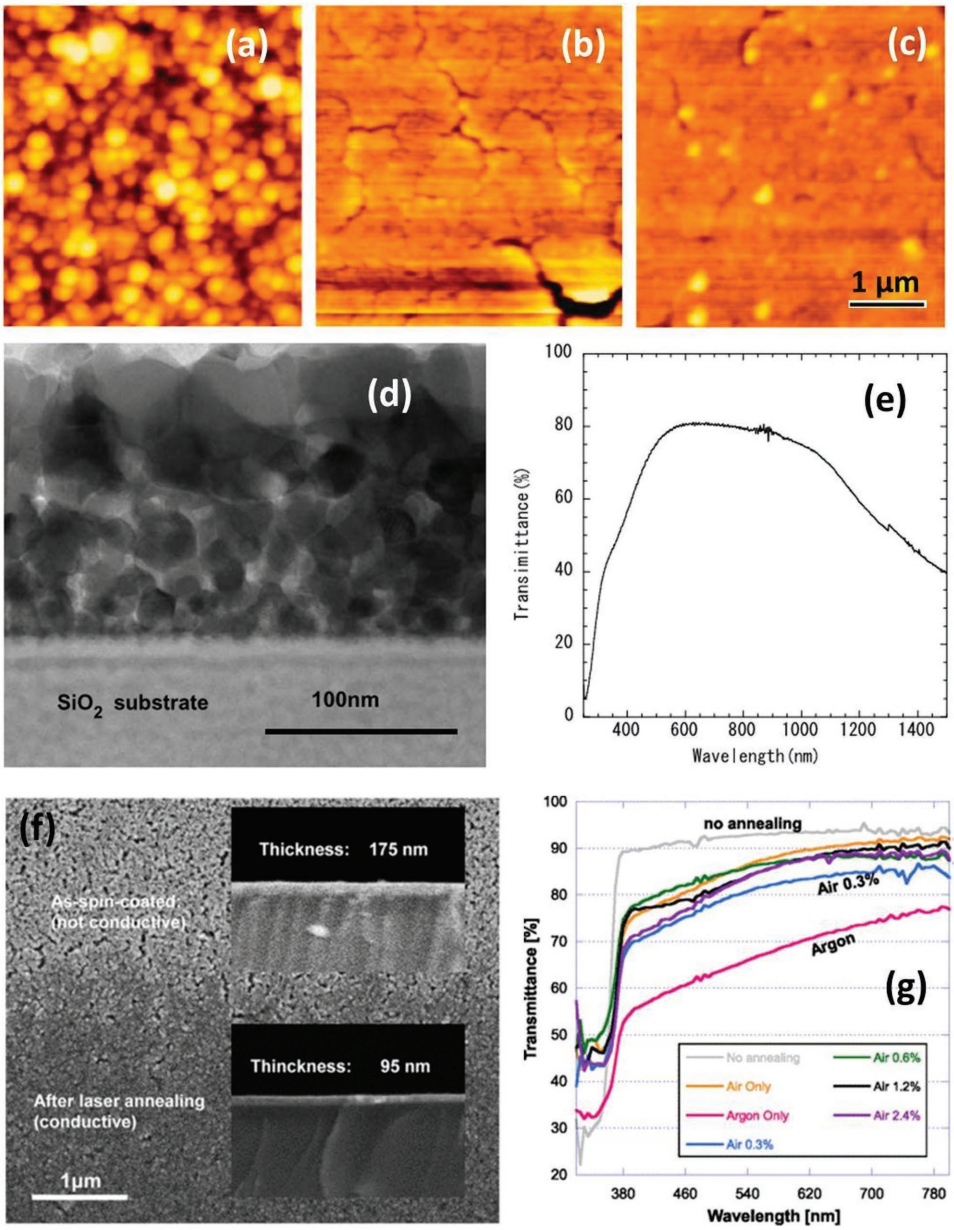

Figure 8. a,b) AFM images of ITO film surfaces after conventional annealing and two-step irradiation, respectively. c–e) AFM image of the surface, cross-sectional TEM image, and transmittance of the ITO film prepared using a combination of two-step and direct irradiation. A good control over the microstructure of the ITO film was achieved through the combination process. a–e) Reproduced with permission.[126] Copyright 2010, Springer-Verlag. f) SEM image at the boundary of as-deposited and laser annealed surface regions of ZnO. Changes in surface morphology and thickness (inset) of the ZnO film were observed after laser annealing. g) Optical transmittance of ZnO thin films annealed in various background gas compositions. f,g) Reproduced with permission.[23] Copyright 2012, Springer-Verlag.

solution, were annealed by employing a UV laser (neodymium-doped yttrium orthovanadate ($Nd:YVO_4$), 355 nm, 32.6–98.9 kW cm^{-2}, 10 mm s^{-1}, 12 ps, 80 MHz). Densification of the film after laser annealing was evidenced from the changes in its surface morphology (fused grains) and cross-sectional features (reduced thickness) (Figure 8f). A significant decrease in roughness (17–1.7 nm) was also caused by the laser treatment of the film. An optimum laser power window (60–80 kW cm^{-2}) was identified with respect to the film conductivity, and annealing with excessively high or low power resulting in high resistivity. Furthermore, combination of 50 mL min^{-1} air and 8000 mL min^{-1} Ar gas flow was shown to yield a highly conductive (sheet resistance of 5 kΩ per square and resistivity of 4.75×10^{-2} Ω cm) thin film while maintaining high transparency (84–88% in the 500–700 nm range) (Figure 8g).[23] Laser annealing of the ZnO film under ambient conditions resulted in a similar transmittance but higher sheet resistance and film resistivity of 30 kΩ per square and 2.85×10^{-1} Ω cm, respectively. The high thermal stimulation during laser irradiation and photon energy (≈3.5 eV for λ = 355 nm) greater than the bandgap of ZnO (≈3.3 eV) was

postulated to promote the dissociation of Zn—O bonds and result in the formation of oxygen vacancies. The ZnO film conductivity will be higher after annealing in an Ar environment, due to the formation of more oxygen vacancies, compared to ambient conditions where oxidation of ZnO also occurs.

3.4. Gas Sensors

Noble metal (Au, Ag, or Pt) additives are popular as activators or sensitizers to improve/tune the gas selectivity and sensitivity and to lower the operating temperature of MOs.[127,128] Two types of noble-metal–MO hybrid nanostructures, namely, surface decorated and encapsulated (core–shell), are currently being developed. Recently, Zhang et al.[129] reported the achievement of both surface decoration and encapsulation at the same time in Au–ZnO hybrid nanostructures using laser irradiation. As depicted in **Figure 9**a, initially, a Au colloidal solution was obtained by laser ablation (80 mJ per pulse) of an Au plate in an aqueous solution of 1×10^{-3} M NaOH. Next, the precursor of the colloidal solution containing Au and ZnO NPs was synthesized by laser ablation (100 mJ per pulse) of a Zn plate immersed in the as-prepared Au colloidal solution. Subsequently, the mixed Au and ZnO colloidal solution, under continuous stirring, was further irradiated by an unfocused laser (40 mJ per pulse). The microscopy images in Figure 9b,c clearly indicate that ZnO was decorated with a few large Au NPs on its surface and encapsulated with many small Au NPs. A physical heating–melting–evaporation mechanism was considered to be responsible for the formation of the Au–ZnO hybrid nanostructures.[9]

For comparison, pure ZnO NPs were prepared by focused laser ablation of a Zn plate in NaOH through irradiation of the as-prepared Zn colloidal solution with an unfocused laser beam under the same conditions. After washing with deionized water, the Au–ZnO and ZnO powders were furnace annealed at 400 °C for 2 h. The gas sensors were fabricated by dispersing the Au–ZnO or ZnO powders in ethanol, or by directly coating the powders on the surface of ceramic tubes. The response properties of both the gas sensors were highly dependent on the operating temperature reaching optimum at different points (Figure 9d). The sensing response of Au–ZnO was higher than the sensing response of ZnO over a broad temperature range (280–340 °C) and at higher concentrations of ethanol (Figure 9e). The responses of both sensors toward 100 ppm of different target gases (e.g., ethanol, acetone, and methanol) at their respective optimum operating temperatures of 360 °C (ZnO) and 320 °C (Au–ZnO) were also measured. The Au–ZnO-based sensor exhibited enhanced responses compared with the pure-ZnO-based sensor for all gases. The greater gas-sensing performance of Au–ZnO was attributed to the catalytic effects (chemical sensitization) of the surface-decorated Au particles and the formation of depletion layers (electronic sensitization) induced by the encapsulated Au particles.

Hou et al.[130] investigated the effect of laser irradiation on the performance of gas sensors made using a sol–gel-synthesized Al-doped ZnO (AZO) thin film on a glass substrate. Laser irradiation (Nd:YVO_4, 532 nm, 8 ns, 5 kHz) of the film was conducted with a fluence of 1.06–3.58 J cm^{-2}. Although the crystallinity and grain size of the film increased up to a fluence

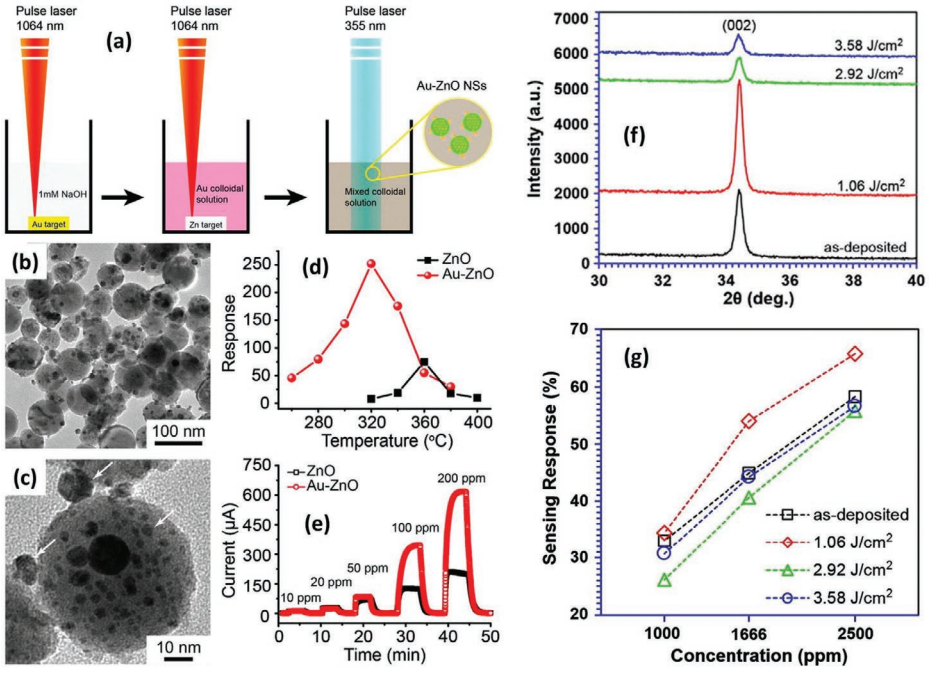

Figure 9. a) Scheme of the production of Au–ZnO NPs by laser ablation in liquid. b,c) TEM images of Au–ZnO particles produced by laser irradiation for 40 min. d) Sensing response versus operating temperature of pure-ZnO-based and Au–ZnO-based sensors to 100 ppm of ethanol. e) Dynamic ethanol response–recovery transients of the pure ZnO and Au–ZnO at 360 and 320 °C. a–e) Reproduced with permission.[129] Copyright 2016, The Royal Society of Chemistry. f) XRD patterns of as-deposited and laser irradiated Al-doped ZnO films. g) Variation of sensing response of as-deposited and laser irradiated Al–ZnO based sensors as a function of H_2 concentration. f,g) Reproduced with permission.[130] Copyright 2014, Elsevier B.V.

of 1.06 J cm^{-2}, further increasing the laser fluence resulted in decreased values (Figure 9f). The same trend was observed in the gas (H_2)-sensing response of the AZO samples (Figure 9g), indicating its strong dependency on crystallinity/grain size of the film. AZO film irradiated with fluence of 1.06 J cm^{-2} showed the highest crystallinity, grain size, and gas-sensing performance. It has been observed that crystallinity and grain size competitively influence the gas-sensor response.[131,132] A superior sensor response can be expected from materials with smaller grains, as they consist of a larger number of grain boundaries, which induce a barrier for the electron flow, thereby amplifying the resistance during the adsorption and desorption process of gaseous species. Materials with higher crystallinity and a better degree of structural perfection are likely to contain a lower density of charge carriers, such as electrons, leading to a more pronounced modulation of resistance. Laser-assisted enhancement of the crystallinity can dominate over the effect of grain growth, thereby improving the sensor response of the Al–ZnO film.

3.5. Photocatalysis

Semiconducting MOs are widely employed for the photocatalytic decomposition of various contaminants in our living environment. A variety of MOs (e.g., TiO_2, WO_3, NiO) in the pure and mixed forms have been utilized in the heterogeneous photocatalytic removal of air/water pollutants.[21,133,134] Generation of electron and hole pairs (e^-–h^+) and the separation and transfer of these charge carriers to catalytically active sites on the surface are critical steps for any photocatalytic reaction. The photocatalytic efficiency is dictated by the light-absorption capacity, which determines the number of photogenerated charge carriers and their separation. Electron–hole recombination is a competing process, decreasing the carrier mobility and preventing carriers from reaching the surface. Different methods have been proposed to enhance the charge-carrier separation, including p–n-junction formation, defect mediation, and metal-ion grafting.[21,133,135]

Recently, Molaei et al.[21] reported the enhancement of photocatalytic efficiency in single-crystalline NiO through the formation of p–n junctions induced by laser irradiation. An epitaxial NiO(111) film was grown on a Si(001) substrate buffered with cubic yttria-stabilized zirconia (c-YSZ(001)) using PLD and annealed using a KrF excimer laser (0.35 J cm^{-2}, 5 pulses, 25 ns). **Figure 10**a shows the cross-sectional microstructure of the laser irradiated NiO(111)/c-YSZ(001)/Si(001) heterostructure with the annealed layer thickness of 100 nm. The epitaxial relationship of the heterostructure was ascertained from the corresponding selected area electron diffraction

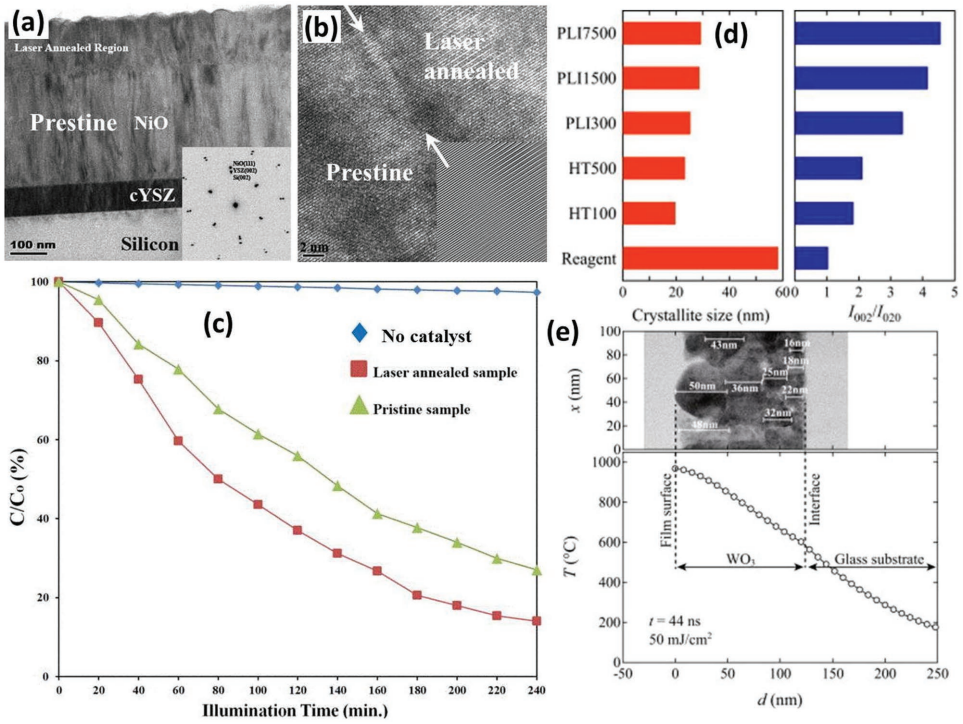

Figure 10. a) Cross-sectional TEM image and the SAED pattern taken from the laser annealed NiO(111) film. The SAED pattern (inset) belongs to Si[110], c-YSZ[110], and NiO[$\bar{4}$13] zones. b) Interface between the pristine and the laser-treated regions. c) Comparison of the photocatalytic decomposition of 4-chlorophenol under UV light by the NiO samples, reported as the ratio of the dye concentration and the initial concentration (C/C_0). a–c) Reproduced with permission.[21] Copyright 2013, AIP Publishing LLC. d) Calculated crystallite size and XRD peak intensity ratio (I_{002}/I_{020}) for the WO_3 reagent powder and thin films obtained by heat treatment at 100 and 500 °C (HT100 and HT500) and pulsed laser (PL) treatment with 300, 500, 7500 pulses (PLI300, PLI1500, and PLI7500). e) The relationship between the crystalline structure of the WO_3 thin film PLI7500, shown by the TEM image, and the depth dependence of temperature variation after the incident pulse. f) The photocatalytic degradation of methylene blue, under visible light, for the HT and PL WO_3 samples, after Cu(II)-grafting. The photolysis of methylene blue is also plotted as a blank measurement. The inset shows the EDS spectrum for the Cu(II)-grafted laser annealed WO_3. d–f) Reproduced with permission.[134] Copyright 2011, Elsevier B.V.

(SAED) pattern (inset of Figure 10a). An atomically sharp and crystallographically continuous interface was observed between the laser annealed and pristine regions (Figure 10b). Such a continuous and defect-free interface is desired for minimizing the charge-carrier scattering and for suppressing their recombination. The Hall coefficient (R_h) measured from the pristine (R_h = + 40633.33 Ω cm G^{-1}) and annealed (R_h = −29051.48 Ω cm G^{-1}) samples revealed a change in the electrical conductivity of NiO from p-type to n-type behavior. The above results confirm the creation of an n-type NiO layer on top of the as-deposited p-type NiO layer and the formation of an n-NiO/p-NiO heterojunction by laser treatment. Changes in the XRD peak position, intensity and lattice constant of NiO(111) after annealing indicated the formation of lattice defects in NiO due to laser interaction. X-ray photoelectron spectroscopy measurements indicated the laser-induced generation of Ni^0 species, which is responsible for the change in electrical conductivity. The results of photocatalytic degradation of 4-chlorophenol without any catalyst and with pristine and laser annealed NiO catalysts under UV illumination are presented in Figure 10c. The enhanced photocatalytic efficiency of the laser annealed NiO film was attributed mainly to the improved charge-carrier separation by the formation of a p–n junction. Similar experiments on the TiO_2(001)/t-YSZ(001)/Si(001) heterostructure resulted in a significant enhancement in the photocatalytic activity of the anatase film after laser annealing,[133] explained on the basis of increased oxygen-vacancy concentration, which introduces a donor energy level below the conduction band of the TiO_2 and traps the photogenerated electrons. Consequently, charge-carrier separation is enhanced, and the positive holes can reach the surface to participate in the chemical reactions.

Nakajima et al. investigated the photocatalytic performance of Cu(II)-grafted WO_3 thin films to decompose methylene blue (MB).[134] An NP dispersion of WO_3 powder was spin-coated onto glass substrates, and the films were annealed separately by furnace heating (100 or 500 °C, 60 min) and excimer laser irradiation (KrF laser, 50 mJ cm^{-2}, 300–7500 pulses, 26 ns). Laser annealing induced greater surface crystallinity and anomalous crystallite growth compared to conventional heating (Figure 10d,e)). The annealed WO_3 film surface was impregnated with an aqueous solution of $CuCl_2 \cdot 2H_2O$ for Cu(II) grafting, which was detected by energy-dispersive X-ray analysis (inset of Figure 10f). The photocatalytic decomposition of MB under visible light for the samples after Cu(II) grafting showed that the degradation rate for laser annealed WO_3 films was much larger the degradation rate of the furnace annealed sample (Figure 10f). The greater surface crystallinity and anomalous crystallite growth of laser annealed WO_3 thin films were proposed to stimulate the photogenerated electron/hole transfer at the film surface, resulting in the enhancement of the photocatalytic activity.

3.6. Field-Effect Transistors

Transparent and mechanically flexible MO semiconductors with good carrier mobility are poised to replace other established materials (Si and organic semiconductors) in next-generation field-effect transistors (FETs).[136] Both simple (e.g., SnO_2, ZnO, In_2O_3, and Ga_2O_3) and multicomponent (e.g., Zn- and/or Ga-doped In_2O_3) MOs have been studied for use as the active channel layer in thin-film transistors (TFTs). Recently, MO NWs have received broad attention for application in FETs.[137] The controllable diameter of NWs (down to <10 nm) together with smaller channel size and higher carrier mobility will lead to high device performance.[138] Traditionally, thermal annealing (>300 °C) has been utilized to improve electrical stability and enhance the channel mobility of the active layer in TFTs. However, such a high-temperature annealing is unsuitable for flexible devices employing plastic substrates and may lead to unwanted side effects during device fabrication. Laser irradiation has been suggested as an alternative annealing technique where desired regions can be selectively treated, and the laser-induced heat can be controlled very well.[139,140] Controlling the threshold voltages of NWs is of practical importance to any integrated circuits. Laser annealing has been employed successfully to shift the threshold voltages of NW FETs to make them operate in both depletion and enhancement modes.[24,141–143]

Maeng et al.[141] investigated the effect of excimer laser annealing on ZnO NWs and the respective FETs (**Figure 11**a–e). The ZnO NWs grown by a vapor–liquid–solid method on a sapphire substrate were laser irradiated (KrF, 248 nm, 50–300 mJ cm^{-2}, 25 ns) in an N_2 (97%)/H_2 (3%) gaseous atmosphere. At 50 mJ cm^{-2}, the vertically grown ZnO NWs began to melt with their tips changing into a spherical shape (Figure 11b). As the laser fluence increased, more melting occurred, and the NWs broke into pieces (Figure 11c). Energy-dispersive X-ray analysis results revealed that there is an excess of Zn in the spherical tip region, relative to the other portion of the ZnO NWs, suggesting an increase in oxygen vacancies by laser annealing in the reducing atmosphere. Furthermore, photoluminescence measurements indicated a decrease in the UV emission intensity of the laser annealed ZnO NWs above 50 mJ cm^{-2}, due to the decrease in crystallinity of the NWs. To fabricate ZnO NW FET devices, as-grown individual NWs were dropped onto a thermally grown oxide layer on silicon. Laser annealing was conducted after the patterning of the Ti and Au source and drain electrodes on the edges of a ZnO NW. While most of the NW FETs survived at 50 mJ cm^{-2}, very few survived above that laser fluence (inset of Figure 11c). After laser annealing, the FETs were observed to operate in an n-channel depletion mode, with a nonzero current at the zero-gate bias and a negative threshold voltage (V_{th}) (Figure 11d,e). The shifting of V_{th} to the negative-gate-bias direction was associated with a relative increase in oxygen vacancies, which act as n-type dopants.

Lee et al.[24] studied the effects of femtosecond laser annealing on fully transparent inverters consisting of two In_2O_3 NW FETs, where the laser pulses were focused and scanned only along the source/drain contact regions (Figure 11f,g) rather than on the NWs themselves to avoid damaging or sputtering the NWs away. A single-crystal In_2O_3 NW synthesized by laser ablation was employed as the active channel, and ITO was used for gate, source, and drain electrodes. Instead of a high-energy excimer laser, a Ti:sapphire laser operating at 800 nm with energy lower than the bandgap of In_2O_3 was used for annealing (0.14–0.43 J cm^{-2}, 50 fs, 1 kHz). Laser irradiation appeared to have induced a shift of V_{th} to the positive direction, which resulted in a smaller saturation current at the same gate voltage (Figure 11h). Moreover, the shift in V_{th} increased

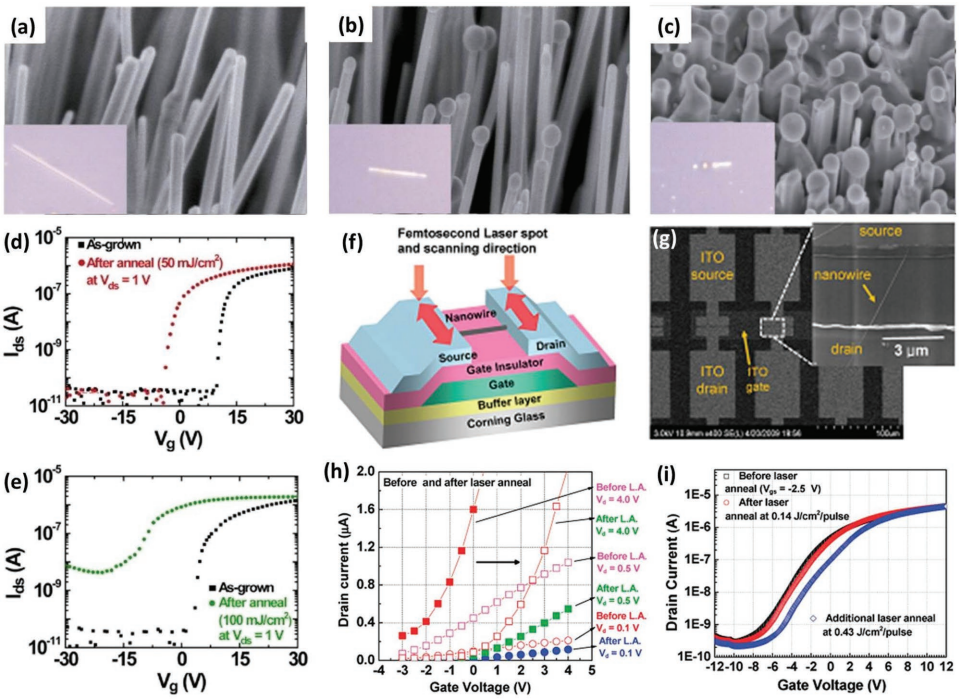

Figure 11. a–c) SEM images of as-grown and laser annealed (at fluences of 50 and 100 mJ cm^{-2}) ZnO NWs, respectively. d,e) Drain–source current versus gate voltage (I_{ds}–V_g) curves of the ZnO NW transistors measured at drain-to-source voltage (V_{ds}) of 1 V for samples annealed at 50 and 100 mJ cm^{-2}, respectively. a–e) Reproduced with permission.[141] Copyright 2009, IOP Publishing Ltd. f) Cross-sectional schematic and g) top-view SEM images of an In_2O_3 NW-based transistor. ITO was used for gate, source, and drain. h) Threshold-voltage (V_{th}) shift of the NW transistor, before and after laser annealing, at V_{ds} = 0.1, 0.5, and 4.0 V. i) The log-scale drain–source current versus gate voltage (I_{ds}–V_{gs}) characteristic of an In_2O_3 NW transistor at V_{ds} = 0.5 V with different laser-fluence conditions. f–i) Reproduced with permission.[24] Copyright 2011, American Chemical Society.

significantly by sequentially applying two different values of laser energy to the same NW FET (Figure 11i). The above results suggest that laser annealing could be a better method to tune the V_{th} values of NW FETs.

3.7. Solar Cells

Dye-sensitized solar cells (DSSCs) utilize TiO_2 as a photoelectrode material synthesized in the form of a nanocrystalline mesoporous structure that provides a high surface area for dye adsorption. Commonly, thermal treatment at ≈500 °C is required to promote sintering, while simultaneously removing the solvents and organic binders from the TiO_2 precursor layer coated on a TCO/glass substrate.[12] Recently, laser annealing of TiO_2 photoelectrodes for DSSCs has been proposed as an alternative to the conventional thermal annealing to reduce the thermal damage to the substrate and improve the compatibility with other layers. In addition, the local nature of laser radiation makes it compatible for integration with flexible substrates such as plastics and metal foils.

Mincuzzi et al.[144] investigated laser irradiation (Nd-YVO_4, 355 nm, 30 kHz, 10 ns) of TiO_2 films deposited via blade-coating on fluorine-doped SnO_2 (FTO)/glass substrates. Efficient sintering of TiO_2 films was achieved by optimizing the laser fluence (ϕ) through modulation of the beam radius (w) and defocusing distance (z) (**Figure 12**a,b). At an optimum laser fluence ($\phi \approx 500$ J cm^{-2}), good quality films were obtained. However, the film was found to deteriorate on further increasing the laser fluence due to thermal stress-induced macroscopic cracks (Figure 12c,d). The DSSCs fabricated using laser-sintered TiO_2 film displayed an efficiency of 5.2%. Due to improved electromechanical bonding between TiO_2 NPs, a longer electron diffusion time (or lifetime) reflecting a lower recombination probability for the injected electron was attained.[12] Mincuzzi et al.[145] have demonstrated that TiO_2 films with even larger area could be uniformly sintered by adjusting the laser fluence and defocusing distance. A 4 cm × 4 cm TiO_2 surface was uniformly processed by controlling the offset between successive scan lines (Nd:YAG, 355 nm, 30 kHz, 60 ns, 1–7 kW) resulting in high efficiency of 7.1% (Figure 12e).

Spann et al.[146] performed pulsed laser sintering of TiO_2 NPs to enhance charge transfer between CdS and TiO_2 heterojunctions formed through the direct adsorption of CdS nanocrystals on the surface of TiO_2. The TiO_2 films (3.5 μm thick) were deposited on a glass substrate using the doctor-blade technique. The laser irradiation of films was conducted using a KrF excimer laser (248 nm, 50–200 mJ cm^{-2}, 25 ns, 10 Hz). After the laser irradiation, CdS was adsorbed on the TiO_2 films through the successive ionic-layer adsorption and chemical reaction. The laser sintering was found to induce a mesoporous to macroporous structural transformation accompanying an anatase to rutile phase transformation of TiO_2. The morphological transformation resulted in volumetrically larger pore networks, leading to an increased density of the electron-accepting states. The phase transformation increased the fraction of rutile

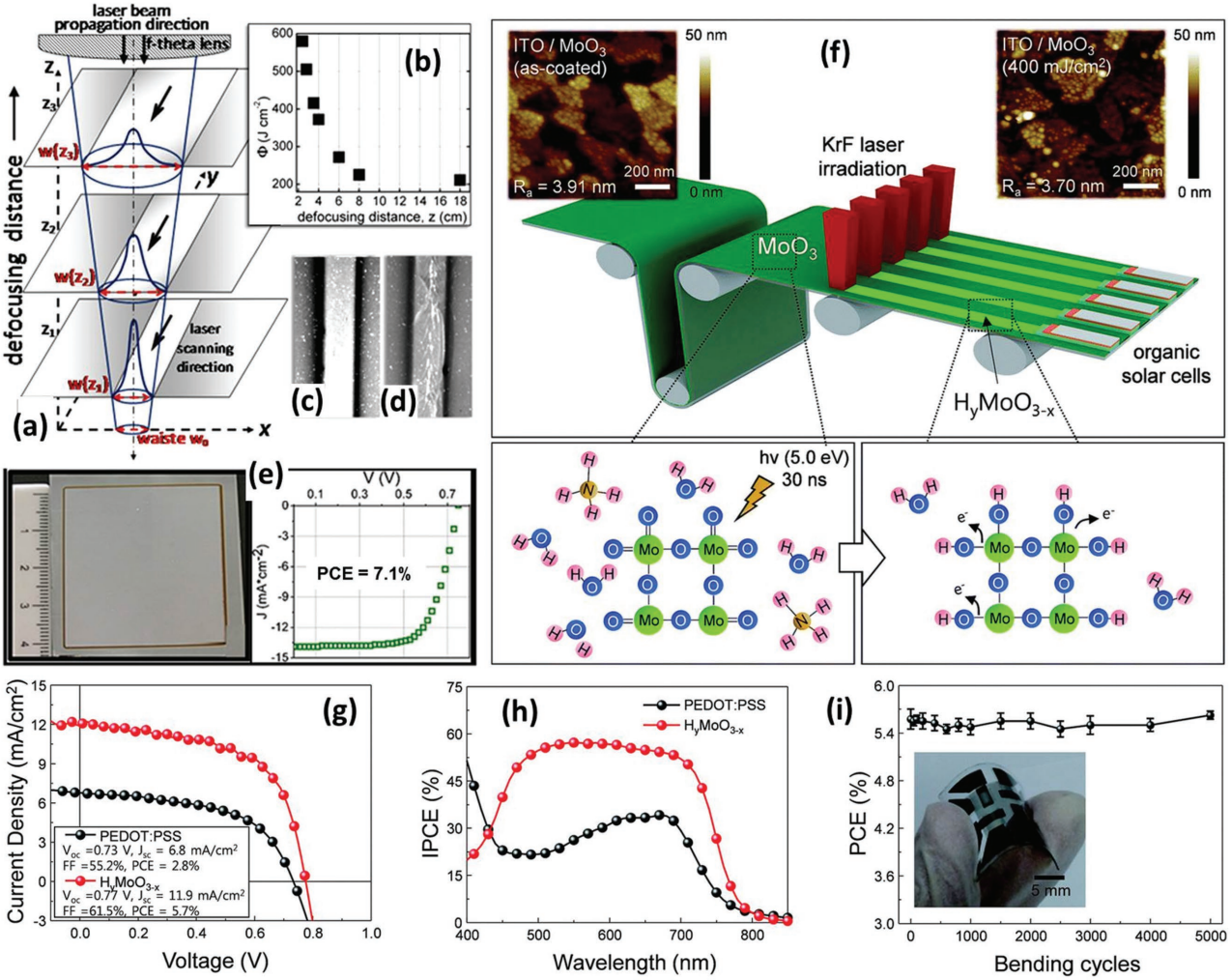

Figure 12. a) Schematics of the laser-scanning procedure for sintering of TiO_2 film. The characteristics of beam-intensity profile are shown for three different defocusing distances $z_1 < z_2 < z_3$. The beam radius (w) increases while the power density decreases with z ($z = 0$ corresponds to the focal plane of the beam). b) Integrated laser fluence Φ as function of z. c,d) Optical microscopy images of the heat-affected zones after one laser pass for optimum Φ (= 500 J cm^{-2}) and smaller z, respectively. a–d) Reproduced with permission.[145] Copyright 2009, American Institute of Physics. e) The TiO_2 surface raster-scanned by a laser over a large area (4 cm × 4 cm) and current-density–voltage (J–V) characteristics of the corresponding DSSC showing a cell efficiency of 7.1%. Reproduced with permission.[146] Copyright 2012, Wiley-VCH. f) Schematic illustration of the laser irradiation of the hydrogenated MoO_3 hole-transport layer for flexible organic solar cells. Inset: AFM images of as-coated MoO_3 and laser irradiated MoO_3. g) J–V curves and h) incident photon-to-current efficiency (IPCE) spectra of flexible top-illuminated OSCs. i) Change in photoconversion efficiency (PCE) by bending cycles at a radius of 0.48 cm. f–i) Reproduced with permission.[25] Copyright 2016, The Royal Society of Chemistry.

phase compared to anatase phase in the TiO_2 film, producing thermodynamically favorable conditions for increasing the electronic potential between donor and acceptor states. Both these transformations enhanced the charge transfer between CdS and TiO_2.

In organic solar cells (OSCs), an anode interfacial layer that functions as a hole-transport layer (HTL) is employed to obtain hole injection in the active layers of the organic semiconductors.[147,148] Transition-metal oxides (TMOs) such as MoO_3, V_2O_5, NiO, and WO_3 have been demonstrated successfully as replacements for the widely used HTL material such as poly(3,4-ethylenedioxythiophene):polystyrenesulfonate (PEDOT:PSS), which is hygroscopic and acidic with an associated reduction in device stability. Among TMOs, molybdenum oxide (MoO_3) has emerged as a promising candidate due to high transmittance, better air stability, and high work function (WF).[149,150] Dong et al.[25] suggested that by adopting a combination of solution processing and laser direct writing roll-to-roll fabrication along with the simultaneous patterning of the HTL material could be enabled (Figure 12f). They considered laser irradiation an alternative approach to create oxygen vacancies in MoO_3 for improving the electrical conductivity necessary for high HTL efficiency. The precursor solution $(NH_4)_6Mo_7O_{24}\cdot 4H_2O$ was spin-coated on ITO/glass substrate, and the resultant MoO_3 containing layer was irradiated using a KrF excimer laser (120–600 mJ cm^{-2}, 2 Hz, 30 ns). Optical transmittance of the MoO_3 film was found to be independent of laser energy. Negligible changes were observed in the roughness of the film until 400 mJ cm^{-2}, after which further increase in the energy led to deterioration of the

ITO electrode (inset of Figure 12f). The heat generated due to the photon absorption in the MoO_3 precursor layer was found to dissociate hydrogen atoms from the ammonium molecules, resulting in the formation of hydrogenated molybdenum oxide (H_yMoO_{3-x}). By controlling the laser energy, the stoichiometry of the H_yMoO_{3-x} layer was manipulated to obtain a high WF (5.6 eV) and good electrical conductivity (9.9 μS cm^{-1}). The device with H_yMoO_{3-x}, due to its higher short-circuit current (J_{sc}), exhibited better photoconversion efficiency (PCE) than the device with PEDOT:PSS (Figure 12g). The higher efficiency of the H_yMoO_{3-x}-based device was attributed to the larger amount of photocurrent generated under the visible-spectrum regime (Figure 12h) facilitated by the efficient light absorption in the H_yMoO_{3-x} layer. The OSCs with H_yMoO_{3-x} displayed a good mechanical flexibility and stable efficiency over 5000 bending cycles (Figure 12i).

In the last few years, there is a growing interest in the development of flexible perovskite solar cells (PSCs), which usually consist of an organometal halide photoactive layer combined with various functional layers that are sequentially deposited on a flexible plastic substrate.[151] In PSCs, mesoporous TiO_2 is often utilized as the electron-transport layer (ETL) for the selective extraction of photogenerated electrons. To address the issue of the high-temperature annealing required to obtain a high-quality TiO_2 layer with good crystallinity, alternative techniques such as UV irradiation and intense pulsed light (200–1400 nm) sintering have been employed.[152–154] Di Giacomo et al.[152] conducted UV irradiation (225 mW cm^{-2}) of a TiO_2 scaffold layer deposited on poly(ethylene terephthalate) (PET)/ITO substrates. The corresponding flexible PSC comprising a $CH_3NH_3PbI_{3-x}Cl_x$ perovskite layer together with an atomic-layer-deposited TiO_2 compact layer exhibited a PCE of 8.4%, significantly higher than devices without a compact layer or scaffold. Das et al.[153] fabricated $CH_3NH_3PbI_{3-x}Cl_x$-based flexible PSC devices incorporating sol–gel-processed and photonic-cured (200 V, 25 pulse, 7 ms) TiO_2 films. These devices exhibited PCEs as high as 15.0% and 11.2% with the TiO_2 films on ITO-coated glass and flexible PET substrates, respectively. Feleki et al.[154] performed intense pulse light curing (12.3 J cm^{-2}, 2 ms) of a mesoporous TiO_2 layer coated on both glass and poly(ethylene naphthalate) (PEN) substrates. The curing treatment has contributed to PCEs of 16.7% and 12.3% in $CH_3NH_3PbI_3$-based PSC devices fabricated on ITO/glass and ITO/PEN substrates, respectively. Recently, it was proposed that TiO_2 NRs offer higher electron mobility, superior phase stability, and improved pore-filling compared with their particle analogues, as an ETL.[155,156] A critical problem in the patterning of NRs on substrates was solved by interfacial engineering during the growth process and using laser ablation for patterning. Fakharuddin et al.[156] fabricated $CH_3NH_3PbI_{3-x}Cl_x$-based PSC modules by employing precisely laser patterned (Nd:YVO_4, 1064 nm, 4.5 J cm^{-2}) TiO_2 NRs on a laser-patterned FTO-coated glass substrate. These PSCs exhibited a PCE of ≈10.5%, which was significantly higher than reference modules made either with TiO_2 NPs (7.9%) or with just a compact TiO_2 layer in the planar architecture (5.8%). These results clearly demonstrate the viability and potential of photo-irradiation techniques for high-efficiency PSCs.

3.8. Flexible Thermistors

Negative-temperature-coefficient thermistors using Mn-spinel oxides require high processing temperatures (sintering above 1300 °C for bulk and deposition/annealing at 700–1200 °C for thin films) to produce sufficient quality.[157–161] As the device design trends toward flexible and wearable applications, there is a demand for thin-film thermistors to be integrated directly onto flexible organic substrates. However, the development of Mn-spinel-oxide-based flexible thermistors is limited by the high fabrication temperatures. To overcome this limitation, Nakajima and Tsuchiya employed the laser-induced photoreaction of NPs of a Mn-spinel oxide coated on a flexible PET substrate.[95] An NP (200–400 nm) ink of $Mn_{1.56}Co_{0.96}Ni_{0.48}O_4$ (MCN) was prepared by wet milling of polycrystalline MCN powders with metal organic salts of Mn, Co, and Ni dissolved in toluene (MCN solution). The MCN ink was spin-coated on a PET sheet with inkjet-printed Ag electrodes and was preirradiated with a KrF laser (35 mJ cm^{-2}) (**Figure 13**a). After repeating the spin-coating and preirradiation sequence twice (to increase the film thickness and reduce the porosity), the precursor films were finally laser irradiated under 35, 55, and 75 mJ cm^{-2} with 50–1000 pulses at room temperature in air. The fabricated flexible MCN (2 μm thick) thermistor is displayed in Figure 13b. As a reference, the MCN film on a PET sheet was prepared using repeated spin-coating and drying (130 °C, 30 min).

Simulations of the temperature variations of the Mn-spinel layer during laser irradiation indicated a strong dependence of heat input on the size and depth of interparticle pores in the precursor film. These pores would enable the UV laser radiation to reach deep into the film, which otherwise is not possible with fully dense precursor films due to the shallow penetration of UV wavelengths. During the initial stage of laser irradiation, the formation of very small (≈10 nm) granular particles of MCN, covering the original MCN NPs, from the chemical reaction of the MCN solution was observed. The tiny pores generated between the small granular NPs lead to strong photothermal heating under laser irradiation because of their very low thermal conductance. The enhanced photothermal heating preferentially induces melting of the small NPs, forming thin liquid layers on the large NPs and stimulating ionic diffusion from the solid particles, resulting in efficient grain growth and densification by liquid-phase sintering. The densified top part with no pores will enhance thermal transport to the layer underneath. In the lower layer, the liquid-phase sintering originating from the enhanced photothermal heating and melting-point depression of the small NPs continuously proceeds toward the substrate interface. The proposed laser-sintering mechanism (Figure 13c) was supported by the microstructural changes observed in the dried and laser irradiated MCN films (Figure 13d–g). Optimum densification and sintering by laser irradiation was observed to occur under 55 mJ cm^{-2} with 600 pulses.

The laser irradiated MCN films were coated with methylcellulose resin to protect the surface. The decrease (≈80%) in resistance of the films observed was attributed to the possible filling of the tiny pores with the resin. The best values of resistivity (ρ) and thermal constant (B) for the MCN

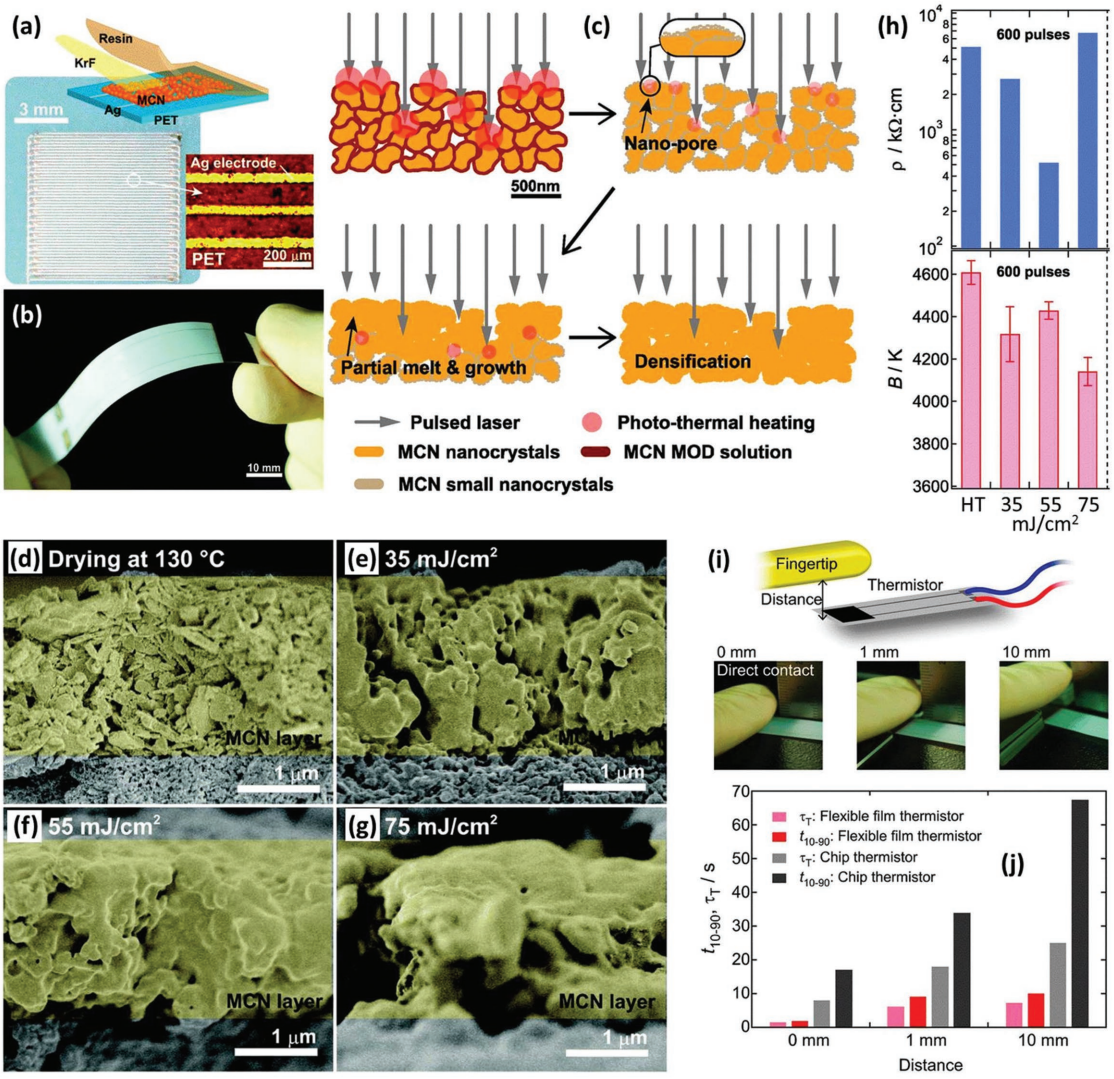

Figure 13. a) Optical microscopy image of the Ag electrode pattern on the PET. The inset shows a schematic view of the fabrication of MCN film thermistors. b) Photograph of the flexible MCN film thermistor on the PET sheet. c) Schematic illustration of the morphological changes of MCN particles during laser irradiation. d–g) SEM cross-sectional view of the sample prepared at 0–75 mJ cm^{-2} with 600 laser pulses. h) Electrical resistivity (ρ) and thermal constant (B) for the MCN films on PET substrates prepared by drying (HT) at 130 °C and laser irradiation at 35–55 mJ cm^{-2} with 600 pulses. i) Finger-approach temperature-sensing test of the thermistor, at a distance of 0, 1, and 10 mm. j) Calculated temperature increase time for commercial and laser irradiated MCN thermistors. Reproduced with permission.[95] Copyright 2015, The Royal Society of Chemistry.

thermistor were obtained at 55 mJ cm^{-2} with 600 pulses (Figure 13h). Both ρ and B of the MCN film were relatively large compared with flexible thermistors fabricated using Au, graphene, NiO, and $Ti_{1-x}Al_xN$, possibly because of the greater crystallinity of the MCN films. During the temperature cycle test, this laser annealed MCN thermistor showed almost unchanged resistance variation (ΔR) and followed the theoretical value for the B value of the film. During the bending test, the ΔR of the MCN thermistor was very stable with a bending radius of 1.0 cm, while the ΔR was slightly increased (≈2.3%) by 40 cycles with a bending radius of 3.0 cm. However, the deterioration was insignificant. The laser annealed MCN film thermistor also exhibited a rapid, sharp response of temperature sensitivity, better than a commercial ceramic chip thermistor (Figure 13i,j).

4. Other Laser-Induced Phenomena in Metal Oxides

4.1. Structural Distortion and Transformation

Local structural modification and controlled concentration of oxygen defects in MOs significantly influence their physical properties. It is possible to tune the electronic states of local sites on crystal surfaces by a high-energy ion beam or laser irradiation.[27,162] Laser irradiation has been utilized for inducing oxygen deficiency into TiO_2,[27] $CaTiO_3$,[163] and $Sm_{0.5}Ba_{0.5}MnO_3$[164] and for phase or structural transformation of α-Al_2O_3 to γ-Al_2O_3,[165] α-Bi_2O_3 to δ-Bi_2O_3,[166] tetragonal Cu_4O_3 to monoclinic CuO,[167] orthorhombic $WO_3 \cdot H_2O$ to monoclinic WO_3,[168] orthorhombic to monoclinic to cubic ZrO_2,[169] and tetragonal $SrCuO_2$ to orthorhombic $SrCuO_2$.[28]

Nakajima et al.[27] studied the effect of laser fluence on the structural transformations and electrical-transport properties of rutile TiO_2 surfaces. The oxygen-deficient TiO_2 surface layer was formed by the reduction of Ti^{4+} to Ti^{3+} under laser irradiation. The cross-sectional TEM image (**Figure 14**a) of the TiO_2 surface after ArF laser irradiation at a fluence of 140 mJ cm^{-2} revealed phase separation between the laser-induced oxygen-deficient TiO_2 layer ($TiO_{2-\delta} \approx 160$ nm) and the unaffected TiO_2 layer. The SAED pattern of the $TiO_{2-\delta}$ layer displayed streaks and some other spots near the interface along the (100) direction (Figure 14b,c). However, these streaks and spots disappeared completely in the unaffected TiO_2 layer (Figure 14d). The thickness of the $TiO_{2-\delta}$ layer was tailored through the suitable control of laser fluence and pulse duration. The laser-induced oxygen vacancies gave rise to structural distortion with stacking faults (Figure 14e) in the $TiO_{2-\delta}$ layer, which, in turn, lowered the structural symmetry from tetragonal to monoclinic or triclinic.

Terakado et al.[28] investigated the super-bandgap light-assisted structural change from layer-type (tetragonal) $SrCuO_2$ to chain-type (orthorhombic) $SrCuO_2$. The chain-type $SrCuO_2$ exhibited a higher thermal conductivity than the layer-type $SrCuO_2$, which is promising for thermal-management applications. Layer-type $SrCuO_2$ films were deposited onto a glass substrate by radio-frequency (RF) magnetron sputtering. The structural transformation from layer-type $SrCuO_2$ to chain-type $SrCuO_2$ was investigated using a Raman spectroscopy system equipped with microfocus optics and solid-state laser emitting CW light at a 532 nm wavelength, which corresponds to a photon energy of 2.3 eV and super-bandgap light for the as-sputtered film having a Tauc gap of 1.5 eV. The as-deposited $SrCuO_2$ film exhibited broad peaks ≈300, 600, and 1200 cm^{-1} (Figure 14f). The structural changes in the $SrCuO_2$ film started to occur when increasing the laser power above 3 mW. On increasing the laser power up to 6.3 mW, the layer-type $SrCuO_2$ film was transformed to chain-type $SrCuO_2$, as is evident from the appearance of a completely different Raman spectra. Figure 14g shows the approximate temperature of the films at the focal point under the laser irradiation with different powers, which was calculated based on the intensity ratios of anti-Stokes/Stokes scattering in the Raman spectra. At 500 K, a significant structural change was observed in the laser irradiated film. However, a conventionally heated film at 573 K exhibited Raman spectra similar to the Raman spectra of the as-deposited film. The rapid heating coupled with the photoexcitation effect was considered to play a major role in the layer-type to chain-type structural transformation in the $SrCuO_2$ film under super-bandgap light irradiation.

4.2. Magnetization Dynamics

Recent studies have demonstrated that laser irradiation/annealing can induce diamagnetic to ferromagnetic switching

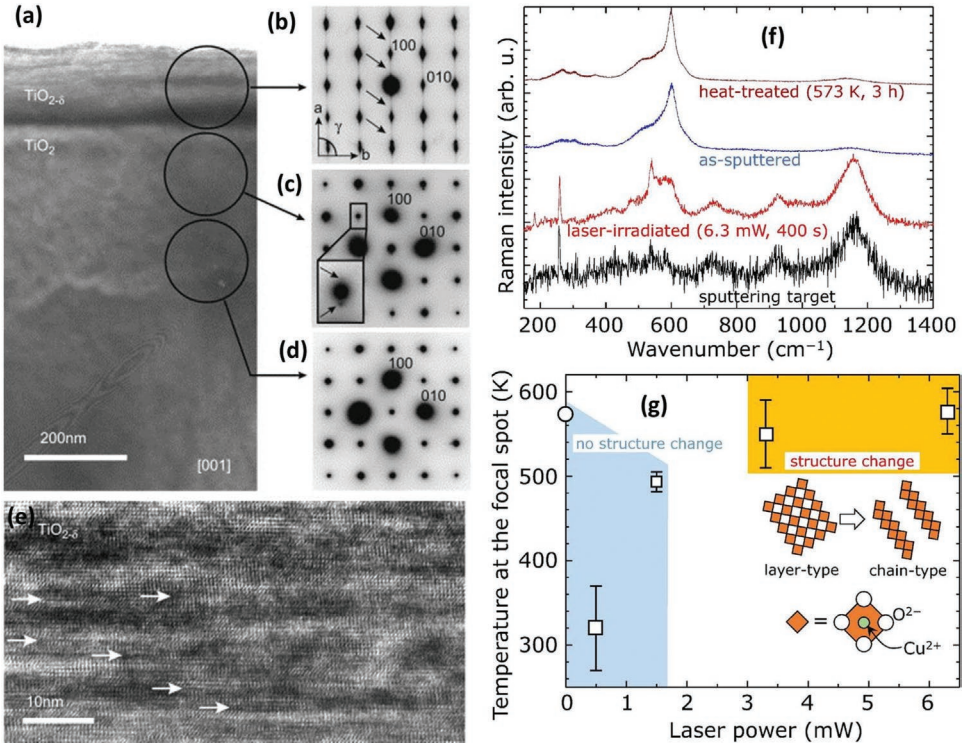

Figure 14. a) Cross-sectional TEM image obtained along the [001] zone axis for a TiO_2(100) substrate irradiated by an ArF laser at 140 mJ cm^{-2}. b–d) SAED patterns observed at the circled regions in the TEM image. e) High-resolution TEM image along the [001] zone axis of the $TiO_{2-\delta}$ layer. The white arrows indicate stacking faults in the structure. a–e) Reproduced with permission.[27] Copyright 2009, Elsevier Inc. f) Raman spectra of as-sputtered, laser irradiated and heat-treated $SrCuO_2$ film as well as the sputtering target. g) Temperatures at the focal spot estimated from intensity ratios of anti-Stokes/Stokes scattering in the Raman spectra under laser irradiation. The open circle shows the conventional heat-treatment condition. Schematic illustrations of the layer and the chain structures in the $SrCuO_2$ having the CuO_4 units are also shown in the inset. f,g) Reproduced with permission.[28] Copyright 2016, Elsevier B.V.

in semiconducting (VO_2) and insulating ($BaTiO_3$, $SrTiO_3$) MOs, without any extrinsic metal impurities.[29,30,170] In these studies, the laser energy was optimized to disrupt the orbital and electronic configuration. Rao et al.[30] reported the ferromagnetic features in a nonmagnetic $SrTiO_3$ (STO) single crystals after irradiation with a KrF (248 nm) laser. Field-dependent magnetization properties of pristine, laser irradiated, and oxygen-annealed STO single crystals, measured at 300 K, are shown in **Figure 15**a. The pristine STO exhibited diamagnetic behavior as expected, whereas a clear magnetic saturation loop with a coercive field of 200 Oe was observed in the laser irradiated (0.236 J cm^{-2}, 20 pulses) STO sample. This laser-induced ferromagnetic property was present in the STO single crystals even after 2 months, indicating a stable state. However, a sample annealed under an oxygen atmosphere exhibited a tenfold reduction in magnetic moment compared to the laser irradiated STO sample. The laser-induced oxygen vacancies were found to play a crucial role in creating a stable ferromagnetic state in the nonmagnetic oxide. The origin of the ferromagnetism in the STO sample was considered to be the result of the coupling between spin-polarized oxygen vacancies and the localized Ti 3d electrons.

Magnetic materials exhibiting an exchange-bias (EB) effect are used in memory devices, logic devices, and radio-frequency emitters. Usually, EB in an antiferromagnetic/ferromagnetic (AFM/FM) bilayer can be established by either applying a magnetic field during film deposition or cooling the sample from above the Neel temperature of the AFM material to room temperature under a constant magnetic field.[31,171,172] However, the application of a magnetic field during the FM-layer deposition cannot effect the reorientation of the interfacial net spins to a much higher degree. However, the conventional field-cooling (postannealing) procedure could cause severe interfacial diffusion and/or reaction between the layers, thereby causing the deterioration of the EB. This issue can be avoided by using the laser annealing technique to induce/enhance the EB in the AFM/FM bilayers. Zhang et al.[31] investigated the feasibility of laser annealing accompanied by fast field cooling in a $BiFeO_3$ (BFO)/Co bilayer system and the corresponding changes in its EB and exchange fields (H_E). Polycrystalline BFO/Co bilayers were deposited onto LNO/Si substrates using PLD and magnetron sputtering. To obtain the EB effect, a magnetic field of 200 Oe was applied during the deposition of the Co layer. After deposition of both layers, the samples were irradiated using a femtosecond pulsed laser (800 nm, 8.5–40 mJ cm^{-2}, 60 fs, 1000 Hz). The sample was irradiated on several 600 µm spots each for 10 s, followed by cooling for 5 min under a magnetic field of 1 kOe. Figure 15b–e represents the *M*–*H* loops of the samples, where the Co layer is deposited under a magnetic field (Figure 15b,c) and without a magnetic field (Figure 15d,e). The samples deposited under the magnetic field exhibited rectangular *M*–*H* loops with a significant EB compared to others. The calculated H_E values (≈−37 to +31 Oe) for all the samples exhibited a profound dependence on the laser fluence and cooling-field (H_F) direction. The EB could either be induced or enhanced by laser irradiation under fast field cooling up to a certain level of laser fluence due to the lower interfacial diffusion compared to conventional field cooling. Above this critical value, the interfacial deterioration and weakening of the exchange coupling of the BFO/Co bilayers was observed. The laser fluence should be optimized carefully to prevent damage at the layer interfaces.

4.3. Wettability Switching

The ability to switch between hydrophobicity and hydrophilicity of materials can be utilized in self-cleaning, self-assembly, drug delivery, and lab-on-a-chip devices. The surface wettability of materials can be tailored by modifying the surface chemistry

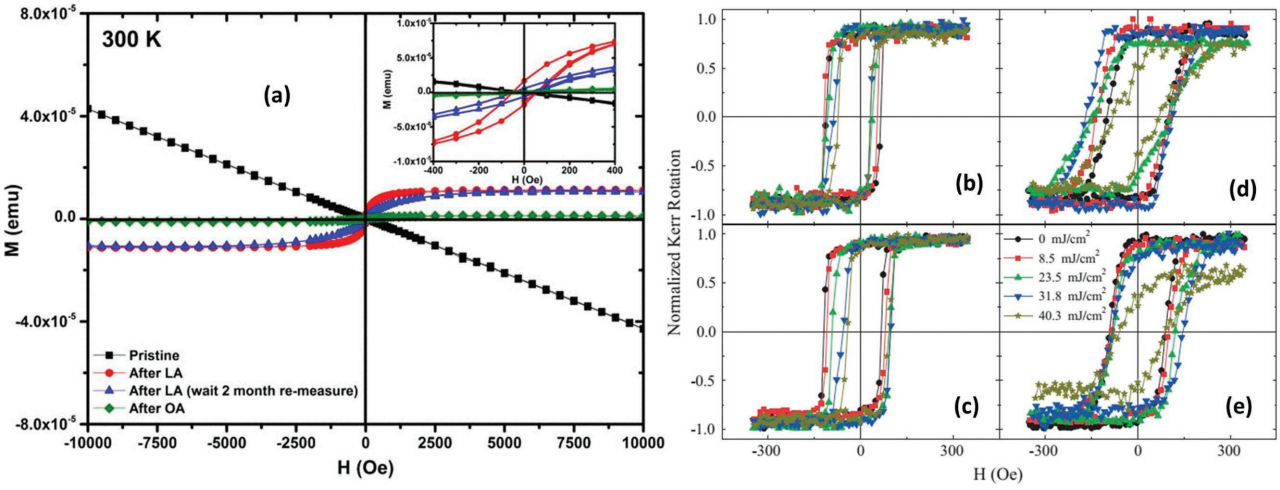

Figure 15. a) In-plane isothermal magnetization data, measured at 300 K, from samples of $SrTiO_3$ single crystals under different conditions: pristine, laser annealed (LA), aged for two-months after laser annealing, and oxygen annealed (OA). Reproduced with permission.[30] Copyright 2014, AIP Publishing LLC. b–e) In-plane *M*–*H* loops of BFO/Co bilayers measured after laser irradiation under H_{FC} = +1000 Oe (b,d) and under H_{FC} = −1000 Oe (c,e). Positive/negative means the direction of H_{FC} is parallel/antiparallel to the positive directions of the magnetic field during the deposition of the Co layer and the *M*–*H* measurement. As the Co layer was deposited with (without) applied magnetic field, exchange bias could (not) be observed in the BFO/Co samples corresponding to (b) and (c) ((d) and (e)). b–e) Reproduced with permission.[31] Copyright 2016, Elsevier B.V.

and morphology using an external stimulation. Wang et al.[32] demonstrated that laser irradiation is an effective way to rapidly modify the surface wettability of ZnO NWs. Vertically aligned ZnO NWs (3.6 µm in length and 150 nm in diameter) synthesized by hydrothermal growth were irradiated using a KrF excimer laser (248 nm, 230 mJ cm^{-2}, 25 ns) at room temperature in an ambient atmosphere to reduce oxygen loss. The laser fluence of 230 mJ cm^{-2} was optimized so that the temperature at the irradiated region of the ZnO NWs could rise above the melting point of ZnO (2248 K) and below the level of the larger diffusion of ejected species. The SEM analysis revealed that the tips of the as-synthesized ZnO NWs were transformed into hollow nanospheres under pulsed laser irradiation (**Figure 16**a,b). This phenomenon was attributed to the heat generation (≈2400 K) under laser irradiation, melting the ZnO NWs into a cluster cloud of Zn, O, Zn^{2+}, and O^{2-}. After irradiation, the ambient air around the sample caused a sharp temperature gradient from the surface to the center of the ejected

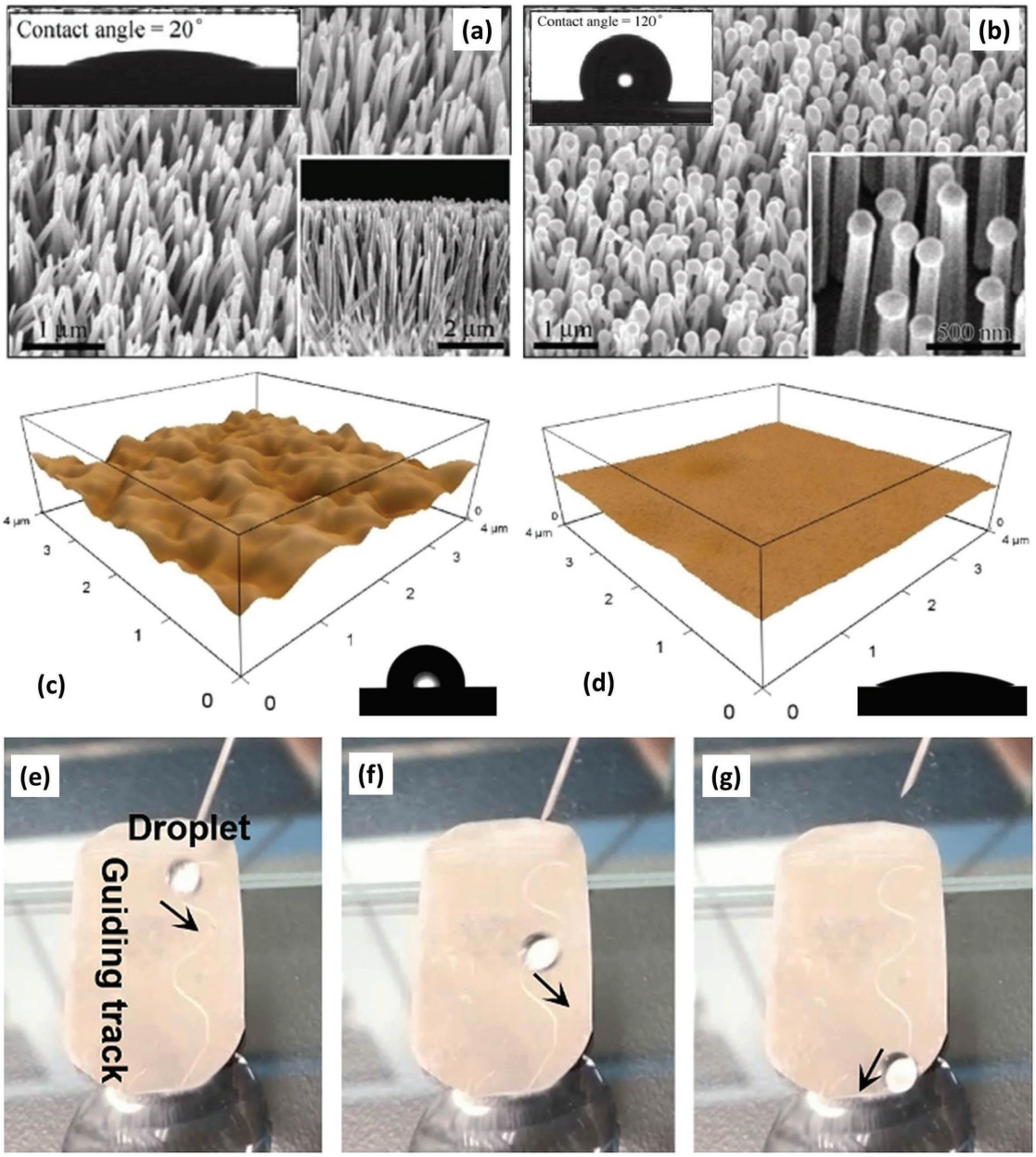

Figure 16. Morphology changes of the as-grown ZnO NW arrays a) before and b) after laser irradiation (230 mJ cm^{-2}). Magnified SEM images (lower right corner inset) and measured water contact angles (upper left corner inset) of a ZnO NW array are also shown. a,b) Reproduced with permission.[32] Copyright 2012, Springer-Verlag. Effect of laser treatment on the surface morphology of ZnO epitaxial layers: c) pristine and d) laser annealed samples. c,d) Reproduced with permission.[173] Copyright 2014, IOP Publishing Ltd. e–g) Photographs of the sequential movement of a water droplet along a predesigned hydrophilic guiding track created by laser writing on the superhydrophobic TiO_2 NW array surface. e–g) Reproduced with permission.[174] Copyright 2015, The Royal Society of Chemistry.

cloud, resulting in cooling and shrinkage of the cluster cloud. Subsequently, recrystallization at the outermost region, formation of a closed shell, and absorption of the encircled clusters onto its inside wall led to recrystallization and formation of ZnO hollow nanospheres on the top of the corresponding ZnO NWs. The as-synthesized ZnO NWs exhibited hydrophilic behavior with a water contact angle of 20 °C (inset of Figure 16a), whereas the laser irradiated sample showed hydrophobic behavior with a water contact angle of 120 °C (inset of Figure 16b). This change in surface wettability was attributed to the reduction in the surface energy of the ZnO NWs by the formation of ZnO hollow nanospheres.

Molaei et al.[173] reported that a hydrophobic ZnO thin film changes to hydrophilic after laser irradiation. In their work, ZnO thin films were deposited onto cubic yttria-stabilized zirconia (c-YSZ)/Si (111) substrates by PLD and laser-treated in an ambient environment by an excimer KrF laser (0.22 J cm^{-2}). The surface roughness was found to decrease from 16.71 to 3.68 nm under laser irradiation (Figure 16c,d).[173] Hydrophobic behavior was observed in the as-deposited ZnO due to the higher surface roughness and lower surface energy. Under laser irradiation, the ZnO surface became more reactive by creating oxygen vacancies and broken bonds, which increased the surface energy of the ZnO film, imparting hydrophilic behavior.

Patterning methods, such as photolithography, and microcontact-printing techniques are used to construct wetting micropatterns on a material surface to enhance its wettability performance. However, these methods require expensive and multistep processing. The laser-patterning technique is considered an alternative approach for fabricating a wetting micropattern in just a single step. Recently, femtosecond laser irradiation was utilized to create a 3D wettability pattern on a superhydrophobic TiO_2 nanotube array (TNA).[174] The superhydrophobic TNA surface was fabricated through electrochemical anodization of a Ti sheet followed by its soaking in 1H,1H,2H,2H-perfluorooctyltriethoxysilane and baking at 140 °C for 1 h. A micropattern (20 μm in width) on the TNA surface was created using a solid-state IR laser (800 nm, 0.5 mW, 5 mm s^{-1}, 150 fs, 1 kHz). Figure 16e–g shows the sequential movement of the droplet along the hydrophilic pattern created by the laser writing on the superhydrophobic TNA surface under the combined influence of the gravitational force, the high adhesion of the hydrophilic micropattern, and the antispreading nature of the superhydrophobic neighboring boundary.[174] The laser processing can provide high-contrast wettability patterning surfaces and fast switching between superhydrophilic and superhydrophobic properties in a single step.

4.4. Electrochromic Switching

Direct patterning of inorganic materials using electrohydrodynamic lithography (EHL) has attracted great attention owing to its cost effectiveness, flexibility, and large-area high-resolution patterning capability. After the EHL process, the materials must be annealed at high temperature for functionalization. To enable rapid fabrication of devices, Cha et al.[37] coupled the EHL patterning process with laser annealing. Enhanced switching performance was reported for an EHL-patterned TiO_2 ETL, in an electrochromic device, annealed by laser irradiation. Initially, TiO_2 layers were coated on both target and master pattern substrates (Si and ITO-coated glass) using a spin-coating technique. Subsequently, sub-50 nm pattern structures were obtained within 10 min by using an EHL patterning method (**Figure 17**a). The patterned films were annealed using a CW IR laser (Nd:YAG, 1064 nm). Figure 17b shows the Raman spectra of the laser annealed EHL-transferred TiO_2 patterns at different laser powers with the annealing time of 30 s. The E_g mode

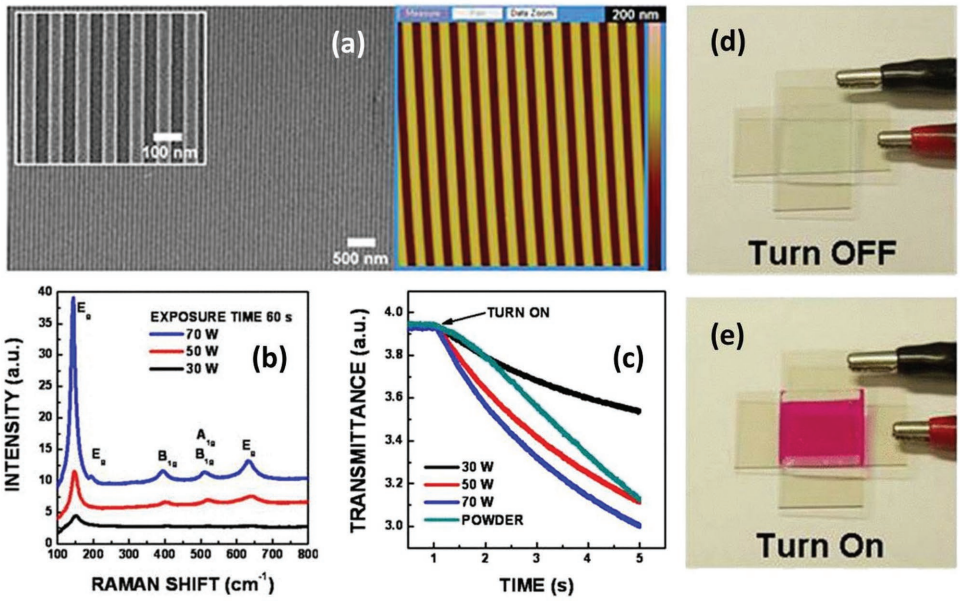

Figure 17. a) SEM and AFM images of the TiO_2 pattern fabricated by the EHL method. b) Raman spectra of the TiO_2 layer on the ITO/glass substrate at different laser powers. c) Switching performance of the electrochromic device. Higher laser power results in a faster and enhanced color contrast. d,e) Images of electrochromic cells and the color change observed with applied bias. Reproduced with permission.[37] Copyright 2013, AIP Publishing LLC.

at 143 cm^{-1} originates from the external vibration of the anatase structure. The peak shift observed in the Raman spectra is due to the phonon-confinement effect, depending on the nanocrystal size. The intensity improvement of the E_g mode with the applied laser power (30–70 W) indicated the development of anatase TiO_2 with improved crystallinity and grain size, confirmed further by microstructural analysis. An electrochromic device was fabricated using patterned TiO_2 on a transparent ITO substrate followed by laser annealing. The performance of the electrochromic device was examined as a function of applied laser power, as shown in Figure 17c. The device was transparent in the off condition, while reduction in the transmittance with a clear color change was noticed under an applied bias (Figure 17d,e). Here, the TiO_2 layer acted as an ETL, controlling the contrast and switching time of the electrochromic device. The fast response time and large change in transmittance of the high-power-laser-annealed TiO_2 film was attributed to the higher crystallinity and increased electron-transport efficiency.

4.5. Resistive Switching

In the resistive-switching (RS) effect, the resistance of the material can be modulated between a high resistance state (HRS) and a low resistance state (LRS) through the application of an electric field. The materials exhibiting the RS effect have applications in nonvolatile memories such as resistive random-access memories and artificial synapses. Defects in a material, such as oxygen vacancies, are known to play an important role in inducing RS behavior. To create oxygen vacancies or tune their concentration in oxide thin films, variation in the oxygen partial pressure during deposition, thermal annealing, and other postprocessing operations has been employed.[34] Recently, Silva et al.[35] demonstrated the effect of light intensity on the resistive-switching behavior of laser annealed $Ba_{0.8}Sr_{0.2}TiO_3$ ferroelectric thin films. A ferroelectric/semiconductor (BST/ITO) structure was employed as the semiconductor layer as the electrode is expected to be beneficial for the RS effect. The BST/ITO heterostructure deposited on a glass substrate, using PLD, was annealed under excimer laser irradiation (80 mJ cm^{-2}, 25 ns, 5 Hz) to promote crystallization. The XRD pattern of as-grown BST/ITO heterostructures exhibited only the peaks related to ITO, due to the amorphous nature of the BST film. The appearance of BST peaks with significant intensity indicated improved crystallinity because of the laser annealing.

The RS behavior of the BST film was examined using current–voltage (I–V) characteristics, measured in the dark and at different light intensities (5–60 mW cm^{-2}), as shown in **Figure 18**a. The I–V curves exhibited two different resistive states, HRS and LRS, and slightly asymmetric behavior due

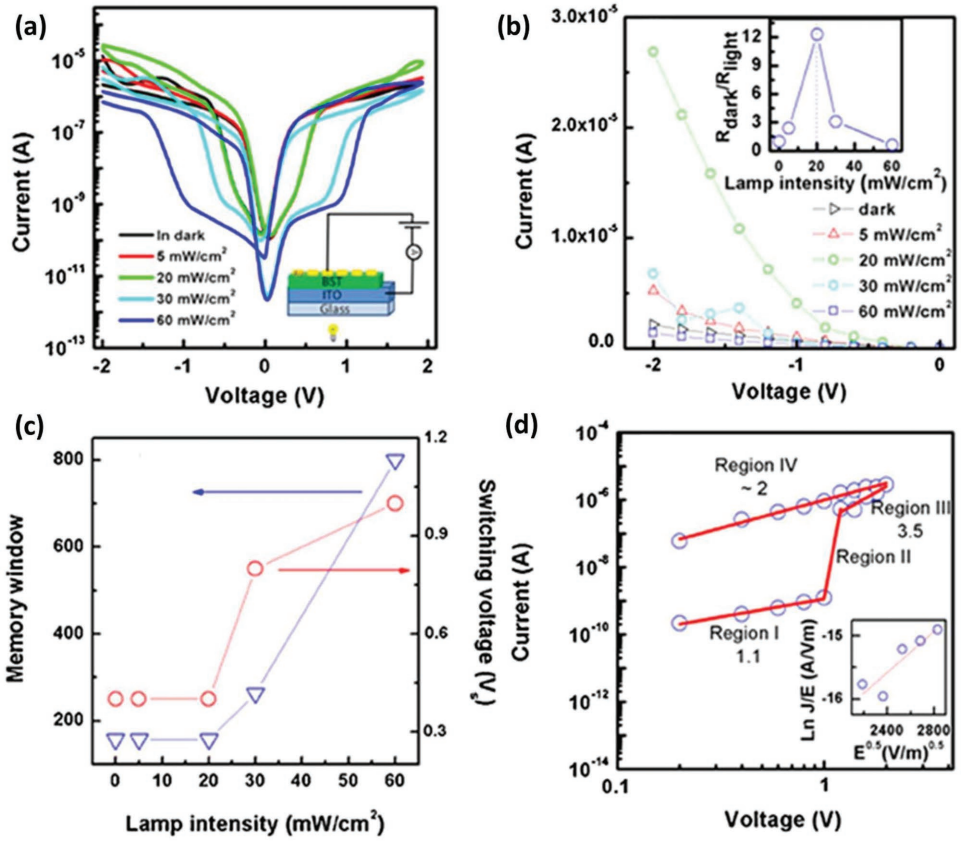

Figure 18. a) Current–voltage (I–V) measurements of $Ba_{0.8}Sr_{0.2}TiO_3$/ITO heterostructure in the dark and under light. b) I–V characteristics in the low resistance state and the ratio of R_{dark}/R_{light} versus light intensity (inset). c) Dependence of memory window (HRS/LRS) and switching voltage (V_s) on the light intensity. d) Linear fittings to the I–V curve obtained at 60 mW cm^{-2} light intensity, for the positive-bias region. The inset shows the plot of the leakage current density and electric-field ratio (J/E) versus $E^{0.5}$ with a linear fit. Reproduced with permission.[35] Copyright 2015, Wiley-VCH.

to the difference in the charge distribution at the ferroelectric/semiconductor interface (Schottky barrier). The effect of light intensity on the RS behavior was examined by analyzing the current of the LRS state measured at different light intensities, as shown in Figure 18b. Under white-light illumination, the current and the ratio between the dark and light resistance (R_{dark}/R_{light}) were found to increase with light intensity up to 20 mW cm^{-2}, and this was attributed to the photovoltaic effect. For a light intensity ≥30 mW cm^{-2}, the current was found to decrease due to the electrostatic nonequilibrium created by the accumulation of the large number of photogenerated charge carriers at the BST/ITO interface. This phenomenon led to an enhancement in the resistance of the HRS (≈2 times), the memory window (5 times) and the switching voltage under white-light illumination (60 mW cm^{-2}) compared to the dark measurement (Figure 18c). Figure 18d shows the linear fitting to the *I*–*V* curve of the BST film illuminated at 60 mW cm^{-2}. These results revealed that HRS follows Ohmic behavior, whereas the LRS follows bulk-limited conduction mechanisms such as the Poole–Frenkel and space-charge-limited conduction mechanisms. Similarly, the RS effect was also observed in a laser-annealed STO single crystals, where the laser-induced oxygen vacancies were responsible for the RS behavior.[34]

4.6. Metal-to-Insulator Transitions

The MIT in strongly correlated electron systems is of interest for applications to infrared detectors (e.g., bolometers), electrooptic switches, and memory elements.[175] Vanadium dioxide (VO_2) is one of the most studied correlated electron systems that exhibits a dramatic MIT at ≈68 °C along with a high temperature coefficient of resistance. Using conventional preparation methods, achieving single-phase VO_2 is difficult owing to the different valence states of VO_x phases and the high-temperature requirement for crystallization. The processing temperature required should be ≤300 °C to achieve a broad MIT with narrow hysteresis in VO_2. To solve this issue, Nishikawa et al.[176] conducted laser annealing of VO_2 films, synthesized by MOD, using a KrF excimer laser (248 nm, 60–100 mJ cm^{-2}). The film irradiated at 60 mJ cm^{-2} for 10 min exhibited only the amorphous phase without MIT (**Figure 19**a). However, the epitaxial VO_2 phase started to grow near the film–substrate interface, while the rest of the film was still amorphous when irradiated under a high laser fluence (100 mJ cm^{-2} for 10 min) resulting in a broad and non-hysteretic MIT (inset of Figure 19b). Interestingly, the film irradiated at 100 mJ cm^{-2} for 60 min exhibited a single phase

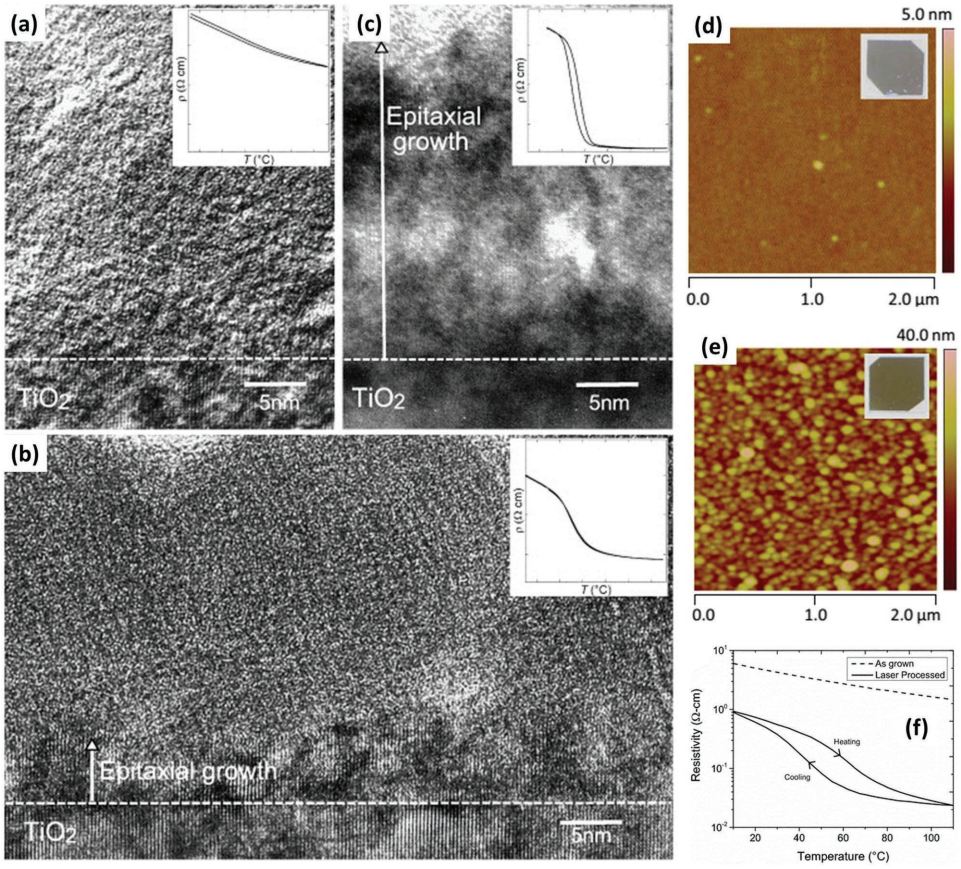

Figure 19. Cross-sectional TEM images and resistivity–temperature (*ρ*–*T*) curves of VO_2 films: irradiated at a) 60 mJ cm^{-2} for 10 min, b) 100 mJ cm^{-2} for 10 min, and c) 100 mJ cm^{-2} for 60 min, after preheating at 300 °C. a–c) Reproduced with permission.[176] Copyright 2010, Elsevier B.V. d,e) AFM images and optical microscopy images (insets) of as-grown VO_x and femtosecond-laser-processed VO_2 films, respectively. The as-grown VO_x film showed an extremely smooth surface (rms roughness = 0.3 nm), while the laser-processed film showed a rougher surface (rms roughness = 4.3 nm). f) *ρ*–*T* data for the as-grown and laser-processed films. d–f) Reproduced with permission.[36] Copyright 2016, Springer-Verlag.

of epitaxial VO_2 throughout the film and a typical MIT with significant hysteresis (Figure 19c). The increased degree of the epitaxial phase in the VO_2 film by laser annealing led to a sharper MIT with broad hysteresis.

Charipar et al.[36] studied the MIT characteristics in laser-annealed VO_2 thin films. PLD-deposited VO_2 thin films were annealed using an Yb femtosecond pulsed laser (248 nm, 80–140 mJ cm^{-2}, 280 fs, 200 kHz). XRD analysis of as-grown and annealed films indicated a change in the phase structure from amorphous (VO_x) to crystalline (VO_2), induced by the laser irradiation. After laser treatment (123 mJ cm^{-2}), the color of the film changed to a transparent yellow shade, characteristic of VO_2. The surface morphology of the as-deposited VO_x and laser annealed VO_2 examined by AFM (Figure 19d,e) revealed an increase in surface roughness from 0.3 to 4.3 nm after laser irradiation, which is typical of crystalline VO_2 thin films processed at elevated temperatures. Temperature-dependent resistivity measurements were conducted to investigate the MIT behavior (Figure 19f). The as-deposited VO_x film did not show any MIT, but the laser annealed VO_2 film exhibited a distinct MIT with broad hysteresis and improved conductivity due to improved crystallinity. The broad nature of both the hysteresis width and the sharpness of the transition were attributed to the incomplete crystallization and the nonstoichiometry of the film. The low resistivity of the film compared to the resistivity of a pure VO_2 film suggested that the laser annealed film is still oxygen deficient. Optimization of the deposition and the laser irradiation conditions are necessary to obtain high-quality VO_2 films.

5. Recent Progress and Advances in Laser Processing of Metal Oxides

5.1. Crystal Growth of Amorphous Metal Oxide Films

Polycrystalline and epitaxial growth of various MO films (**Table 2**) has been demonstrated using laser irradiation of amorphous layers derived from CSD methods.[5,10,180–187] UV lasers have been the preferred choice in these studies due to the higher optical absorbance of MOs in the UV range. Several studies have been conducted by Tsuchiya and co-workers to understand the UV-laser-assisted nucleation and growth of oxide films synthesized by the MOD method.[5] The MOD precursor layers were preheated (<500 °C) to evaporate the organic components and the obtained amorphous films were annealed with a UV laser (KrF/ArF). During the laser-assisted epitaxial growth of oxides on single-crystal substrates with minimal lattice mismatch (**Figure 20**a,d), initial photoabsorption occurs on the substrate surface, and crystal nucleation occurs through chemical bonding between the molecular structures protruding on the substrate surface and the amorphous oxide layer. Subsequently, crystals will begin to grow epitaxially at the substrate surface, and the amorphous material continues to crystallize in the epitaxial region due to further photochemical activation of the emergent crystal nuclei. The laser-induced photothermal heating accelerates ion migration and assists in enhancing the growth rate. The epitaxial growth proceeds upward from the substrate surface to the film surface without any polycrystalline nucleation in the amorphous matrix. In the case of polycrystalline growth of the oxide films on amorphous substrates, two

Table 2. Examples of laser-assisted crystal growth of metal oxide films. MOD: metal organic deposition, CSD: chemical solution deposition. Redrawn using the data reported in refs. [5] and [10].

Metal oxide	Solution type	Laser	Substrate	Crystalline form	Reference
TiO_2	Sol–gel	ArF (193 nm)	Glass	Polycrystalline	[180]
Fe_2O_3	MOD	ArF (193 nm)	Glass	Polycrystalline	[180]
ZnO	Sol–gel	KrF (248 nm)	Glass	Polycrystalline	[181]
In_2O_3	Sol–gel	ArF (193 nm)	Glass	Polycrystalline	[182]
		Nd:YAG (266 nm)			
Sn-doped In_2O_3	NPs	KrF (248 nm)	Glass	Polycrystalline	[126]
VO_2	MOD	KrF (248 nm)	TiO_2 (001)	Epitaxial	[176]
WO_3	NPs	KrF (248 nm)	Glass	Polycrystalline	[134]
$PbTiO_3$	MOD	ArF (193 nm)	Glass, Si	Polycrystalline	[183]
$Ba_{0.7}Sr_{0.3}TiO_3$	Sol–gel	KrF (248 nm)	$Pt/TiO_2/SiO_2/Si$	Polycrystalline	[113]
$La_{0.8}Sr_{0.2}MnO_3$	MOD	ArF (193 nm)	$LaAlO_3$ (100)	Epitaxial	[184]
		KrF (248 nm)	$SrTiO_3$ (100)		
		XeCl (308 nm)			
$PbZr_{0.53}Ti_{0.47}O_3$	Sol–gel	KrF (248 nm)	$LaNiO_3/Si$	Polycrystalline	[185]
Sn-doped SnO_2	NP	KrF (248 nm)	Polyester	Polycrystalline	[186]
$RbLaNb_2O_7$	MOD	KrF (248 nm)	Glass	1D-oriented, polycrystalline	[187]
$Ce_{0.9}Zr_{0.1}O_{2-y}$	CSD	Nd:YAG (266 nm)	Y_2O_3:ZrO_2 (001)	Epitaxial	[10]
$LaNiO_3$	CSD	Nd:YAG (266 nm)	$SrTiO_3$ (001)	Epitaxial	[10]
$Ba_{0.8}Sr_{0.2}Ti_{O3}$	CSD	Nd:YAG (266 nm)	$LaNiO_3/LaAlO_3$ (001)	Epitaxial	[10]
$La_{0.7}Sr_{0.3}Mn_{O3}$	CSD	Nd:YAG (266 nm)	$SrTiO_3$ (001)	Epitaxial	[10]

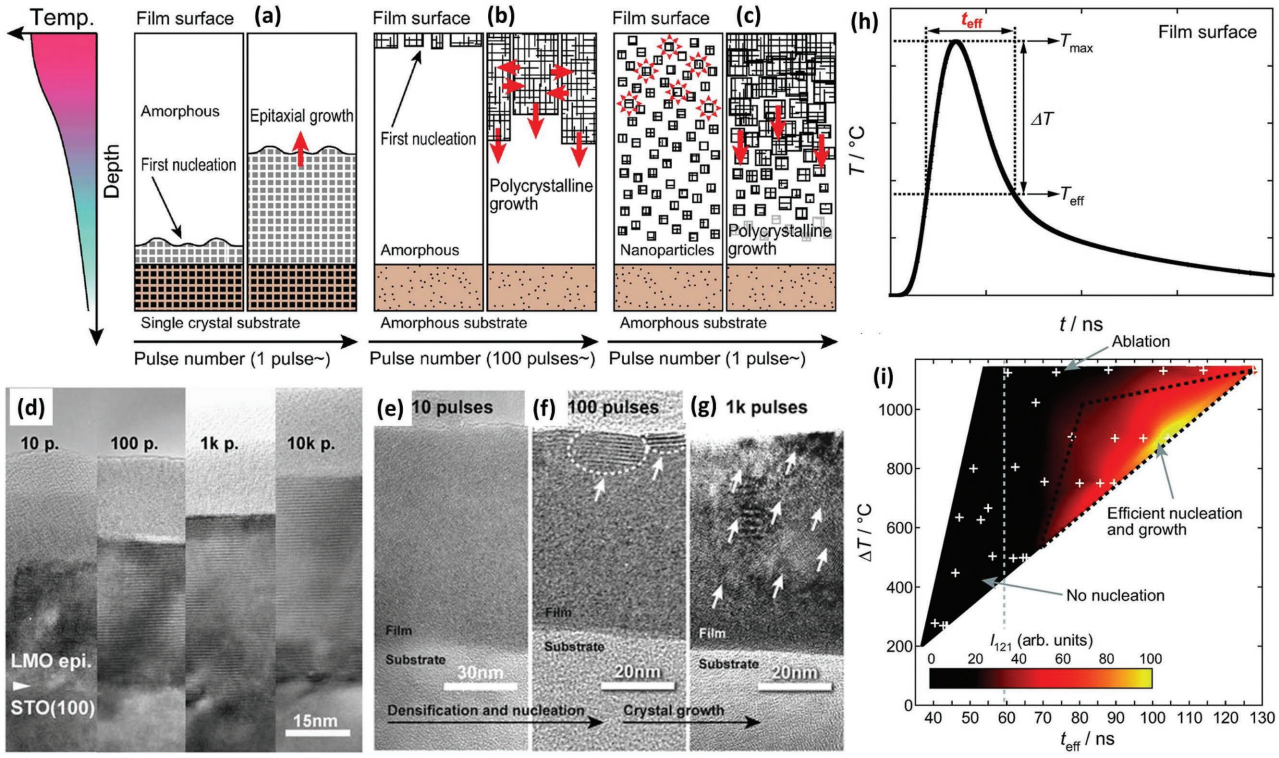

Figure 20. a–c) Schematics describing the crystal growth of oxide thin films from an amorphous matrix under excimer laser irradiation in the case of a single-crystal substrate (a) and amorphous substrates without (b) and with (c) crystal seeds. a–c) Reproduced with permission.[5] Copyright 2013, The Royal Society of Chemistry. d–g) Evolution of epitaxial structure of $LaMnO_3$ film on $SrTiO_3$(100) (d) and polycrystalline structure of $LaMnO_3$ film on glass (e,g), with respect to the number of laser pulses. The white arrows and dotted lines represent the crystalline domain and phase boundary, respectively. h) Simulated temperature-variation plot as a function of time, at precursor film surface under UV laser irradiation, based on 1D heat flow. T_{max}, T_{eff}, and t_{eff} represent the maximum temperature, the effective temperature for crystallization, and the effective time for crystallization, respectively. i) Contour map of the t_{eff} and ΔT dependence of the 121 peak intensities of $LaMnO_3$ thin films. White crosses indicate data points. T_{max} and T_{eff} in this system were 1920 and 790 °C, respectively. d) Reproduced with permission.[177] Copyright 2009, Elsevier B.V. e–i) Reproduced with permission.[178] Copyright 2009, The Japan Society of Applied Physics.

scenarios of nucleation and growth of crystals have been put forward: (i) in amorphous films with no pre-existing nucleation sites (Figure 20b,e–g), crystal nucleation begins at the film surface due to a photothermal heating effect. Subsequent polycrystalline crystal growth progresses from the emergent crystal nuclei near the film surface toward the substrate interface; (ii) when the amorphous matrix originally contains crystal nuclei (Figure 20c), crystal growth proceeds from the effective nucleation sites, primarily due to photochemical activation processes that create new bonds at the reaction interface.

Tsuchiya and co-workers hypothesized that the effective annealing time (t_{eff}) is an appropriate universal value for evaluating the pulsed-laser-induced polycrystalline nucleation of oxides.[178,179] The t_{eff} is defined as the time in which the temperature at the film surface increases over the effective annealing temperature (T_{eff}) for the crystallization of the film in a conventional furnace heating (Figure 20h). The evaluation of t_{eff} was initially carried out for perovskite $LaMnO_3$ (LMO) amorphous films spin-coated onto substrates (silica glass (SG), LAO, SG coated LAO, and Si) with different diffusivities (D). By examining the XRD patterns of all the laser annealed LMO films on different substrates, a contour map of the (121) Bragg peak intensities of the LMO films was plotted as a function of t_{eff} and ΔT (= T_{max} − T_{eff}) (Figure 20i). These data indicate that high-fluence laser irradiation does not necessarily produce good-quality films, as the ablation rate appears to substantially exceed the crystal growth rate at high T_{max}. The threshold value of t_{eff} for initial crystal nucleation of LMO films was found to be ≈60 ns. Experimentally, the threshold t_{eff} can be controlled by changing the wavelength of the incident laser, as well as the fluence and the thickness and temperature of the substrate. Based on the experiments and other simulations on polycrystalline oxides having various crystal structures, including bixbyite ITO, anatase TiO_2, pyrochlore $La_2Zr_2O_7$, and perovskite $RbLaNb_2O_7$, the threshold value of t_{eff} for nucleation was estimated to fall typically in the range of 58–67 ns and appear almost independent of the crystal structure or composition. The above studies confirmed that the concept of a threshold t_{eff} value can be applied universally to the initiation of crystal growth in various oxides in response to pulsed-UV-laser irradiation, highly beneficial for better understanding and control of the nucleation process.

Queraltó et al.[10] conducted UV-laser-assisted (Nd:YAG, 266 nm, 20–40 mJ cm^{-2}) epitaxial growth of CSD-derived oxide thin films of $Ce_{0.9}Zr_{0.1}O_{2-\gamma}$ (CZO), LNO, $Ba_{0.8}Sr_{0.2}TiO_3$, and $La_{0.7}Sr_{0.3}MnO_3$ on single-crystal substrates (Y_2O_3:ZrO_2, LAO,

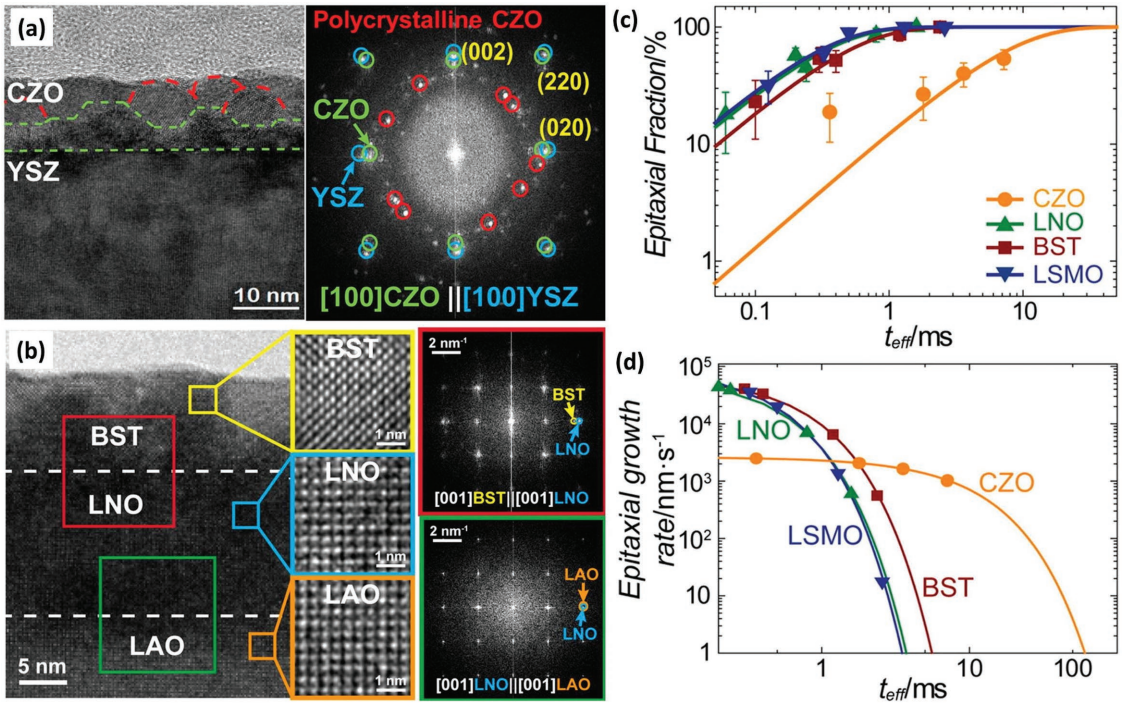

Figure 21. a,b) Microstructural characterization of laser irradiated epitaxial films of $Ce_{0.9}Zr_{0.1}O_{2-y}$ on YSZ and $Ba_{0.8}Sr_{0.2}TiO_3$ on LNO/LAO, respectively. The colored frames correspond to the different areas investigated. c,d) Epitaxial fractions and growth rates determined for the $Ce_{0.9}Zr_{0.1}O_{2-y}$, $LaNiO_3$, $Ba_{0.8}Sr_{0.2}TiO_3$, and $La_{0.7}Sr_{0.3}MnO_3$ laser irradiated films, respectively. Quantification of epitaxial fractions of the films was done by means of 2D XRD measurements and the values of epitaxial growth rate were obtained by deriving the fitted curves of epitaxial fractions with respect to the effective heating time and multiplying by the final film thickness. Reproduced with permission.[10] Copyright 2016, American Chemical Society.

and STO). The estimated t_{eff} values were found to be widely dispersed (5–65 ns), depending strongly on the laser fluence and the material system due to the different optical and thermophysical parameters of the different oxide components. Microstructural features of laser irradiated (40 mJ cm^{-2}, 20 000 pulses per site) CZO/YSZ and BST/LNO/LAO samples observed by high-resolution TEM are presented in **Figure 21**a,b. The CZO film contained both polycrystalline and epitaxial regions, whereas the BST film was completely epitaxial, as evidenced by the respective fast Fourier transform spectra. Figure 21c displays the quantification of the epitaxial fraction from 2D XRD measurements for laser annealed CZO (20 nm thick), LNO (25 nm thick), BST (30 nm thick), and LSMO (35 nm thick) films as a function of the overall t_{eff}. For all the films, the degree of epitaxy was found to increase with the t_{eff}, i.e., as more pulses per site were accumulated. The epitaxial transformation of the LNO, BST, and LSMO films was found to be an order of magnitude faster than the epitaxial transformation of the CZO film. The epitaxial growth rates of the films (Figure 21d) have an initial value that decreases with t_{eff} as the epitaxial growth proceeds, suggesting that the driving force toward epitaxial crystallization is higher at the beginning and is reduced as less polycrystalline material can transform. The estimated epitaxial growth rates of the LNO, BST, and LSMO films were approximately two orders of magnitude higher than the estimated epitaxial growth rate of the CZO film. The diffusion coefficient of CZO/YSZ was approximately an order of magnitude smaller than the other MO systems studied, which could explain the variation in growth rates.

5.2. Production of Metal Oxide NPs by Laser Ablation in Liquid

In the past two decades, the laser ablation technique has been applied successfully to the synthesis of metallic, as well as oxide, NPs.[61,58–60,188,189] This process, called laser ablation in liquid (LAL), produces NPs from an ionized plasma or plume generated by the laser interaction with a solid target immersed in a liquid (**Figure 22**a). The plasma is composed of highly ionized or atomic species originating from the target material. The duration of the plasma is generally in the range of nanoseconds to microseconds for each laser pulse, depending on the laser parameters and the liquid composition.[190] During plasma generation and decay, photoionization of the target materials and photothermal decomposition of the solvent occur simultaneously, creating an excited environment for chemical reactions. Then, rapid quenching of the plasma occurs, and the vapor layer grows into a cavitation bubble, which undergoes periodic expansion and shrinkage until it collapses. During this period, the excited species from the ablated solid interact with the surrounding liquid molecules (dissolved molecular or water-bound oxygen) and undergo chemical reactions leading to solid crystallization and formation of atom clusters as well as primary particles. The volume and lifetime of the bubble depend on the laser fluence.[191] The peak temperature and pressure evolved during the bubble collapse create conditions for the nucleation and growth of NPs, which disperse further into the liquid.

Although the synthesis of NPs by the LAL process has been widely studied, the fundamental mechanisms of particle formation and the key processes that control the particle characteristics

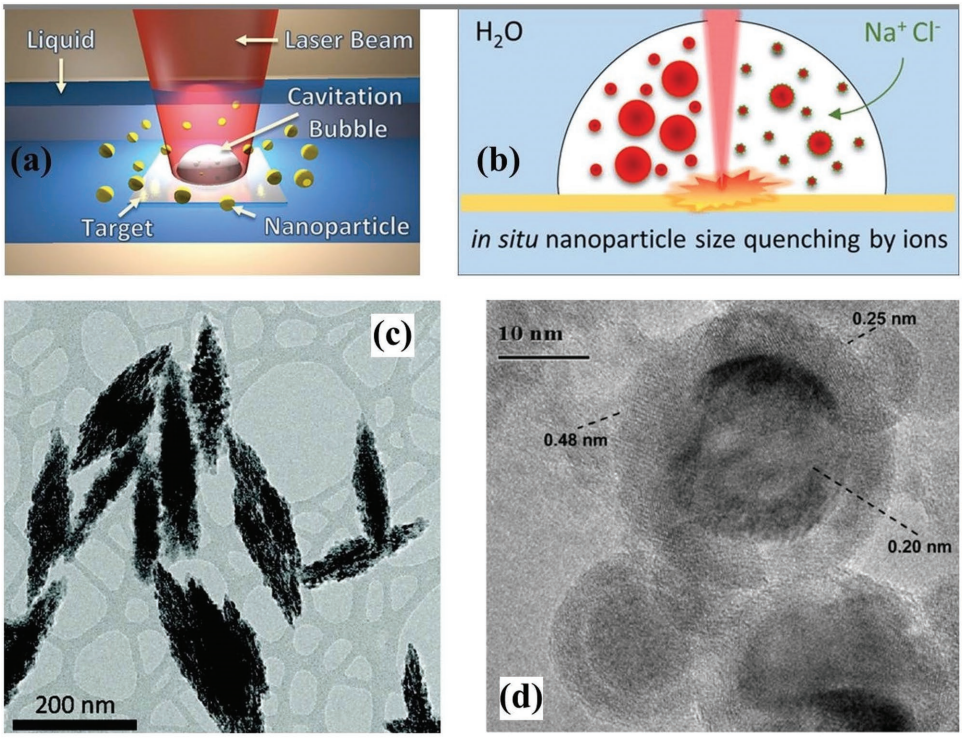

Figure 22. a) Scheme of laser ablation in liquid (LAL), where the laser-beam interaction with a solid target leads to the formation of plasma and a cavitation bubble. Ablated matter condensed in the bubble gives rise to NPs, which disperse into the liquid after the collapse of the bubble. Reproduced with permission.[58] Copyright 2017, American Chemical Society. b) Schematic illustration of particle size quenching by ions inside a cavitation bubble. Reproduced with permission.[192] Copyright 2017, American Chemical Society. c) TEM image of CuO nanospindles obtained by the LAL method. Reproduced with permission.[52] Copyright 2009, American Chemical Society. d) TEM image of iron and iron oxide core–shell particles, produced by the LAL process, with interplanar distances of 0.20 nm (α-Fe) in the core and of 0.25 (Fe_3O_4) and 0.48 nm (γ-Fe_2O_3) in the shell. Reproduced with permission.[57] Copyright 2010, American Chemical Society.

are not fully understood yet.[192,193] Recent atomistic simulation studies suggest that explosive decomposition of the metal target leads to the generation of primary particles, and a further breakup of superheated molten metal at the plasma–water interface results in secondary particle formation.[193] Letzel et. al.[192] investigated the particle-size quenching effects by dissolved ions of electrolyte added to the liquid prior to laser ablation. Through in situ and ex situ experiments, it was demonstrated that size reduction by NP–ion interactions during the LAL is in fact a gas-phase phenomenon and happens inside the laser-induced cavitation bubble (Figure 22b).[192] It was hypothesized that the ions enter the cavitation bubble, resulting in surface charges that give rise to electrostatic repulsive forces between particles. This causes particle-size reduction and stabilization against particle agglomeration and growth. It is interesting to note that the NPs formed by LAL are actually produced in a vapor phase. However, the plasma plume generated in LAL is confined in a small region unlike that observed during laser ablation in other environments (e.g., air, gas, and vacuum) where a larger volume of the plume is created.

In the LAL process, the size, shape, morphology, and microstructure of NPs that are strongly related to the physical and chemical properties can be tuned by simply varying the laser parameters (e.g., wavelength, energy, dwell time, and spot size) and liquid medium conditions (e.g., viscosity, temperature, concentration, and stir rate).[61,189] This process is applicable to most solid targets and produces stable and phase-pure NPs with high dispersion. The LAL method has been utilized to produce NPs of several pure and doped metal oxides including CuO[52] (Figure 22c), MnO_x,[53] $Y_3Fe_5O_{12}$,[54] Ag/TiO_2,[55] Y_2O_3:Eu^{3+}, Gd_2O_3:Eu^{3+}, $Y_3Al_5O_{12}$:Ce^{3+} (YAG:Ce),[56] Fe@Fe_2O_3 or Fe_3O_4[57] (Figure 22d), etc.[58–61,188,189] Considering the wide applicability of LAL, a higher productivity of the process is essential for its industrial implementation. However, productivities on the order of mg h^{-1} have been reported for the LAL process, which are lower when compared to wet-chemical and gas-phase synthesis of NPs. In the past few years, many efforts have been undertaken to enhance the productivity of LAL by means of optimizing the laser parameters (power, scan speed, repetition rate), target geometry, and cavitation bubble dynamics.[194–197] Recently, it has been demonstrated that productivities >4 g h^{-1} can be achieved with LAL for the synthesis of several metal (Pt, Au, Ag, Al, Cu, and Ti) NPs.[194,195] Such an accomplishment of boosted productivity suggests the economic competitiveness of the LAL process for the mass production of NPs and its huge potential for large-scale applications.

5.3. Selective Growth of Metal Oxide Nanostructures

As an alternative to the complex and multistep conventional synthesis, growth, and patterning of MO nanostructures, laser-induced direct selective growth of nanostructures has

recently been proposed.[11] Rapid, single-step, and site-specific growth of MO NWs directly on 3D structures using the laser-induced hydrothermal growth (LIHG) method has been demonstrated.[41–43] The simple and straightforward LIHG process typically involves irradiation of the target sample immersed in a precursor solution with a focused laser beam (**Figure 23**a), which creates a confined temperature field inside the liquid. Natural convection produced by the temperature gradient from the confined temperature field and potential superheating on the micrometer-scale induce the localized growth of NWs. Yeo et al.[41] reported the site-specific growth and integration of ZnO NWs (≈10 µm in length) directly on the premade arbitrary 3D structures at high precision simply by focusing the laser at the target point, which is not possible using conventional processing schemes (Figure 23b). Here, a sample of a ZnO NP seed layer spin-coated on a Au/Cr buffered glass substrate immersed in the ZnO precursor solution was irradiated using a CW laser (Nd:YAG, 532 nm, 130 mW, 30 min). The LIHG process in the bottom-focusing mode yielded longer and better quality NWs because of the elimination of optical disturbances and scattering by the growing NWs to the laser beam compared with the top-focusing mode (NWs growing against the laser path). Furthermore, in situ monitoring of the growth kinetics revealed that the growth rate of the NWs is largely higher in the LIHG process, compared to conventional hydrothermal methods, attributed to growth localization suppressing the precursor depletion occurring by homogeneous growth reactions, as well as enhancing the mass transport of precursor molecules.[43] However, the NW growth was limited by the heat dissipation through the growing NWs acting as thermal fins.

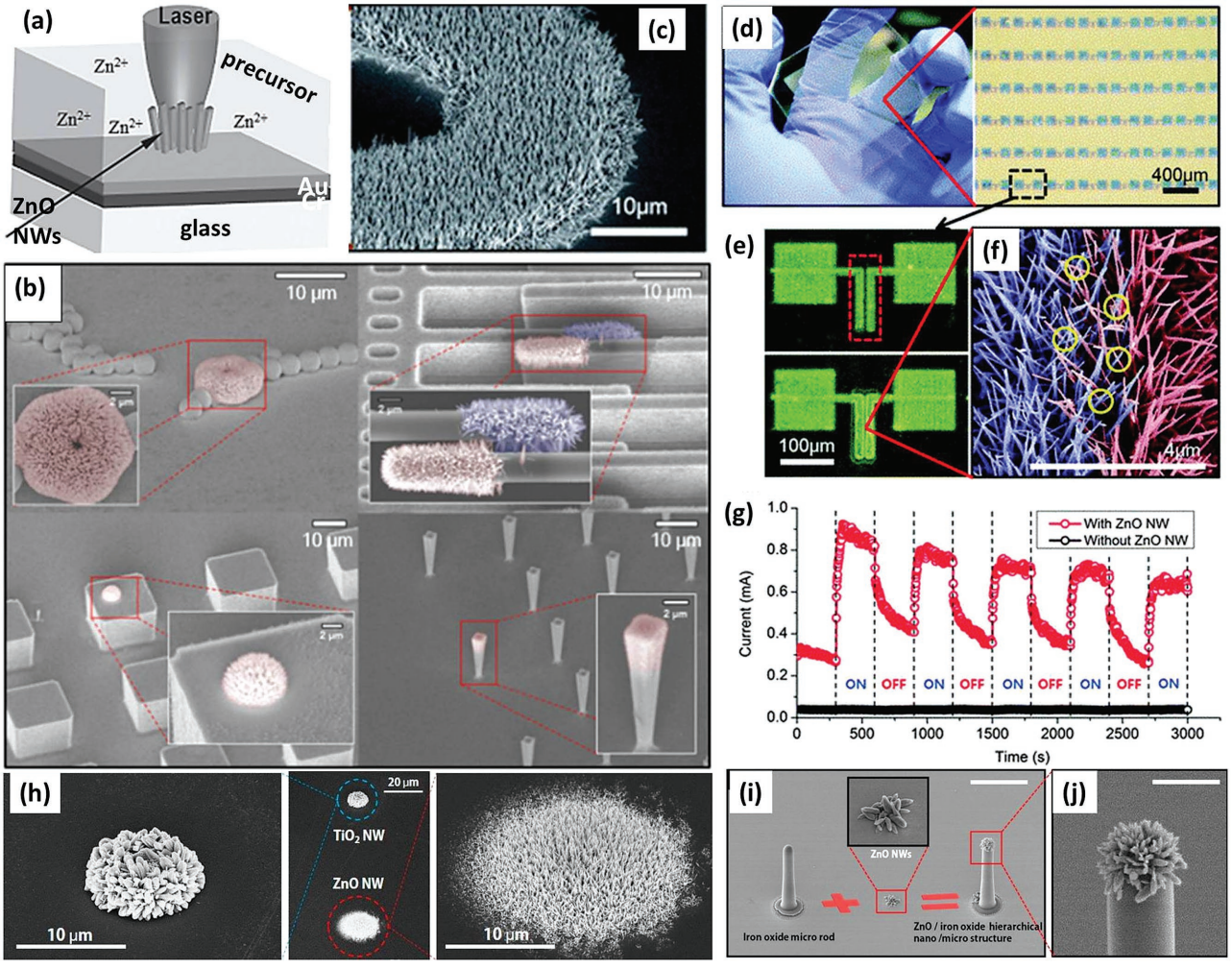

Figure 23. a) Schematic diagram of laser-induced hydrothermal growth (LIHG) process (top focusing). b) SEM images of the ZnO NW arrays grown on various 3D structures of Si. a,b) Reproduced with permission.[41] Copyright 2013, Wiley-VCH. c) SEM image of part of a large-area ZnO NW pattern grown from a laser-decomposed zinc acetate layer. d–g) Demonstration of a fully digital all-laser-processed electronics fabrication d) UV-detector arrays fabricated by selective laser sintering of Ag NP ink (metal electrodes) and subsequent laser-assisted growth of ZnO NWs (active layer). e) Optical images of a UV detector before and after the ZnO NW growth (at the red-dotted region). f) SEM image of the ZnO NW networks grown and the junction formed (yellow circles) between the Ag electrodes. g) Typical response of a UV sensor with and without ZnO NWs. c–g) Reproduced with permission.[42] Copyright 2013, The Royal Society of Chemistry. h–j) SEM images of TiO_2 NW and ZnO NW grown on the same flexible PI substrate, iron oxide microrods, and ZnO/iron oxide hierarchical nano/microstructure, respectively. h) Reproduced with permission.[44] Copyright 2015, American Chemical Society. i,j) Reproduced with permission.[45] Copyright 2014, American Chemical Society.

This heat dissipation could be counteracted by tailored temporal modulation of the input laser power to enable sustained growth to extended dimensions (≈60 µm in length).

To extend the LIHG process to grow NWs on a large scale, initial laser patterning of ZnO NP seeds and subsequent NW growth by conventional hydrothermal synthesis were carried out (Figure 23c).[42] To demonstrate the feasibility of the above process to large-area device fabrication, a UV sensor array was designed. As the conductivity of ZnO varies upon exposure to UV light, ZnO NWs with a high surface-to-volume ratio are appropriate for a photoconductive UV sensor with high sensitivity. During fabrication of the UV sensor array, the Ag metal electrode pads were patterned initially by selective laser sintering of Ag NP ink spin-coated on a glass substrate. Then, ZnO NWs were selectively grown from the laser-patterned ZnO NP seeds, to form the UV-sensitive channel between two adjacent metal electrode pads (Figure 23d–g). The photoconductivity of an arbitrary UV sensor was investigated by measuring the transient current change under UV light. Figure 23g shows the obvious difference in the sensitivity of a typical UV sensor with and without ZnO NWs under UV-light exposure. The LIHG process has further been employed to grow heterogeneous MO NWs (ZnO and TiO_2) on the same substrate (Figure 23h), trans-scale hierarchical structures of ZnO NWs on Fe_2O_3 microrods (Figure 23i,j), and growth of ZnO NRs decorated with Ag NPs.[44–46] The fully digital laser-assisted growth approach discussed above is also promising for nanosensor integration, which requires the highly selective growth of functional nanostructures.

5.4. Self-Assembly and Patterning of Metal Oxide Nanostructures

For low-cost and large-scale fabrication purposes, development of simple and direct patterning methods that do not require templating or masking is highly desired. Recently, the formation of multiscale patterns of nanostructured materials through directed self-assembly under laser radiation has generated extensive research interest. This technique is based on the utilization of long-range forces such as the capillary force and surface tension or convection, to construct patterned structures via a self-assembly approach at the nano/mesoscale level. Laser-assisted patterning of a variety of materials, such as CdSe/ZnS quantum dots, polyoxometalates, glycine single crystals, carbon nanotubes, Al_2O_3 NWs, and ZnO nanocrystals has been demonstrated.[47,48,198,199] This fast and easily controllable patterning approach has potential for diverse applications in microelectronics, chemical/biomolecular systems, photonics, and energy-conversion systems.

Haga and co-workers demonstrated the simultaneous formation and spatial patterning of ZnO nanocrystals on ITO substrates in aqueous $[Zn(NH_3)_4]^{2+}$ solution based on the laser-induced generation of microbubbles (**Figure 24**a–d).[47] For this purpose, a CW laser (Nd:YAG, 1064 nm) was focused on the ITO surface through the objective lens of an optical microscope. The photothermal formation of microbubbles and a subsequent concentration/accumulation of metal ions in the vicinity of the laser-beam focus was proposed to lead to self-assembly of the material from the solution at the edges of the bubble due to Gibbs–Marangoni convection. Furthermore, solvent evaporation from the bubble–substrate–solution three-phase contact line accelerates the nucleation and growth of the MO at the interface. Finally, manipulation of the location of the bubble formation by laser scanning results in a spatial patterning of the material on the substrate (Figure 24e).[47] To induce the above-discussed phenomenon, it is necessary to have a precursor solution with high absorbance in the chosen laser-wavelength region and a substrate with low thermal conductivity for inducing local heating on its surface upon laser irradiation.

Lv et al.[48] developed a laser-assisted solution-spreading method for fabrication and self-assembly of Al_2O_3 NWs into well-organized 3D micropatterns. A pulsed laser (355 nm) was used to etch the template in a controllable manner. Direct spreading of the NaOH solution onto the AAO template resulted in random patterns of the NWs due to uncontrolled capillary force during the solution evaporation (Figure 24f,g). However, solution spreading after laser etching of the template generated regular assembly of NWs (Figure 24h,i). All the NWs evidently lodged toward the laser-etched points and formed a microscale volcano-like structure (Figure 24j). The laser-etched AAO template regions appeared to undergo a considerably slower chemical etching process by the NaOH solution compared to the nonetched template parts (Figure 24k,l). Furthermore, the laser-etched area was found to act as a fixation point during the NW assembly process, and suitable modification of the distance between the laser scans could allow well-controlled NW patterns (Figure 24m,n). By designing the laser etching pattern, various micropatterned Al_2O_3 NWs were obtained in a straightforward way. The above findings will motivate other researchers to devise strategies for creating tunable 3D architectures from 1D nanostructures in a controllable manner.

5.5. Laser Direct Writing/Structuring of Metal Oxides

Devices based on microelectromechanical systems (MEMS) are used in various applications, including electronics, information technology, biomedicine, and energy-harvesting systems. As an alternative to the conventional photobeam/e-beam-/ion-beam lithography techniques, laser direct structuring/writing (LDS/LDW) has attracted considerable interest as a simple, maskless, low-cost method for fabricating 2D and 3D structures of different metals and their oxides.[66,67,200–202] Recently, LPKF Laser & Electronics AG has demonstrated a precise and effective LDS method to produce microstructured layouts. The LDS technique was employed to create ultrafine insulation spaces in transparent, conductive ITO films deposited on glass or polymers. The insulation channels, formed by laser scribing of fine structures in the ITO layer, can be designed with any required dimensions and geometry. The LDS method is very flexible, with the possibility of optimizing the layout continuously, and the modified layout data can immediately be incorporated into new products.[65,203]

Mizoshiri et al.[67] reported the direct fabrication of a Cu/Cu_2O composite temperature microsensor by laser reduction patterning of CuO NPs. A femtosecond fiber laser (780 nm) was employed to selectively reduce the CuO NP solution spin-coated on a glass

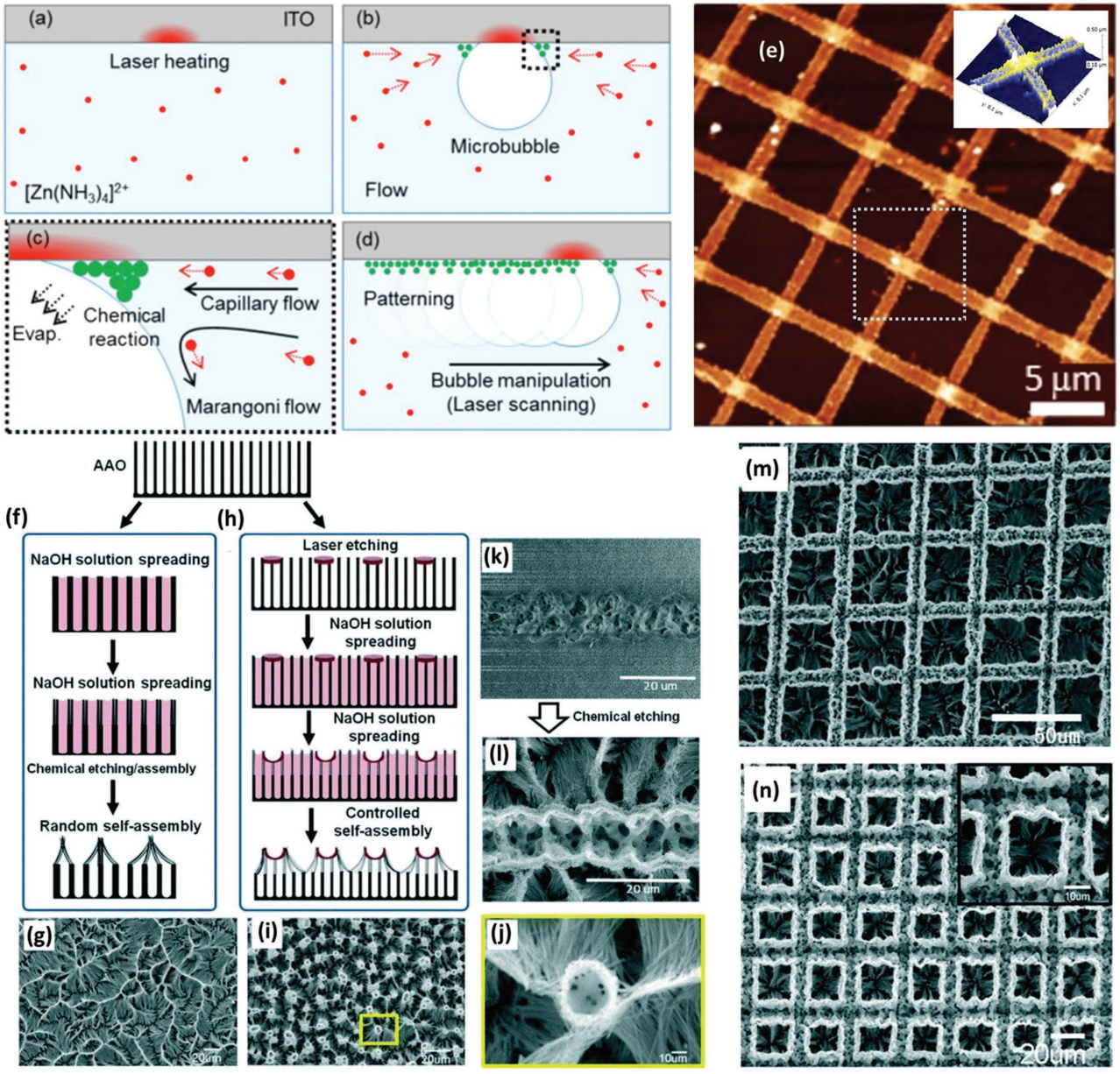

Figure 24. a–d) Schematic illustration of the spatial patterning of ZnO based on the laser-induced formation of microbubbles. e) AFM image of the ZnO nanocrystals pattern formed on the ITO surface (the inset of (e) shows a 3D height image for the dotted pale-blue square in the pattern). a–e) Reproduced with permission.[47] Copyright 2017, American Chemical Society. f–i) Schematic illustration of the direct and laser-assisted solution spreading and the resulting irregular and ordered assembling of Al_2O_3 NWs, respectively. j) High-magnification image of a single laser pointed NW assembly. k,l) SEM images of the AAO substrate after laser treatment and then after solution spreading, respectively. m,n) Micropatterns of Al_2O_3 NWs obtained by altered distances between adjacent laser scan lines (≈30 µm (m) and 19 µm (n)). f–n) Reproduced with permission.[48] Copyright 2014, The Royal Society of Chemistry.

substrate (**Figure 25**a). A strong correlation between Cu/Cu_2O formation and the laser parameters (laser energy (0.17–0.54 nJ), scan speed (1–20 mm s^{-1}), and raster scan pitch (5–15 µm)) was observed. Cu-rich electrodes were formed at a scan speed of 15 mm s^{-1}, a raster scan pitch of 5 µm, and a pulse energy of 0.45 nJ. Semiconductor-like Cu_2O was generated by reoxidation of Cu in the micropatterns, after irradiation at a scan speed of 1 mm s^{-1}, a raster scan pitch of 5 µm, and a pulse energy of 0.54 nJ. The fabricated temperature microsensor is shown in Figure 25b,c. The above results suggest that it is possible to fabricate metal/MO microdevices selectively by simply controlling the laser irradiation conditions.

Wang et al.[66] fabricated TiO_2-based microdevices, such as a Fresnel lens, a gear structure and suspended beams, simply by LDW and etching treatment. Initially, Ti films (50 nm thick) were deposited on glass substrates by an electron-beam-evaporation technique, and then gratings were formed by raster-scanning the films with a Nd:YAG laser (532 nm,

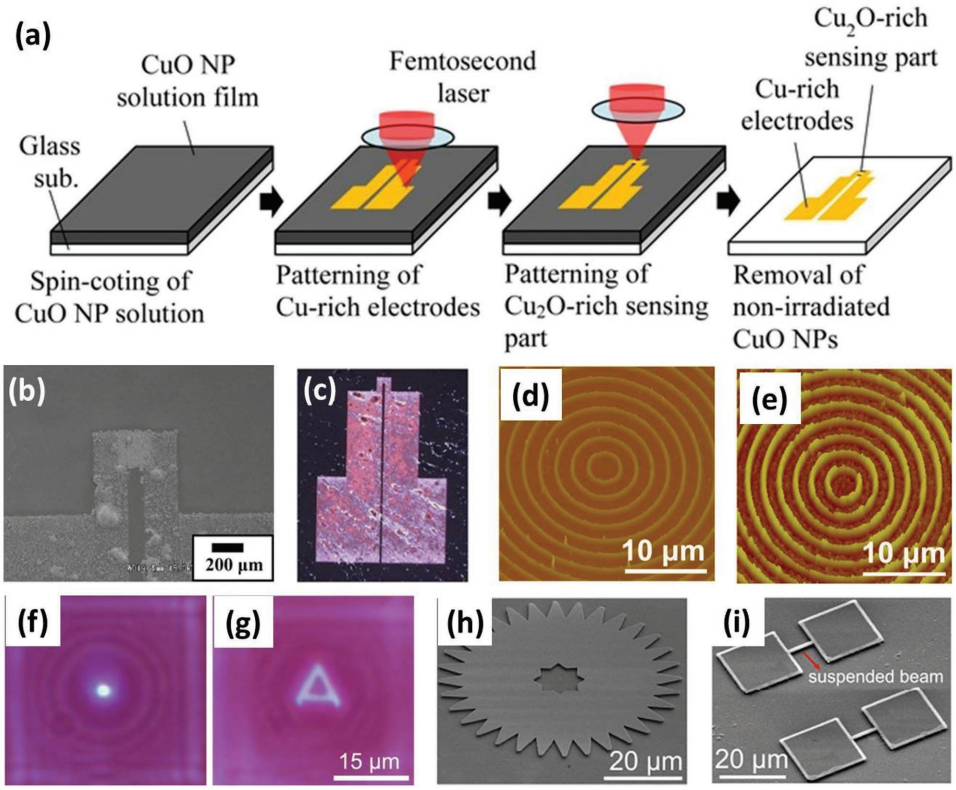

Figure 25. a–c) Laser direct writing (LDW) process, SEM image, and optical microscopy image of the Cu/Cu_2O composite temperature microsensor, respectively. a–c) Reproduced with permission.[67] Copyright 2016, The Japan Society of Applied Physics. d,e) AFM images of the concentric ring pattern of TiO_2 formed by LDW and subsequent dry etching, respectively. f,g) Optical microscopy images of the focusing image of a Fresnel lens made of the TiO_2 pattern and a letter "A" imaged through the lens. h,i) SEM images of MEMS structures of TiO_2 fabricated by LDW and subsequent wet etching. d–i) Reproduced with permission.[66] Copyright 2011, Optical Society of America.

50 μm s^{-1}, 250 Hz). Both the width and the height of the grating lines increased proportionally with the laser power (1–15 mW). The transparency of the Ti film changed above the laser power of 3 mW due to the phase transformation of Ti into the rutile TiO_2 structure under laser irradiation. After LDW, both dry and wet etching of the films was carried out to construct TiO_2-based microdevices. Figure 25d,e shows the concentric rings obtained by dry etching (CF_4/O_2) of the LDW films. The Fresnel lens made using the LDW-fabricated TiO_2 films on a glass substrate was also demonstrated to function as an optical element with good performance (Figure 25f,g). In addition, MEMS structures of gear and suspended beams of TiO_2 (Figure 25h,i) were also fabricated by LDW and subsequent wet etching (HF). Furthermore, the dimensions of the TiO_2 structures can be adjusted, in the above method, to meet different application requirements.

6. Conclusions and Outlook

The rising interest in laser processing over the past two decades has confirmed the relevance of this technique for scientific and technological developments. The availability of a diverse range of lasers with extended parameter control allows them to be employed in the processing of a wide variety of materials covering metals and alloys, ceramics, polymers, and composites. Lasers can induce spatially resolved thermal effects enabling excellent control over material modifications. Recent developments in laser technology combined with enhanced fundamental understanding of laser–material interactions and design of innovative fabrication approaches have facilitated the rapid processing of materials with improved functionality.

Laser systems operating in CW or pulsed modes over wavelengths in the range of UV to IR have been employed to induce controlled heating effects, chemical reactions, and other complex phenomena in MOs. Laser irradiation has demonstrated significant improvements in the physical properties and functional performance of these oxide structures. Despite the exciting prospects of laser irradiation in materials fabrication at low temperatures and on short time scales, the use of highly energetic laser sources requires a careful control over different processing parameters to avoid damage to the constituent materials.

Film thickness and dimensions of the nanostructures were found to be important processing variables in laser irradiation of functional materials. The inhomogeneous temperature distribution inside thick films was found to result in partial crystallization and the development of high thermal stress, leading to the formation of cracks. However, very thin precursor films, which were transparent to the laser radiation, failed to sustain the temperature required for initiating crystallization. Similarly, limited

heat dissipation through long NWs may constrain the laser energy near the tip, leading to excessive melting and breakage. Similar issues were found to occur during the laser-assisted growth of NWs, where the already-grown portions of the NWs were found to behave as thermal fins, limiting the heat dissipation and thereby further growth. Appropriate photothermal conditions should be considered in the design of the laser treatment.

Few studies have attempted to evaluate the direct correlation between the process parameters and the resulting physical behavior of the materials. There are a limited number of studies on in situ characterization of laser-processed materials and on comparative analysis of experimental and theoretical results. These studies are needed to provide insight into real-time laser-induced enhancements in the physical properties and the functional performance of materials. The use of lasers for mass production and large-area roll-to-roll fabrication of functional materials and nanostructures is still in the early stages of development. For long-term progress of laser-based manufacturing, interdisciplinary theoretical and experimental approaches are necessary to provide understanding of the dissimilar physical concepts in laser-induced functional changes at different length and time scales. The current technological advancement in laser processing is highly encouraging for future commercial development of manufacturing processes.

Acknowledgements

H.P., J.H.P., and D.M. contributed equally to this work. This research work was supported by the National Research Foundation of Korea (Grant No. NRF-2016R1A2B4011663), the Korea Institute of Materials Science (KIMS) internal R&D program (Grant No. PNK5061), and the U.S. Office of Naval Research Global (Grant No. N62909-16-1-2135). K.J.L. is thankful to the Ministry of Science, ICT and Future Planning, Korea for funding Nano Material Technology Development Program (Grant No. NRF-2016M3A7B4905621) through the National Research Foundation of Korea (NRF). D.M. and S.P. acknowledge financial support from the Office of Basic Energy Science, U.S. Department of Energy (Grant No. DE-FG02-06ER46290). J.R. and S.P. are thankful to Office of Naval of Research (I. Perez) for funding the US–Korea research collaboration (Grant No. N000141613043). V.A. would like to acknowledge the support from the Department of Science and Technology (DST), Government of India under the INSPIRE Faculty scheme. D.M. acknowledges the partial support from NSF-CREST (Grant No. HRD 1547771).

Conflict of Interest

The authors declare no conflict of interest.

Keywords

functional materials, laser radiation, metal oxide, physical behavior, thermal treatment

Received: September 8, 2017
Revised: October 20, 2017
Published online: February 7, 2018

[1] S. B. Ogale, T. V Venkatesan, M. Blamire, *Functional Metal Oxides: New Science and Novel Applications*, Wiley-VCH, Weinheim, Germany **2013**.
[2] A. K. Srivastava, *Oxide Nanostructures: Growth, Microstructures, and Properties*, Pan Stanford Publishing, CRC Press, Taylor & Francis Group, Boca Raton, FL, USA **2014**.
[3] G. Pacchioni, S. Valeri, *Oxide Ultrathin Films: Science and Technology*, Wiley-VCH, Weinheim, Germany **2012**.
[4] *Thin Film Metal-Oxides: Fundamentals and Applications in Electronics and Energy* (Ed: S. Ramanathan), Springer **2010**.
[5] T. Nakajima, K. Shinoda, T. Tsuchiya, *Chem. Soc. Rev.* **2014**, *43*, 2027.
[6] D. Hwang, S.-G. Ryu, N. Misra, H. Jeon, C. P. Grigoropoulos, *Appl. Phys. A* **2009**, *96*, 289.
[7] D. J. Joe, S. Kim, J. H. Park, D. Y. Park, H. E. Lee, T. H. Im, I. Choi, R. S. Ruoff, K. J. Lee, *Adv. Mater.* **2017**, *29*, 1606586.
[8] J.-G. Cheng, J. Wang, T. Dechakupt, S. Trolier-McKinstry, *Appl. Phys. Lett.* **2005**, *87*, 232905.
[9] H. Wang, A. Pyatenko, K. Kawaguchi, X. Li, Z. Swiatkowska-Warkocka, N. Koshizaki, *Angew. Chem., Int. Ed.* **2010**, *49*, 6361.
[10] A. Queraltó, A. Pérez del Pino, M. de la Mata, J. Arbiol, M. Tristany, X. Obradors, T. Puig, *Chem. Mater.* **2016**, *28*, 6136.
[11] S. Hong, H. Lee, J. Yeo, S. H. Ko, *Nano Today* **2016**, *11*, 547.
[12] G. Mincuzzi, A. L. Palma, A. Di Carlo, T. M. Brown, *ChemElectroChem* **2016**, *3*, 9.
[13] Y.-L. Zhang, D.-Q. Chen, H. Xia, H.-B. Sun, *Nano Today* **2010**, *5*, 435.
[14] Annual Laser Market Review & Forecast: Where have all the lasers gone?, http://www.laserfocusworld.com/articles/print/volume-53/issue-01/features/annual-laser-market-review-forecast-where-have-all-the-lasers-gone.html (accessed: July 2017).
[15] The Digital Display Revolution: Built on Excimer Laser Annealing, http://www.coherent.co.jp/document/whitepaper/fpd/vyper_laser_annealing.pdf (accessed: July 2017).
[16] S. S. N. Bharadwaja, A. Rajashekhar, S. W. Ko, W. Qu, M. Motyka, N. Podraza, T. Clark, C. A. Randall, S. Trolier-McKinstry, *J. Appl. Phys.* **2016**, *119*, 24106.
[17] M.-G. Kang, K.-H. Cho, Y. Ho Do, Y.-J. Lee, S. Nahm, S.-J. Yoon, C.-Y. Kang, *Appl. Phys. Lett.* **2012**, *101*, 242910.
[18] W. X. Xianyu, H. S. Cho, J. Y. Kwon, H. X. Yin, T. Noguchi, *MRS Online Proc. Libr.* **2004**, *830*, D3.6.
[19] A. Queraltó, A. Pérez del Pino, M. de la Mata, J. Arbiol, M. Tristany, A. Gómez, X. Obradors, T. Puig, *Appl. Phys. Lett.* **2015**, *106*, 262903.
[20] H. Palneedi, D. Maurya, G.-Y. Kim, V. Annapureddy, M.-S. Noh, C.-Y. Kang, J.-W. Kim, J.-J. Choi, S.-Y. Choi, S.-Y. Chung, S.-J. L. Kang, S. Priya, J. Ryu, *Adv. Mater.* **2017**, *29*, 1605688.
[21] R. Molaei, M. R. Bayati, H. M. Alipour, S. Nori, J. Narayan, *J. Appl. Phys.* **2013**, *113*, 233708.
[22] Y. Hou, A. H. Jayatissa, *Thin Solid Films* **2014**, *562*, 585.
[23] D. Lee, H. Pan, S. H. Ko, H. K. Park, E. Kim, C. P. Grigoropoulos, *Appl. Phys. A* **2012**, *107*, 161.
[24] C. Lee, P. Srisungsitthisunti, S. Park, S. Kim, X. Xu, K. Roy, D. B. Janes, C. Zhou, S. Ju, M. Qi, *ACS Nano* **2011**, *5*, 1095.
[25] W. J. Dong, J. Ham, G. H. Jung, J. H. Son, J.-L. Lee, *J. Mater. Chem. A* **2016**, *4*, 4755.
[26] T. Nakajima, T. Tsuchiya, *J. Mater. Chem. C* **2015**, *3*, 3809.
[27] T. Nakajima, T. Tsuchiya, T. Kumagai, *J. Solid State Chem.* **2009**, *182*, 2560.
[28] N. Terakado, R. Takahashi, Y. Takahashi, T. Fujiwara, *Thin Solid Films* **2016**, *603*, 303.
[29] R. Molaei, R. Bayati, S. Nori, D. Kumar, J. T. Prater, J. Narayan, *Appl. Phys. Lett.* **2013**, *103*, 252109.
[30] S. S. Rao, Y. F. Lee, J. T. Prater, A. I. Smirnov, J. Narayan, *Appl. Phys. Lett.* **2014**, *105*, 42403.

[31] Y. Q. Zhang, X. Z. Ruan, B. Liu, Z. Y. Xu, Q. Y. Xu, J. D. Shen, Q. Li, J. Wang, B. You, H. Q. Tu, Y. Gao, W. Zhang, Y. B. Xu, J. Du, *Appl. Surf. Sci.* **2016**, *367*, 418.
[32] X. Wang, Y. Ding, D. Yuan, J.-I. Hong, Y. Liu, C. P. Wong, C. Hu, Z. L. Wang, *Nano Res.* **2012**, *5*, 412.
[33] R. Molaei, R. Bayati, J. Narayan, *Cryst. Growth Des.* **2013**, *13*, 5459.
[34] X. Pan, Y. Shuai, C. Wu, W. Luo, X. Sun, Y. Yuan, S. Zhou, X. Ou, W. Zhang, *Appl. Surf. Sci.* **2016**, *389*, 1104.
[35] J. P. B. Silva, K. Kamakshi, K. C. Sekhar, J. A. Moreira, A. Almeida, M. Pereira, M. J. M. Gomes, *Phys. Status Solidi* **2016**, *213*, 1082.
[36] N. A. Charipar, H. Kim, E. Breckenfeld, K. M. Charipar, S. A. Mathews, A. Piqué, *Appl. Phys. A* **2016**, *122*, 512.
[37] S. Cha, S. Lee, J. E. Jang, A. Jang, J. P. Hong, J. Lee, J. I. Sohn, D. J. Kang, J. M. Kim, *Appl. Phys. Lett.* **2013**, *103*, 53114.
[38] D. Shiojiri, R. Yamauchi, D. Fukuda, N. Tsuchimine, S. Kaneko, A. Matsuda, M. Yoshimoto, *J. Cryst. Growth* **2015**, *424*, 38.
[39] S. O. El hamali, W. M. Cranton, N. Kalfagiannis, X. Hou, R. Ranson, D. C. Koutsogeorgis, *Opt. Lasers Eng.* **2016**, *80*, 45.
[40] W.-T. Hsiao, S.-F. Tseng, C.-K. Chung, D. Chiang, K.-C. Huang, K.-M. Lin, L.-Y. Li, M.-F. Chen, *Opt. Laser Technol.* **2015**, *68*, 41.
[41] J. Yeo, S. Hong, M. Wanit, H. W. Kang, D. Lee, C. P. Grigoropoulos, H. J. Sung, S. H. Ko, *Adv. Funct. Mater.* **2013**, *23*, 3316.
[42] S. Hong, J. Yeo, W. Manorotkul, H. W. Kang, J. Lee, S. Han, Y. Rho, Y. D. Suh, H. J. Sung, S. H. Ko, *Nanoscale* **2013**, *5*, 3698.
[43] J. Bin In, H.-J. Kwon, D. Lee, S. H. Ko, C. P. Grigoropoulos, *Small* **2014**, *10*, 741.
[44] J. Yeo, S. Hong, G. Kim, H. Lee, Y. D. Suh, I. Park, C. P. Grigoropoulos, S. H. Ko, *ACS Nano* **2015**, *9*, 6059.
[45] J. Yeo, S. Hong, W. Manorotkul, Y. D. Suh, J. Lee, J. Kwon, S. H. Ko, *J. Phys. Chem. C* **2014**, *118*, 15448.
[46] Y. Xie, S. Yang, Z. Mao, P. Li, C. Zhao, Z. Cohick, P.-H. Huang, T. J. Huang, *ACS Nano* **2014**, *8*, 12175.
[47] S. Fujii, R. Fukano, Y. Hayami, H. Ozawa, E. Muneyuki, N. Kitamura, M. Haga, *ACS Appl. Mater. Interfaces* **2017**, *9*, 8413.
[48] M. Lv, Q. Wang, Q. Meng, T. Zhao, H. Liu, L. Jiang, *CrystEngComm* **2015**, *17*, 540.
[49] D. Lin, P. Kumar, S. Jin, S. Liu, Q. Nian, G. J. Cheng, *Appl. Surf. Sci.* **2015**, *351*, 148.
[50] G. Wang, K. Li, F. J. Purcell, D. Zhao, W. Zhang, Z. He, S. Tan, Z. Tang, H. Wang, E. Reichmanis, *ACS Appl. Mater. Interfaces* **2016**, *8*, 24974.
[51] J. Huang, D. Ma, F. Chen, D. Chen, M. Bai, K. Xu, Y. Zhao, *ACS Appl. Mater. Interfaces* **2017**, *9*, 7436.
[52] X. Z. Lin, P. Liu, J. M. Yu, G. W. Yang, *J. Phys. Chem. C* **2009**, *113*, 17543.
[53] D. Zhang, Z. Ma, M. Spasova, A. E. Yelsukova, S. Lu, M. Farle, U. Wiedwald, B. Gökce, *Part. Part. Syst. Charact.* **2017**, *34*, 1600225.
[54] T. Schmitz, U. Wiedwald, C. Dubs, B. Gökce, *ChemPhysChem* **2017**, *18*, 1125.
[55] H. Zhang, C. Liang, J. Liu, Z. Tian, G. Wang, W. Cai, *Langmuir* **2012**, *28*, 3938.
[56] D. Amans, C. Malaterre, M. Diouf, C. Mancini, F. Chaput, G. Ledoux, G. Breton, Y. Guillin, C. Dujardin, K. Masenelli-Varlot, P. Perriat, *J. Phys. Chem. C* **2011**, *115*, 5131.
[57] V. Amendola, P. Riello, M. Meneghetti, *J. Phys. Chem. C* **2011**, *115*, 5140.
[58] D. Zhang, B. Gökce, S. Barcikowski, *Chem. Rev.* **2017**, *117*, 3990.
[59] D. Zhang, B. Gökce, *Appl. Surf. Sci.* **2017**, *392*, 991.
[60] E. Maurer, S. Barcikowski, B. Gökce, *Chem. Eng. Technol.* **2017**, *40*, 1535.
[61] V. Amendola, M. Meneghetti, *Phys. Chem. Chem. Phys.* **2013**, *15*, 3027.
[62] R. Ye, Z. Peng, T. Wang, Y. Xu, J. Zhang, Y. Li, L. G. Nilewski, J. Lin, J. M. Tour, *ACS Nano* **2015**, *9*, 9244.
[63] D. Morselli, A. Scarpellini, A. Athanassiou, D. Fragouli, *RSC Adv.* **2016**, *6*, 11412.
[64] Y. Rho, K.-T. Kang, D. Lee, *Nanoscale* **2016**, *8*, 8976.
[65] *Laser Structuring of ITO Layers*, http://www.lpkf.com/applications/laser-micromachining/ito-layer-structuring.htm (accessed: July 2017).
[66] Y. Wang, J. Miao, Y. Tian, C. Guo, J. Zhang, T. Ren, Q. Liu, *Opt. Express* **2011**, *19*, 17390.
[67] M. Mizoshiri, Y. Ito, S. Arakane, J. Sakurai, S. Hata, *Jpn. J. Appl. Phys.* **2016**, *55*, 06GP05.
[68] A. I. Bogdan, J. Kaufman, *Basics in Dermatological Laser Applications* (Eds: A. I. Bogdan, D. J. Goldberg), Karger, Basel, Switzerland **2011**, pp. 7–23.
[69] J. D. Majumdar, I. Manna, *Laser-Assisted Fabrication Materials* (Eds: J. D. Majumdar, I. Manna), Springer-Verlag, Heidelberg **2013**, pp. 1–67.
[70] J. D. Majumdar, I. Manna, *Sadhana* **2003**, *28*, 495.
[71] S. Siano, *Handbook on the Use of Lasers in Conservation and Conservation Science* (Eds: M. Schreiner, M. Strlic, R. Salimbeni), COST Office, Brussels, Belgium **2008**, pp. 1–26.
[72] M. S. Brown, C. B. Arnold, *Laser Precision Microfabrication* (Eds: K. Sugioka, M. Meunier, A. Piqué), Springer, Heidelberg, Germany **2010**, pp. 91–120.
[73] D. Bäuerle, *Laser Processing Chemistry*, Springer, Heidelberg, Germany **2011**, pp. 13–38.
[74] R. A. Ganeev, *Laser–Surface Interactions*, Springer Netherlands, Dordrecht, The Netherlands **2014**, pp. 1–21.
[75] A. G. Cullis, *Rep. Prog. Phys.* **1985**, *48*, 1155.
[76] E. Carpene, D. Hoche, P. Schaaf, *Laser Processing of Materials* (Ed: P. Schaaf), Springer-Verlag, Heidelberg, Germany **2010**, pp. 21–48.
[77] S. K. Sundaram, E. Mazur, *Nat. Mater.* **2002**, *1*, 217.
[78] D. Bäuerle, *Laser Processing Chemistry*, Springer-Verlag, Heidelberg, Germany **2011**, pp. 3–12.
[79] N. B. Dahotre, S. P. Harimkar, *Laser Fabrication and Machining of Materials*, Springer US, New York **2008**.
[80] G. Padmanabham, B. Shanmugarajan, *Laser-Assisted Fabrication Materials* (Eds: J. D. Majumdar, I. Manna), Springer-Verlag, Heidelberg, Germany **2013**, pp. 159–220.
[81] H. Kim, C. M. Gilmore, A. Piqué, J. S. Horwitz, H. Mattoussi, H. Murata, Z. H. Kafafi, D. B. Chrisey, *J. Appl. Phys.* **1999**, *86*, 6451.
[82] W. Zhang, Y. L. Yao, in *Manufacturing Engineering Handbook*, 2nd ed. (Ed: P. Hwaiyu Geng, CMfgE), McGraw Hill Professional, Access Engineering, New York **2016**, pp. 1–32.
[83] H. Palneedi, D. Maurya, G.-Y. Kim, S. Priya, S.-J. L. Kang, K.-H. Kim, S.-Y. Choi, J. Ryu, *Appl. Phys. Lett.* **2015**, *107*, 12904.
[84] H. Palneedi, I. Choi, G.-Y. Kim, V. Annapureddy, D. Maurya, S. Priya, J.-W. Kim, K. J. Lee, S.-Y. Choi, S.-Y. Chung, S.-J. L. Kang, J. Ryu, *J. Am. Ceram. Soc.* **2016**, *99*, 2680.
[85] I. Choi, H. Y. Jeong, D. Y. Jung, M. Byun, C.-G. Choi, B. H. Hong, S.-Y. Choi, K. J. Lee, *ACS Nano* **2014**, *8*, 7671.
[86] J. M. Poate, J. W. Mayer, *Laser Annealing of Semiconductors*, Academic Press, New York **1982**.
[87] B. Kang, S. Han, J. Kim, S. Ko, M. Yang, *J. Phys. Chem. C* **2011**, *115*, 23664.
[88] O. Suttmann, A. Moalem, R. Kling, A. Ostendorf, in *Laser Precision Microfabrication* (Eds: K. Sugioka, M. Meunier, A. Piqué), Springer, Heidelberg **2010**, pp. 311–335.
[89] S.-F. Tseng, W.-T. Hsiao, K.-C. Huang, D. Chiang, *Appl. Surf. Sci.* **2011**, *257*, 8813.
[90] M.-F. Chen, K. Lin, Y.-S. Ho, *Opt. Lasers Eng.* **2012**, *50*, 491.
[91] B. Li, L. Huang, M. Zhou, N. Ren, B. Wu, *Ceram. Int.* **2014**, *40*, 1627.
[92] L. Huang, B. Li, N. Ren, *Ceram. Int.* **2016**, *42*, 7246.

[93] A. Chernatynskiy, D. R. Clarke, S. R. Phillpot, in *Handbook of Nanoscience, Engineering, and Technology* (Eds: W. A. Goddard III, D. W. Brenner, S. E. Lyshevski, G. J. Iafrate), CRC Press, Boca Rotan **2012**, pp. 545–572.
[94] W. Kim, R. Wang, A. Majumdar, *Nano Today* **2007**, *2*, 40.
[95] T. Nakajima, T. Tsuchiya, *J. Mater. Chem. C* **2015**, *3*, 3809.
[96] P. Campbell, *J. Opt. Soc. Am. B* **1993**, *10*, 2410.
[97] D. Li, A. J. H. McGaughey, *Nanoscale Microscale Thermophys. Eng.* **2015**, *19*, 166.
[98] O. Kluth, B. Rech, L. Houben, S. Wieder, G. Schöpe, C. Beneking, H. Wagner, A. Löffl, H. W. Schock, *Thin Solid Films* **1999**, *351*, 247.
[99] A. Pereira, A. Cros, P. Delaporte, S. Georgiou, A. Manousaki, W. Marine, M. Sentis, *Appl. Phys. A* **2004**, *79*, 1433.
[100] N. Ohtsu, K. Kodama, K. Kitagawa, K. Wagatsuma, *Appl. Surf. Sci.* **2010**, *256*, 4522.
[101] V. Le Borgne, H. Bazi, T. Hayashi, Y. A. Kim, M. Endo, M. A. El Khakani, *Carbon N. Y.* **2014**, *77*, 857.
[102] D. Zhang, B. Gökce, S. Sommer, R. Streubel, S. Barcikowski, *Appl. Surf. Sci.* **2016**, *367*, 222.
[103] B. Li, L. Huang, N. Ren, X. Kong, Y. Cai, J. Zhang, *Appl. Surf. Sci.* **2015**, *351*, 113.
[104] L. Huang, N. Ren, B. Li, M. Zhou, *Mater. Lett.* **2015**, *140*, 75.
[105] S. Prucnal, W. Skorupa, *Subsecond Annealing of Advanced Materials* (Eds: W. Skorupa, H. Schmidt), Springer International Publishing, Cham, Switzerland **2014**, pp. 189–210.
[106] H. M. Jin, S. H. Lee, J. Y. Kim, S.-W. Son, B. H. Kim, H. K. Lee, J. H. Mun, S. K. Cha, J. S. Kim, P. F. Nealey, K. J. Lee, S. O. Kim, *ACS Nano* **2016**, *10*, 3435.
[107] B. Li, H. Li, L. Huang, H. Cao, W. Zu, N. Ren, H. Ding, X. Kong, J. Zhang, *Ceram. Int.* **2017**, *43*, 7329.
[108] C. K. Jeong, S. B. Cho, J. H. Han, D. Y. Park, S. Yang, K.-I. Park, J. Ryu, H. Sohn, Y.-C. Chung, K. J. Lee, *Nano Res.* **2017**, *10*, 437.
[109] H. E. Lee, S. Kim, J. Ko, H.-I. Yeom, C.-W. Byun, S. H. Lee, D. J. Joe, T.-H. Im, S.-H. K. Park, K. J. Lee, *Adv. Funct. Mater.* **2016**, *26*, 6170.
[110] S. Kim, J. H. Son, S. H. Lee, B. K. You, K.-I. Park, H. K. Lee, M. Byun, K. J. Lee, *Adv. Mater.* **2014**, *26*, 7480.
[111] J. Heller, J. W. Bartha, C. C. Poon, A. C. Tam, *Appl. Phys. Lett.* **1999**, *75*, 43.
[112] E. D. Tsagarakis, C. Lew, M. O. Thompson, E. P. Giannelis, *Appl. Phys. Lett.* **2006**, *89*, 202910.
[113] S. Halder, U. Boettger, T. Schneller, R. Waser, O. Baldus, P. Jacobs, M. Wehner, *Mater. Sci. Eng., B* **2006**, *133*, 235.
[114] S. S. N. Bharadwaja, T. Dechakupt, S. Trolier-McKinstry, H. Beratan, *J. Am. Ceram. Soc.* **2008**, *91*, 1580.
[115] S. Baba, J. Akedo, *Appl. Surf. Sci.* **2009**, *255*, 9791.
[116] S. S. N. Bharadwaja, F. Griggio, J. Kulik, S. Trolier-McKinstry, *Appl. Phys. Lett.* **2011**, *99*, 42903.
[117] M. G. Kang, K. H. Cho, S. M. Oh, Y. H. Do, C. Y. Kang, S. Kim, S. J. Yoon, *Curr. Appl. Phys.* **2011**, *11*, S66.
[118] A. Rajashekhar, A. Fox, S. S. N. Bharadwaja, S. Trolier-McKinstry, *Appl. Phys. Lett.* **2013**, *103*, 32908.
[119] A. Queraltó, A. Pérez del Pino, M. de la Mata, M. Tristany, X. Obradors, T. Puig, S. Trolier-McKinstry, *Ceram. Int.* **2016**, *42*, 4039.
[120] M.-C. Kim, J.-W. Choi, C.-Y. Kang, S.-J. Yoon, H.-J. Kim, K.-H. Yoon, *Trans. Electr. Electron. Mater.* **2002**, *3*, 14.
[121] I.-H. Im, K.-H. Chung, D.-H. Kim, *Trans. Electr. Electron. Mater.* **2014**, *15*, 253.
[122] M. Morales-Masis, S. De Wolf, R. Woods-Robinson, J. W. Ager, C. Ballif, *Adv. Electron. Mater.* **2017**, *3*, 1600529.
[123] W. Chung, M. O. Thompson, P. Wickboldt, D. Toet, P. G. Carey, *Thin Solid Films* **2004**, *460*, 291.
[124] H. Pan, D. Lee, S. H. Ko, C. P. Grigoropoulos, H. K. Park, T. Hoult, *Appl. Phys. A* **2011**, *104*, 29.
[125] T. Park, D. Kim, *Thin Solid Films* **2015**, *578*, 76.
[126] T. Tsuchiya, F. Yamaguchi, I. Morimoto, T. Nakajima, T. Kumagai, *Appl. Phys. A* **2010**, *99*, 745.
[127] P. Rai, S. M. Majhi, Y.-T. Yu, J.-H. Lee, *RSC Adv.* **2015**, *5*, 76229.
[128] C. Liu, Q. Kuang, Z. Xie, L. Zheng, *CrystEngComm* **2015**, *17*, 6308.
[129] H. Zhang, S. Wu, J. Liu, Y. Cai, C. Liang, *Phys. Chem. Chem. Phys.* **2016**, *18*, 22503.
[130] Y. Hou, A. H. Jayatissa, *Thin Solid Films* **2014**, *562*, 585.
[131] S.-W. Choi, J. Y. Park, S. S. Kim, *J. Mater. Res.* **2011**, *26*, 1662.
[132] A. Katoch, G.-J. Sun, S.-W. Choi, J.-H. Byun, S. S. Kim, *Sens. Actuators, B* **2013**, *185*, 411.
[133] M. R. Bayati, H. M. Alipour, S. Joshi, R. Molaei, R. J. Narayan, J. Narayan, S. T. Misture, *J. Phys. Chem. C* **2013**, *117*, 7138.
[134] T. Nakajima, T. Kitamura, T. Tsuchiya, *Appl. Catal., B* **2011**, *108*, 47.
[135] M. Liu, R. Inde, M. Nishikawa, X. Qiu, D. Atarashi, E. Sakai, Y. Nosaka, K. Hashimoto, M. Miyauchi, *ACS Nano* **2014**, *8*, 7229.
[136] L. Petti, N. Münzenrieder, C. Vogt, H. Faber, L. Büthe, G. Cantarella, F. Bottacchi, T. D. Anthopoulos, G. Tröster, *Appl. Phys. Rev.* **2016**, *3*, 21303.
[137] D. Chen, Z. Liu, B. Liang, X. Wang, G. Shen, *Nanoscale* **2012**, *4*, 3001.
[138] W. Lu, P. Xie, C. M. Lieber, *IEEE Trans. Electron Devices* **2008**, *55*, 2859.
[139] H. Yu, H. Lee, J. Lee, H. Shin, M. Lee, *Microelectron. Eng.* **2011**, *88*, 6.
[140] C. H. Wu, H. Y. Huang, S. J. Wang, K. M. Chang, *IEEE Electron Device Lett.* **2014**, *35*, 1031.
[141] J. Maeng, S. Heo, G. Jo, M. Choe, S. Kim, H. Hwang, T. Lee, *Nanotechnology* **2009**, *20*, 095203.
[142] S. Kim, S. Kim, P. Srisungsitthisunti, C. Lee, M. Xu, P. D. Ye, M. Qi, X. Xu, C. Zhou, S. Ju, D. B. Janes, *J. Phys. Chem. C* **2011**, *115*, 17147.
[143] S. K. Garlapati, J. S. Gebauer, S. Dehm, M. Bruns, M. Winterer, H. Hahn, S. Dasgupta, *Adv. Electron. Mater.* **2017**, *3*, 1600476.
[144] G. Mincuzzi, L. Vesce, A. Reale, A. Di Carlo, T. M. Brown, *Appl. Phys. Lett.* **2009**, *95*, 103312.
[145] G. Mincuzzi, M. Schulz-Ruhtenberg, L. Vesce, A. Reale, A. Di Carlo, A. Gillner, T. M. Brown, *Prog. Photovoltaics Res. Appl.* **2014**, *22*, 308.
[146] B. T. Spann, S. V. Bhat, Q. Nian, K. M. Rickey, G. J. Cheng, X. Ruan, X. Xu, *Phys. Chem. Chem. Phys.* **2014**, *16*, 10669.
[147] J. Meyer, R. Khalandovsky, P. Görrn, A. Kahn, *Adv. Mater.* **2011**, *23*, 70.
[148] Y. Sun, C. J. Takacs, S. R. Cowan, J. H. Seo, X. Gong, A. Roy, A. J. Heeger, *Adv. Mater.* **2011**, *23*, 2226.
[149] C. Girotto, E. Voroshazi, D. Cheyns, P. Heremans, B. P. Rand, *ACS Appl. Mater. Interfaces* **2011**, *3*, 3244.
[150] S. Chambon, L. Derue, M. Lahaye, B. Pavageau, L. Hirsch, G. Wantz, *Materials* **2012**, *5*, 2521.
[151] M. Sygletou, C. Petridis, E. Kymakis, E. Stratakis, *Adv. Mater.* **2017**, *29*, 1700335.
[152] F. Di Giacomo, V. Zardetto, A. D'Epifanio, S. Pescetelli, F. Matteocci, S. Razza, A. Di Carlo, S. Licoccia, W. M. M. Kessels, M. Creatore, T. M. Brown, *Adv. Energy Mater.* **2015**, *5*, 1401808.
[153] S. Das, G. Gu, P. C. Joshi, B. Yang, T. Aytug, C. M. Rouleau, D. B. Geohegan, K. Xiao, *J. Mater. Chem. A* **2016**, *4*, 9685.
[154] B. Feleki, G. Bex, R. Andriessen, Y. Galagan, F. Di Giacomo, *Mater. Today Commun.* **2017**, *13*, 232.
[155] A. Fakharuddin, A. L. Palma, F. D. Giacomo, S. Casaluci, F. Matteocci, Q. Wali, M. Rauf, A. D. Carlo, T. M. Brown, R. Jose, *Nanotechnology* **2015**, *26*, 494002.
[156] A. Fakharuddin, F. D. Giacomo, A. L. Palma, F. Matteocci, I. Ahmed, S. Razza, A. D'Epifanio, S. Licoccia, J. Ismail, A. D. Carlo, T. M. Brown, R. Jose, *ACS Nano* **2015**, *9*, 8420.

[157] T. Meguro, Y. Abe, T. Yokoyama, S. Murosawa, K. K. J. Tatami, *Jpn. J. Appl. Phys.* **2001**, *40*, 5041.
[158] K. Park, D. Y. Bang, *J. Mater. Sci.: Mater. Electron.* **2003**, *14*, 81.
[159] L. He, Z. Y. Ling, Y. T. Huang, Y. S. Liu, *Mater. Lett.* **2011**, *65*, 1632.
[160] J. Ryu, K.-Y. Kim, J.-J. Choi, B.-D. Hahn, W.-H. Yoon, B.-K. Lee, D.-S. Park, C. Park, *J. Am. Ceram. Soc.* **2009**, *92*, 3084.
[161] J. Ryu, D.-S. Park, R. Schmidt, *J. Appl. Phys.* **2011**, *109*, 113722.
[162] S. Zhou, E. Čižmár, K. Potzger, M. Krause, G. Talut, M. Helm, J. Fassbender, S. A. Zvyagin, J. Wosnitza, H. Schmidt, *Phys. Rev. B* **2009**, *79*, 113201.
[163] T. Nakajima, T. Tsuchiya, T. Kumagai, *Jpn. J. Appl. Phys.* **2007**, *46*, L365.
[164] T. Nakajima, T. Tsuchiya, K. Daoudi, M. Ichihara, Y. Ueda, T. Kumagai, *Chem. Mater.* **2007**, *19*, 5355.
[165] P. Yan, K. du, M. Sui, *Acta Mater.* **2010**, *58*, 3867.
[166] M. Vila, C. Diaz-Guerra, J. Piqueras, *Appl. Phys. Lett.* **2012**, *101*, 071905.
[167] D. S. Murali, A. Subrahmanyam, *J. Phys. D.: Appl. Phys.* **2016**, *49*, 375102.
[168] Y. He, Y. Zhao, *J. Phys. Chem. C* **2008**, *112*, 61.
[169] K. Starbova, V. Mankov, N. Starbov, D. Popov, D. Nihtianova, K. Kolev, L. D. Laude, *Appl. Surf. Sci.* **2001**, *173*, 177.
[170] S. R. Singamaneni, S. Punugupati, J. T. Prater, F. Hunte, J. Narayan, *J. Appl. Phys.* **2014**, *116*, 94103.
[171] J. Dho, M. G. Blamire, *J. Appl. Phys.* **2009**, *106*, 73914.
[172] H. W. Chang, F. T. Yuan, C. W. Shih, W. L. Li, P. H. Chen, C. R. Wang, W. C. Chang, S. U. Jen, *J. Appl. Phys.* **2012**, *111*, 07B105.
[173] R. Molaei, M. R. Bayati, H. M. Alipour, N. A. Estrich, J. Narayan, *J. Phys.: Condens. Matter* **2014**, *26*, 015004.
[174] H. Li, Y. Lai, J. Huang, Y. Tang, L. Yang, Z. Chen, K.-Q. Zhang, X. Wang, L. P. Tan, *J. Mater. Chem. B* **2015**, *3*, 342.
[175] D. Ruzmetov, S. Ramanathan, *Thin Film Metal Oxides* (Ed: S. Ramanathan), Springer US, New York **2010**, pp. 51–94.
[176] M. Nishikawa, T. Nakajima, T. Manabe, T. Okutani, T. Tsuchiya, *Mater. Lett.* **2010**, *64*, 1921.
[177] T. Nakajima, T. Tsuchiya, M. Ichihara, H. Nagai, T. Kumagai, *Appl. Surf. Sci.* **2009**, *255*, 9775.
[178] T. Nakajima, T. Tsuchiya, M. Ichihara1, H. Nagai, T. Kumagai, *Appl. Phys. Express* **2009**, *2*, 23001.
[179] T. Nakajima, K. Shinoda, T. Tsuchiya, *Phys. Chem. Chem. Phys.* **2013**, *15*, 14384.
[180] T. Tsuchiya, A. Watanbe, Y. Imai, H. Niino, I. Yamaguchi, T. Manabe, T. Kumagai, S. Mizuta, *Jpn. J. Appl. Phys.* **1999**, *38*, L823.
[181] T. Nagase, T. Ooie, J. Sakakibara, *Thin Solid Films* **1999**, *357*, 151.
[182] H. Imai, A. Tominaga, H. Hirashima, M. Toki, N. Asakuma, *J. Appl. Phys.* **1998**, *85*, 203.
[183] T. Tsuchiya, A. Watanabe, Y. Imai, H. Niino, I. Yamaguchi, T. Manabe, T. Kumagai, S. Mizuta, *Jpn. J. Appl. Phys.* **2000**, *39*, L866.
[184] T. Tsuchiya, T. Nakajima, T. Kumagai, *Appl. Surf. Sci.* **2009**, *255*, 9804.
[185] T. Miyazaki, S. Sou, N. Sakamoto, N. Wakiya, H. Suzuki, *J. Ceram. Soc. Japan* **2009**, *117*, 950.
[186] W. M. Cranton, S. L. Wilson, R. Ranson, D. C. Koutsogeorgis, K. Chi, R. Hedgley, J. Scott, S. Lipiec, A. Spiller, S. Speakman, *Thin Solid Films* **2007**, *515*, 8534.
[187] T. Nakajima, T. Tsuchiya, T. Kumagai, *Cryst. Growth Des.* **2010**, *10*, 4861.
[188] H. Zeng, X.-W. Du, S. C. Singh, S. A. Kulinich, S. Yang, J. He, W. Cai, *Adv. Funct. Mater.* **2012**, *22*, 1333.
[189] M. Kim, S. Osone, T. Kim, H. Higashi, T. Seto, *KONA Powder Part. J.* **2017**, *34*, 88.
[190] J. Lam, J. Lombard, C. Dujardin, G. Ledoux, S. Merabia, D. Amans, *Appl. Phys. Lett.* **2016**, *108*, 74104.
[191] S. Reich, P. Schönfeld, A. Letzel, S. Kohsakowski, M. Olbinado, B. Gökce, S. Barcikowski, A. Plech, *ChemPhysChem* **2017**, *18*, 1084.
[192] A. Letzel, B. Gökce, P. Wagener, S. Ibrahimkutty, A. Menzel, A. Plech, S. Barcikowski, *J. Phys. Chem. C* **2017**, *121*, 5356.
[193] C.-Y. Shih, C. Wu, M. V Shugaev, L. V Zhigilei, *J. Colloid Interface Sci.* **2017**, *489*, 3.
[194] R. Streubel, G. Bendt, B. Gökce, *Nanotechnology* **2016**, *27*, 205602.
[195] R. Streubel, S. Barcikowski, B. Gökce, *Opt. Lett.* **2016**, *41*, 1486.
[196] S. Jendrzej, B. Gökce, M. Epple, S. Barcikowski, *ChemPhysChem* **2017**, *18*, 1012.
[197] M.-R. Kalus, N. Barsch, R. Streubel, E. Gokce, S. Barcikowski, B. Gokce, *Phys. Chem. Chem. Phys.* **2017**, *19*, 7112.
[198] B. Roy, M. Arya, P. Thomas, J. K. Jürgschat, K. V Rao, A. Banerjee, C. M. Reddy, S. Roy, *Langmuir* **2013**, *29*, 14733.
[199] S. Roy, *CrystEngComm* **2014**, *16*, 4667.
[200] M. Gebhardt, J. Hänel, F. Allenstein, C. Scholz, M. Clair, *Laser Tech. J.* **2013**, *10*, 25.
[201] S. Krause, P.-T. Miclea, F. Steudel, S. Schweizer, G. Seifert, *J. Renewable Sustainable Energy* **2014**, *6*, 11402.
[202] M. Beresna, M. Gecevičius, P. G. Kazansky, *Adv. Opt. Photonics* **2014**, *6*, 293.
[203] Application Report LPKF MicroLine UV Laser Systems, Laser Structuring of Conductive TCO/ITO Coatingss, http://www.lpkf.com/_mediafiles/219-laser-structuring-of-conductive-tco-ito-coatings.pdf (accessed: July 2017).

